

Targeting ferroptosis for neuroprotection
Novel diphenylamine compounds targeting
mitochondrial pathways of oxidative cell death

Dissertation

zur

Erlangung des Doktorgrades
der Naturwissenschaften

(Dr. rer. nat.)

dem

Fachbereich Pharmazie der
Philipps-Universität Marburg

vorgelegt von

Lukas Hinder

aus Lich

Marburg/Lahn **2021**

Erstgutachter: Prof. Dr. Carsten Culmsee

Zweitgutachter: Prof. Dr. Martin Schlitzer

Eingereicht am 24.09.2021

Tag der mündlichen Prüfung: 10.11.2021

Hochschulkenziffer: 1180

ERKLÄRUNG

Ich versichere, dass ich meine Dissertation

„Targeting ferroptosis for neuroprotection

Novel diphenylamine compounds targeting mitochondrial pathways of oxidative cell death “

selbständig ohne unerlaubte Hilfe angefertigt und mich dabei keiner anderen als der von mir ausdrücklich bezeichneten Quellen bedient habe. Alle vollständig oder sinngemäß übernommenen Zitate sind als solche gekennzeichnet.

Die Dissertation wurde in der jetzigen oder einer ähnlichen Form noch bei keiner anderen Hochschule eingereicht und hat noch keinen sonstigen Prüfungszwecken gedient.

Marburg, den

.....
(Lukas Hinder)

Teilergebnisse der vorliegenden Arbeit wurden bereits vorab publiziert:

(1) Characterization of novel diphenylamine compounds as ferroptosis inhibitors / 27.01.2021 zur Veröffentlichung eingereicht bei „Journal of Pharmacology and Experimental Therapeutics“/ 04.05.2021 zur Veröffentlichung angenommen bei „Journal of Pharmacology and Experimental Therapeutics“:

Hinder L, Pfaff AL, Emmerich RE, Michels S, Schlitzer M, Culmsee C. Characterization of novel diphenylamine compounds as ferroptosis inhibitors. J Pharmacol Exp Ther. 2021, JPET-AR-2021-000534. doi: 10.1124/jpet.121.000534

Table of content

1. Introduction.....	1
1.1. Regulated cell death	1
1.2. The role of oxidative stress in neurodegeneration.....	2
1.3. Oxytosis and ferroptosis	3
1.4. The BCL-2 family	8
1.4.1. <i>BCL-2 family members in oxidative cell death</i>	9
1.5. The BH3-interacting domain death agonist BID	10
1.5.1. <i>BID structure</i>	10
1.5.2. <i>Function of BID in apoptosis</i>	11
1.5.3. <i>The role of BID in neuronal cell death</i>	13
1.5.4. <i>Pharmacological inhibitors of BID and oxidative cell death</i>	14
1.6. Aims	17
2. Materials and methods.....	18
2.1. Software	18
2.2. Cell Culture	19
2.2.1. <i>Standard solutions for cell culture</i>	20
2.2.2. <i>Splitting of the cells</i>	21
2.3. Cell death induction.....	22
2.3.1. <i>Induction of cell death by compounds</i>	22
2.3.2. <i>t-BID induced cell death</i>	23
2.4. Inhibition of cell death.....	23
2.5. Assessment of cell viability	24
2.5.1. <i>Microscopic images</i>	24
2.5.2. <i>MTT assay and EC-50 determination</i>	24
2.5.3. <i>XCELLigence measurements</i>	25
2.6. Flow cytometry measurements	26
2.6.1. <i>DCF assay</i>	27

2.6.2. BODIPY assay	28
2.6.3. MitoSOX assay.....	29
2.6.4. TMRE assay	30
2.6.5. Annexin V FITC/ PI assay	31
2.7. DPPH assay.....	32
2.8. Glutathione assay	32
2.9. Analysis of protein levels	34
2.9.1. BCA assay.....	35
2.9.2. Polyacrylamid gel electrophoresis (PAGE).....	35
2.9.3. Western blot.....	37
2.10. Mitochondrial analysis.....	39
2.10.1. Mitochondrial morphology and categorization	39
2.10.2. Seahorse measurements	40
2.10.3. ATP measurement	41
2.11. Isolation of mitochondria from rat brains	42
2.11.1. Seahorse measurements in isolated mitochondria	44
2.12. <i>In silico</i> ADME and toxicity analysis	46
2.13. Protein Purification	47
2.13.1. Bid3CCSS-GST construct.....	47
2.13.2. Buffers and solutions for protein purification.....	47
2.13.3. Bid3CCSS expression.....	49
2.13.4. Protein purification.....	49
2.13.5. Cell lysis.....	50
2.13.6. Glutathione affinity chromatography	50
2.13.7. Coomassie staining.....	51
2.13.8. Thrombin cleavage	52
2.13.9. Size exclusion chromatography (SEC).....	53
2.13.10. Mass spectrometry	54
2.13.11. Buffer exchange.....	54

2.14.	Protein crystallization	55
2.14.1.	<i>Crystallization technique</i>	56
2.14.2.	<i>Seeding</i>	56
2.14.3.	<i>Harvesting and measurements of the crystals</i>	57
2.14.4.	<i>Crystal data analysis and structural refinement</i>	57
2.14.5.	<i>Heavy metal soaking</i>	57
2.14.6.	<i>Compound co-crystallization/ Soaking</i>	57
2.15.	Microscale thermophoresis assay (MST)	58
2.16.	NMR measurements	60
2.17.	Statistical analysis	61
3.	Results	62
3.1.	BID Crystallization	62
3.1.1.	<i>Bid3CCSS purification</i>	62
3.1.2.	<i>Optimization of the Bid3CCSS crystallization conditions</i>	66
3.1.3.	<i>First crystal structure of Bid3CCSS</i>	72
3.1.4.	<i>Functional analysis of the Bid3CCSS protein</i>	73
3.2.	Characterization of novel diphenylamine compounds as ferroptosis inhibitors	76
3.2.1.	<i>Erastin and RSL-3 induced cell death in HT22 cells</i>	77
3.2.2.	<i>Time dependent development of ferroptosis hallmarks</i>	80
3.2.3.	<i>DPA compounds provided protection against ferroptosis</i>	82
3.2.4.	<i>Investigations on potential neurotoxicity</i>	87
3.2.5.	<i>Major ROS dependent hallmarks of ferroptosis were effectively blocked by the novel compounds</i>	88
3.2.6.	<i>Upstream cascade of ferroptosis was not affected by DPA compounds</i>	92
3.2.7.	<i>DPA compounds preserved mitochondrial membrane potential and morphology</i>	94
3.2.8.	<i>DPA compounds maintain mitochondrial respiration and function</i>	96
3.2.9.	<i>Confirmation of the results in the mouse hypothalamus cells</i>	98
3.2.10.	<i>Post-treatment time windows after ferroptosis induction</i>	102
3.2.1.	<i>Approaches to investigate BID as a target structure for the novel DPA compounds</i>	104

4. Discussion.....	112
4.1. BID crystallization	113
4.2. Characterization of novel DPA compounds as ferroptosis inhibitors	119
5. Summary	130
6. Zusammenfassung	132
7. Abbreviations	134
8. References.....	139
9. Publications and presentations	147
10. Meetings and conferences	147
11. Acknowledgments/ Danksagung.....	148
12. Curriculum vitae	150

1. Introduction

1.1. Regulated cell death

The first reports of research on regulated cell death (RCD) were published by Karl Vogt in 1842. In his studies on vertebrates, he noticed the phenomenon of physiological cell death during developmental processes^{1,2}. However, it was not until 1972 that Kerr and colleagues identified distinct morphological patterns of dying cells. Kerr described cell shrinkage (pyknosis), membrane blebbing, apoptotic body formation as well as DNA fragmentation and condensation³, and termed this phenomenon apoptosis. Later, apoptosis (type I cell death) was categorized separately from autophagic cell death which is characterized by extensive vacuolization of the cytoplasm (type II cell death) and necrosis (type III cell death)⁴.

Since then, the term regulated cell death has considerably developed. Nowadays, RCD is defined as cell death originating from intra- or extracellular impairments. When RCD takes place in developmental processes it is called programmed cell death (PCD). In contrary to RCD, accidental cell death (ACD) is defined that occurs due to severe physical, chemical or mechanical harm which is not modulated via a molecular machinery and hence could not be addressed by therapeutics^{5,6}.

Additionally, the understanding of necrosis has evolved. Initially, necrosis was described as an unregulated form of cell death, but then several controlled forms of necrosis were discovered, such as necroptosis, ferroptosis, oxytosis, among others. The different types of RCD are distinct from each other by the defined cell death inducers and/ or inhibitors, the involved proteins and compartments as well as the contribution of reactive oxygen species (ROS)^{7,8}. However, current research indicates that these cell death pathways are highly interconnected rather than individual mechanisms for distinct purposes^{5,9}.

1.2. The role of oxidative stress in neurodegeneration

RCD is often associated with oxidative stress evoked by ROS². ROS are produced via exogenous (environmental) or endogenous sources. A significant proportion of endogenous ROS occur in the mitochondrial energy metabolism via direct reduction of oxygen in the electron transport chain¹⁰. Additionally, ROS arise in cell compartments apart from mitochondria like the endoplasmic reticulum during oxidative modifications or degradation processes of proteins^{11,12}. Usually, ROS generation and ROS degradation via enzymatic or non-enzymatic reactions are in a regulated balance (Figure 1). When the homeostasis between the oxidative and antioxidative machinery is disturbed, this results in oxidative stress^{13,14}, which then could harm biomolecules, like DNA, RNA, lipids, and proteins or can interfere with processes, like lipid peroxidation¹⁵. Neurons are in particular at high risk for ROS toxicity due to their high metabolic activity and associated high energy demand which is mainly met by intense mitochondrial respiration.

Hence, many chronic neurodegenerative disorders are currently attributed to oxidative stress, like Alzheimer's disease (AD)^{16,17} or Huntington's disease (HD)¹⁸. Moreover, acute brain insults induced by hypoxia or ischemia could result in increased ROS accumulation that promote neuronal cell death^{19,20}.

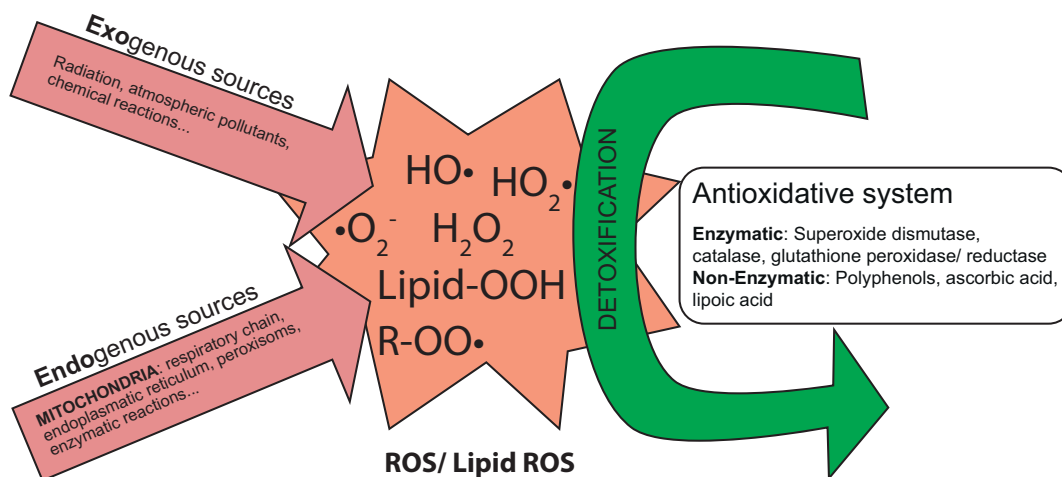


Figure 1. Oxidative stress. Formation of different reactive oxygen species by exogenous and endogenous sources. Endogenously, ROS originate mainly from mitochondria by electrons leaking between complexes I and III of the electron-transport chain and through NADPH-oxidase. Detoxification takes place in enzymatic or non-enzymatic reactions^{15,21}.

1.3. Oxytosis and ferroptosis

Already in 1986 it was found that excessive glutamate treatment led to cell death in a neuronal hybridoma N18-RE-105 cell line²². The authors already assumed that glutamate caused an inhibition of the X_C^- -system (or xCT). Under physiological conditions this system is predominantly expressed in the brain²³, where its main function is the transport of cystine into the cell in exchange for glutamate in a 1:1 ratio following their respective concentration gradients²⁴. The X_C^- -antiporter consists of two subunits with the heavy chain 4F2 (SLC3A2) and the light chain xCT (SLC7A11) linked by disulfide bridges.

Inhibition of the X_C^- -system results in an intracellular cysteine depletion, the rate limiting amino acid for glutathione (GSH) synthesis²⁵. GSH in turn is the main component of the antioxidative machinery in neuronal cells²⁶.

In 2001, studies by David Schubert and Pamela Maher in the neuronal HT22 cell line confirmed the previously assumed mechanism of action and coined the name oxytosis for this form of glutamate induced oxidative cell death. Importantly, the HT22 cell line lacks ionotropic NMDA receptors, so excitotoxicity due to massive calcium influx upon excessive glutamate treatment could be excluded²⁷. This type of cell death was independent of caspases since no caspase-3 activation was detected and pan-caspase inhibition via the commonly-used z-VAD-fmk inhibitor did not prevent oxytosis²⁷⁻²⁹. Therefore, it could be clearly separated from caspase-dependent apoptosis.

The depleted GSH levels cause a significant impairment of the function of the selenoprotein glutathione peroxidase 4 (GPX4), the only member of the GPX family that is able to detoxify hydroperoxides in complex biomolecules like lipids or phospholipids in the cell^{30,31} (Figure 2).

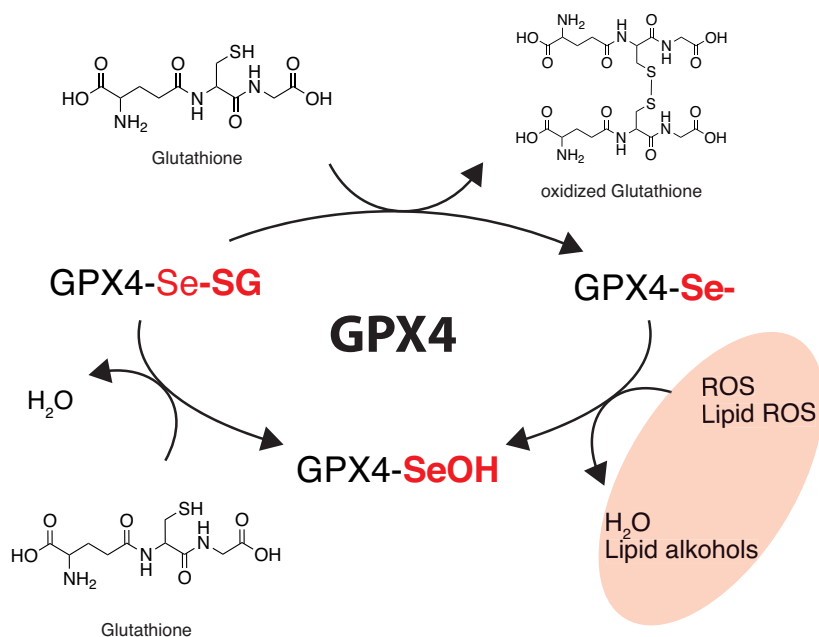


Figure 2. Detoxification cycle of ROS/ lipid ROS via GPX4. The detoxification reaction is shown in the orange area. Selenolate (Se⁻) reacts with ROS or lipid peroxides (Lipid ROS), whereby the selenolate was oxidized to the respective selenenic acid (SeOH) and to water or lipid alcohols. To regenerate the selenolate group, GPX4-SeOH first reacts with glutathione (Se-SG) by water elimination. In a second step, a further GSH molecule reacts with the GPX4 bound glutathione, thereby releasing the free selenolate (Se⁻) group, which can enter the next detoxification cycle. The figure was modified from Flohé et al. ³⁰.

The involvement of the GPX4 enzyme in the oxidative cell death paradigm was confirmed by experiments using inducible GPx4 gene knock-out in mice as well as experiments with RSL-3, a compound that directly inhibits and downregulates GPX4 ³²⁻³⁵. As a consequence, the activity of lipoxygenases increases, i.e. ALOX12-15, which causes enhanced cytosolic ROS formation as well as lipid peroxidation, which finally resulted in oxidative cell death ^{32,36}.

In 2003, a screen for anticancer drugs identified the small molecule erastin that killed tumor cells through a mechanism different from apoptosis ³⁷. Later in 2012, the group of Brent Stockwell demonstrated the essential role of iron in this cell death pathway, since iron supply, but not the application of other metal ions like Cu²⁺, Mn²⁺, Ni²⁺ and Co²⁺ could increase the toxic effects evoked by erastin ³⁸. Moreover, co-treatment with the iron chelator deferoxamine (DFO) could block the observed detrimental effects of erastin. As a result, the group named this cell death pathway ferroptosis (ferrum (latin) = iron; apóptosis (ancient greek) = "falling off") ³⁸.

Iron is not only crucial in the oxygen transport and supply in the body, but is also obligate for redox homeostasis in the cells and, therefore, incorporated in many enzymes of the redox system like i.e., in NAD(P)H dehydrogenases and lipoxygenases^{39,40}. However, an overload of free iron in the labile iron pool of the cell facilitates ferroptosis via the Fenton reaction, in which Fe^{2+} is oxidized to Fe^{3+} under the formation of reactive oxygen species. Nevertheless, the specific role of iron in ferroptosis is still not yet fully understood and needs further investigation^{41,42}.

Furthermore, it was demonstrated that erastin is also a XC⁻-system inhibitor³⁸. Therefore, similar to oxytosis, erastin treatment caused a depletion in intracellular cysteine levels³⁸, ROS development³¹ and elevated lipid peroxidation, which usually occurs on polyunsaturated fatty acids (PUFA) from phospholipids^{43,44}. Therefore, it is suggested that oxytosis and ferroptosis were very closely related or even synonyms for the same cell death cascade^{31,45}. The key features of those oxidative cell death pathways have been found in several models of acute and chronic neurodegenerative disorders shown in the figure below (Figure 3).



Figure 3. Oxytosis/ Ferroptosis in neurodegenerative diseases. The key hallmarks of oxytosis and ferroptosis, including iron dependency, GPX4 deregulation and lipid ROS formation were found in AD⁴⁶⁻⁴⁸, Parkinson's Disease (PD)⁴⁹⁻⁵¹, Friedreich's ataxia^{52,53}, HD^{51,54} as well as in traumatic brain injury and cerebral ischemia⁵⁵⁻⁵⁸.

Several inhibitors targeting different parts of the detrimental oxidative cell death cascade have already been established. The small molecule ebselen abrogates oxidative cell death in different cell lines due to a GPX4 mimetic activity ^{38,59}. Furthermore, the 5-LOX inhibitor Zileuton ⁵⁹ or 12/15-LOX inhibitor PD146176 ³⁶ as well as ROS and lipid ROS scavengers such as Trolox ³⁸, ferrostatin-1 ^{35,60} and liproxstatin-1 ⁶¹ prevented oxytosis and/ or ferroptosis.

In addition, there is increasing evidence for a significant role of mitochondria in oxytosis and ferroptosis. Already in early descriptions of these oxidative cell death pathways, mitochondrial alterations were observed ^{38,62} although increased mitochondrial ROS formation was not found in HT1080 upon erastin treatment ³⁸. Nevertheless, erastin has been hypothesized to directly target mitochondria as a VDAC2,3 opener inducing impairments of the mitochondrial membrane potential ⁶³. Additionally, the apoptosis inducing factor (AIF), normally located at the inner mitochondrial membrane, was found to participate in the execution of the final steps of oxytosis ⁵⁵ as well as ferroptosis ³⁵. Moreover, mitochondrial protection using mitochondrial ROS scavengers like XJB-5-131 or MitoQ prevented oxidative cell death in different cell lines upon RSL-3 as well as erastin treatment ^{35,64}. In addition, the BH3 interacting domain death agonist (BID) plays an important role in these oxidative cell death pathways to transfer the upstream ROS dependent effects to the mitochondria ^{29,36,45}.

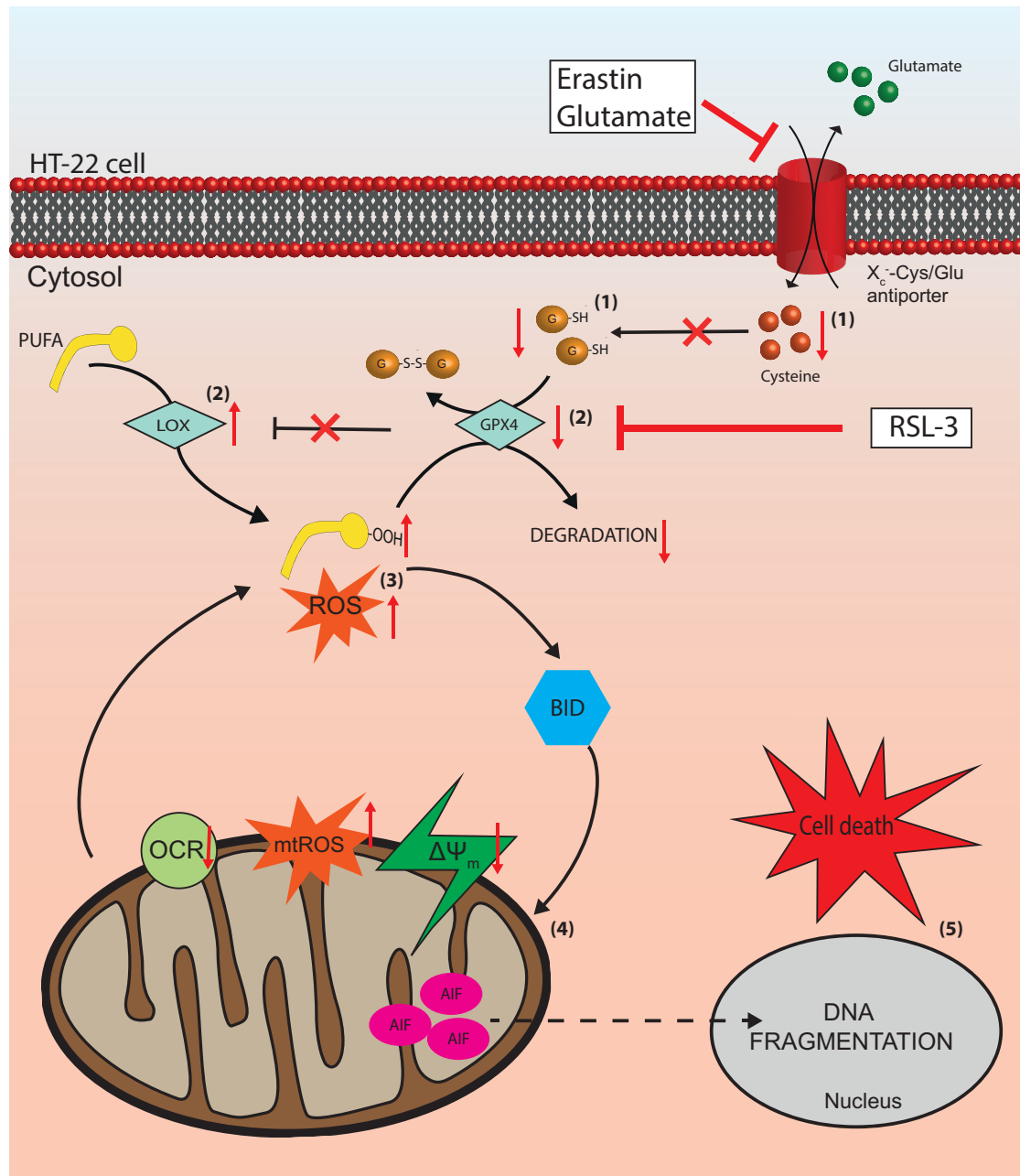


Figure 4. Model of oxystosis and ferroptosis in HT22 cells. Oxidative cell death in HT22 cells is initiated by X_c^- -transporter inhibition via erastin or glutamate treatment. Consequently, cysteine and glutathione levels drop (1). Hence, GPX4 function is impaired (2) and the activity of lipogeneses (i.e., LOX 12/15) is increased (2) resulting in enhanced ROS and lipid ROS levels in the cell (3). This effect could also be evoked via RSL-3 treatment, which directly inhibits and depletes the GPX4 protein. Following ROS and lipid ROS development, mitochondrial impairments occur including a decrease of the mitochondrial membrane potential, mitochondrial ROS formation, decreased mitochondrial respiration as well as mitochondrial fragmentation, which is associated with a release of AIF (4) to finally execute cell death (5). Thereby, the pro-apoptotic protein BID is discussed to transfer the upstream ROS dependent effects to mitochondria. GSH (glutathione); GSSH (oxidized glutathione); PUFA (polyunsaturated fatty acids); PUFA-OOH (lipid ROS); LOX (lipogeneses); ROS (reactive oxygen species); $\Delta\Psi_m$ (mitochondrial membrane potential), mtROS (mitochondrial ROS), OCR (oxygen consumption rate \cong mitochondrial respiration), AIF (apoptosis inducing factor).

1.4. The BCL-2 family

B-cell lymphoma-2 (BCL-2) proteins are tightly connected to the intrinsic apoptosis pathway which is also called the mitochondrial pathway of apoptosis. In contrast to the extrinsic pathway of apoptosis, which is induced by the binding of the FAS ligand or TNF to their respective cell death receptors, the intrinsic pathway is initialized through unspecific factors such as i.e., ROS, ER stress, DNA damage, or others ⁵. However, both pathways are closely interconnected ⁶⁵. Especially in Type II cells, FAS-induced cell death also switches to the mitochondrial apoptosis pathway after caspase-8-mediated cleavage and mitochondrial trans-activation of the Bcl-2 family member BID ⁶⁶.

Activators of intrinsic apoptosis alter the sensitive balance within the pro-apoptotic and anti-apoptotic BCL-2 proteins in the cell which can decide between life or death. The members of this family are structurally related, each possessing at least one BCL-2 homology (BH) domain. The anti-apoptotic (BCL-2, BCL-XL, BCL-W, MCL-1, A1...) as well as pro-apoptotic (BAX, BAK) proteins contain four BH motifs (BH1-4) ⁶⁷. Notably, the function of BAK is different in neurons compared to other mitotic cells, since BAK is only expressed as an alternative splicing variant (N-BAK) in the brain, which then functions as an anti-apoptotic protein ⁶⁸.

On the other hand, the aforementioned BID as well as BAD, BIK, BIM, NOXA and PUMA share only the BH3 domain with the members of BCL-2 family and are therefore referred to as BH3-only proteins ⁶⁵. The BH3-only proteins serve as regulators of the intrinsic apoptosis cascade and are genetically upregulated or activated e.g. upon p53 activation ^{69,70}, ER stress ⁷¹ or caspase cleavage ⁷². Under physiological conditions BAX and BAK are bound to anti-apoptotic BCL-2 family members, such as BCL-2 and BCL-XL, so that apoptosis is inhibited ⁶⁵. BH3-only members can initiate apoptosis either by binding anti-apoptotic BCL-2 family members ⁷³⁻⁷⁵ or by direct activation of BAX and BAK ⁷⁶⁻⁷⁸. This leads to BAX or BAK oligomerization at the mitochondrial outer membrane causing mitochondrial membrane permeabilization (MOMP) ⁷⁹⁻⁸¹ and the release of pro-apoptotic mitochondrial proteins such as the apoptosis inducing factor (AIF), cytochrome c or Smac/DIABLO ^{75,82,83}. Cytochrome c and APAF 1 initiate apoptosome formation that subsequently activates caspase-9 ^{82,84} promoting further cell death ⁷⁵. Smac/DIABLO additionally support caspase-9 activation by inhibition of IAPs (inhibitor of apoptosis proteins), whereas AIF release results in DNA fragmentation in the nucleus ⁸².

1.4.1. BCL-2 family members in oxidative cell death

The pivotal role of the BCL-2 family members in apoptosis is well-established, although their contribution in caspase-independent oxidative cell death paradigms like oxytosis and ferroptosis is still under debate.

Primary BAX^{-/-} neuron cultures were resistant to apoptotic cell death induced by staurosporine, even though no protection was demonstrated when these KO cells were exposed to oxidative glutamate toxicity⁸⁵. In contrast, experiments using BAX^{-/-} HT22 neurons suggest a role for the BAX protein in the oxidative cell death pathway⁸⁶. Moreover, Bax/Bak double KO mouse embryonic fibroblasts (MEF cells) still responded to erastin and RSL-3 treatment with mitochondrial impairments and increased cell death^{38,87}. However, treatments with BAX/BAK oligomerization inhibitors protected primary neurons from glutamate induced excitotoxic cell death⁸⁸.

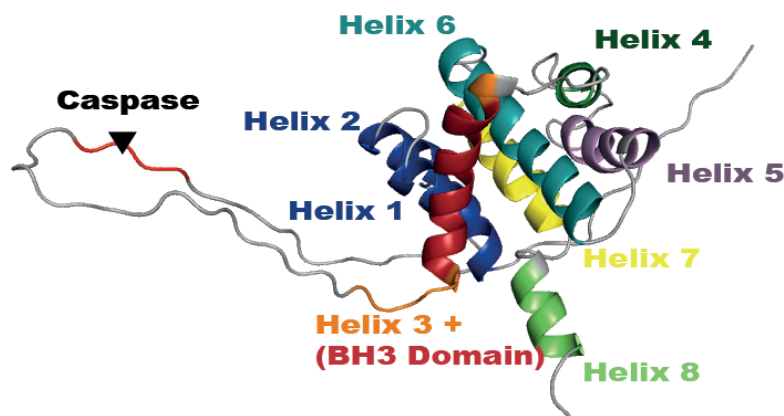
The KO of the anti-apoptotic BCL-XL protein only resulted in a slight increased susceptibility to glutamate toxicity in embryonic fibroblasts. This effect could be due to a direct increase in oxidative stress and mitochondrial damage due to Bcl-XL deletion, although these effects were at least partially compensated by enhanced glutathione synthesis⁸⁹. In addition, HT22 cells treated with cholera toxin and vasoactive intestinal peptide (VIP) showed enhanced resistance against glutamate toxicity, and concomitant upregulation of the BCL-2 protein was detected⁹⁰⁻⁹². It was suggested by the authors that BCL-2 supported the antioxidative defense via GSH upregulation or probably via a direct antioxidative effect of the BCL-2 protein^{90,91,93}.

Besides the undefined roles of the aforementioned BCL-2 family members in the oxidative cell death paradigm, many studies strongly indicate an involvement of the BH3-interacting domain death agonist (BID) in caspase-independent oxidative cell death in neurons as described in detail in 1.5.3..

1.5. The BH3-interacting domain death agonist BID

1.5.1. BID structure

BID is a protein of 195 amino acids in its full-length form. There are two descriptions of BID NMR structures available ^{94,95}. BID is constructed of eight α -helices containing a core of two central hydrophobic helices (H6, H7) which are surrounded by amphiphilic helices. Furthermore, there is a highly exposed, unstructured loop between helix 2 and helix 3 ⁹⁶ (Figure 5). Thus, BID is structurally more closely related to the multi-region BCL-2 family members like BAX and BCL-XL than to the other BH3-only members which were described as unstructured proteins ⁹⁷.



```

1MDSEVSNGLGAEHITDLLVFGFLQSSGCTROELEVLRRELVPVQAYWEADLEDELQTDGSQASR
                H1                H2
SFNQRIEPDSESQEEIIHNIARHLAQIGDEMDHNIQPTLVROLAAQFMNGSLEEDKRNNCLAKALD
                H3                H4                H5
EVKTAFPRDMMENDKAMLIMTMLLAKKVASHAPSLLRDVFHHTTVNFINONLFSYVRNLVRNEMD195
H5                H6                H7                H8

```

Figure 5. Mouse BID NMR structure (PDB: 1DDB) and respective amino acid sequence.

However, high resolution crystal structures of the BID protein, which remain the gold standard for determination of the spatial, three-dimensional arrangement of the amino acids within a protein, are still missing ⁹⁸. The significance of a crystal structure is demonstrated by data derived from the PDB data bank, where today nearly 160,000 X-ray crystal structures were deposited. In contrast, the number of available NMR structures reaches just below 13,500.

The first attempts to crystallize the BID protein were started by Dr. Sina Oppermann and Dr. Anja Jelinek. During their work, several BID constructs have been created and purified. These BID constructs were then transferred to the

MarXtal crystallization lab (SYNMICRO, University of Marburg, Germany) where several high-throughput crystallization screens were conducted. In the thesis of Dr. Sina Oppermann was noticed that the flexible N-terminus of the full-length BID construct (Bid22) hinders crystal formation⁹⁹. Therefore, the Bid3 construct was developed lacking this flexible loop (AS 13-47). In addition, both cysteine residues of the Bid3 protein were exchanged to serine (Bid3CCSS) to prevent glutathione binding to the Bid3 protein in order to enhance the protein homogeneity to facilitate crystallization¹⁰⁰. Using this Bid3CCSS construct, it was possible to continuously obtain small, ingrown crystals which were, however, of insufficient quality to gain an X-ray data set for solving the crystal structure of the BID protein.

mouse Bid	1	MDSEVSNGLGAEHITDLLVFGFLQSSGCTRQEEVLGRELFPVQAYWEADLEDELQTDGSQASRSFNQRIEPTDSE	78
Bid22	1	MDSEVSNGLGAEHITDLLVFGFLQSSGCTRQEEVLGRELFPVQAYWEADLEDELQTDGSQASRSFNQRIEPTDSE	78
Bid3	1	-----GS-AEHITDLLVFGFLQSSGCTRQEEVLGRELFPVQAY-----	37
Bid3CCSS	1	-----GS-AEHITDLLVFGFLQSSGSTRQEEVLGRELFPVQAY-----	37
mouse Bid	62	SQEEIIHNIARHLAQIGDEMDHNIQPTLVRQLAAQFMNGSLSEEDKRNCLAKALDEVKTAFFPRDMENDKAMLIMTML	154
Bid22	62	SQEEIIHNIARHLAQIGDEMDHNIQPTLVRQLAAQFMNGSLSEEDKRNCLAKALDEVKTAFFPRDMENDKAMLIMTML	154
Bid3	38	SQEEIIHNIARHLAQIGDEMDHNIQPTLVRQLAAQFMNGSLSEEDKRNCLAKALDEVKTAFFPRDMENDKAMLIMTML	114
Bid3CCSS	38	SQEEIIHNIARHLAQIGDEMDHNIQPTLVRQLAAQFMNGSLSEEDKRNCLAKALDEVKTAFFPRDMENDKAMLIMTML	114
mouse Bid	124	LAKKVASHAPSLLRDVFHTTVNFINQNLFSYVRNLVRNEMD	195
Bid22	124	LAKKVASHAPSLLRDVFHTTVNFINQNLFSYVRNLVRNEMD	195
Bid3	84	LAKKVASHAPSLLRDVFHTTVNFINQNLFSYVRNLVRNEMD	155
Bid3CCSS	84	LAKKVASHAPSLLRDVFHTTVNFINQNLFSYVRNLVRNEMD	155

Figure 6. Sequence alignment of mouse BID and the Bid constructs. Mouse BID sequence was retrieved from Uniprot (P70444) and sequences for Bid constructs was derived from the thesis of Dr. Anja Jelinek¹⁰⁰.

1.5.2. Function of BID in apoptosis

To activate BID in apoptosis, the 22 kDa full-length BID protein is cleaved within the unstructured loop usually by caspase-8 (Figure 5) into the C-terminal p15 fragment (truncated BID; t-BID) and the N-terminal p7 fragment^{72,101}. However, several other proteins could also truncate BID including granzyme B, lysosomal proteases, caspase-3, calpains and cathepsins⁹⁶. The cleavage procedure is regulated via phosphorylation of BID in close proximity to the cleavage site¹⁰².

Remarkably, it remains controversial why BID cleavage is necessary in the apoptotic paradigm. It is well-established that the BH3 domain of BID is required for the interaction with pro- and anti-apoptotic BCL-2 family proteins^{103,104}. Prediction data of BID cleavage by caspase-8 suggested that the truncation resulted in an exposure of a previously buried hydrophobic area of the BH3 domain⁹⁵ which might facilitate this interplay. Other studies stated that cleavage

of the BID protein does not have a significant impact on its general structure and causes rather small structural changes. Therefore, it was suggested that the unstructured loop could possibly function as an intrinsic inhibitor of the BID function⁹⁴.

After cleavage, the resulting p15 fragment t-BID and the p7 fragment are still tethered together through hydrophobic interactions and finally fall apart when reaching the outer mitochondrial membrane^{72,105} due to conformational changes of t-BID upon membrane binding⁶⁷. Several proteins are discussed for being mitochondrial t-BID receptors such as the mitochondrial phospholipid cardiolipin^{104,106,107} and/ or the mitochondrial carrier homolog 2 (MTCH2) which is possibly associated with the Modulator of apoptosis-1 (MOAP-1) to facilitate t-BID binding^{108–111}. Furthermore, BID myristylation at the cleavage site is proposed to mediate insertion into the mitochondrial membrane¹⁰². BID binding to mitochondria results in a marked mitochondrial accumulation of t-BID^{112–114} which prompted the activation and oligomerization of the pro-apoptotic BAX and BAK molecules^{76,115} and the inhibition of the inhibitory BCL-2 and BCL-XL proteins¹⁰³. These interactions ultimately result in mitochondrial membrane permeabilization and cytochrome c release¹⁰⁵.

In addition, it was demonstrated that BID binding *per se* leads to mitochondrial fragmentation via direct binding to the Optic Atrophy 1 protein (OPA-1)^{116,117} or direct interaction with the voltage dependent anion channel (VDAC)^{118,119}, a channel which was reported to be crucially involved in the intrinsic apoptotic pathway^{120–122}.

Moreover, BID shows structural similarities to some bacterial pore-forming toxins and, indeed, a ion-channel activity could be demonstrated by t-BID in planar bilayers¹²³. Furthermore, there are studies suggesting that BID contributes to mitochondrial impairment via direct BID-BAX hetero-oligomerization¹²⁴ or even through t-BID homo-oligomerization^{104,125,126}. Moreover, it was demonstrated in hepatocytes¹²⁷ and in the cardiomyocyte cell line H9c2 that BID activation resulted in ROS development during apoptosis that additionally promote cell death progression^{127,128}. The authors assume that BID induced ROS production might be mediated by a disturbance in complex III at the electron transport chain, caspase-dependent disruption of complex I or II or possibly due to induction of mitochondrial permeability transition¹²⁷.

1.5.3. The role of BID in neuronal cell death

BID is of central importance in neuronal cell death pathways. Unlike other proteins of the BCL-2 family i.e., BAK and BCL-2, immunostaining and immunoblotting revealed that BID is still highly expressed in most regions of the mature mouse brain ¹²⁹. Furthermore, Bid-deficient mice were significantly protected from ischemic brain damage and showed starkly reduced infarct volumes in a model of cerebral artery occlusion ^{130,131}. This protective effect was additionally confirmed in a model of controlled cortical impact (CCI) in mice, where BID deletion also resulted in a reduced infarct volume ¹³². Interestingly, in neurons, full-length BID was able to co-localize to mitochondria, where it mediated an impairment in mitochondrial membrane potential upon glutamate treatment in a caspase-independent mechanism ^{133,134}.

Further, Bid gene silencing using Bid siRNA prevented HT22 neurons from glutamate induced cell death by suppressing mitochondrial damage as well as the release of AIF ²⁹. AIF was previously shown to drive delayed neuronal cell death that occurs several hours after ischemia-reperfusion injury through a caspase-independent mechanism ^{135,136}.

Furthermore, Bid KO using the CRISPR/ Cas9 method in the neuronal HT22 cells strikingly abrogated mitochondrial ROS as well as lipid ROS formation and preserved mitochondrial morphology and function in models of oxytosis and ferroptosis. As a consequence, the Bid KO cells maintained cell viability after exposure to glutamate or erastin ^{137,138}. Interestingly, studies demonstrated that BID plays a role in phospholipid trafficking to mitochondria ^{112,126,139} and therefore might directly contribute to lipid peroxide formation in the mitochondrial membranes during the oxidative dysregulation in ferroptosis.

1.5.4. Pharmacological inhibitors of BID and oxidative cell death

First BID inhibitors

The first small-molecule BID inhibitors BI-6c9 and BI-11A7 (Figure 7) were developed by Becattini and colleagues using an NMR-based approach^{140,141}. These compounds could be fitted in a hydrophobic groove of the BID NMR structure. However, an extensive *in silico* search for novel BID inhibiting compounds failed due to the limited quality of the BID NMR structures. Binding of the compounds to the BID protein was further confirmed via NMR measurements using ¹⁵N-labeled BID^{140,141}. In primary rat neurons, BI-6c9 and BI-11A7 inhibited oxygen-glucose deprivation induced cell death^{19,141}, although BI-11A7 showed cytotoxicity at concentrations higher than 20 μ M. *In vitro*, BI-6c9 prevented cell death induced by t-BID overexpression, glutamate or erastin treatment in various cell culture experiments including the hippocampal HT22 neurons, HeLa and MEF cells. These protective effects were attributed to pronounced mitochondrial protection by the compound^{29,35,36,45,142–144}. Unfortunately, BI-6c9 was not applicable to *in vivo* studies due to their poor solubility¹⁴⁰ and their poor bioavailability.

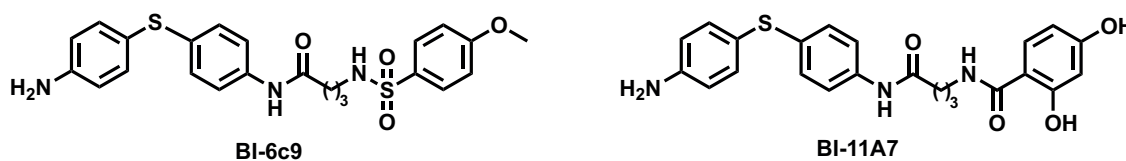


Figure 7. First developed BID inhibitors by Becattini and colleagues^{140,141}.

Inhibitor development based on BI-6c9 as a scaffold molecule

To generate improved BID compounds, BI-6c9 was modulated using a medicinal chemistry approach by replacing the metabolically unstable 4-(4-aminophenyl) sulfanylaniline moiety¹⁴⁵ and reducing the flexibility¹⁴⁶. The mentioned strategies resulted in a series of 4-phenoxyaniline derivatives¹⁴⁵ and N-phenyl-substituted thiazolidinediones¹⁴⁶ (Figure 8). These compounds were tested in HT22 cells in the model of glutamate-induced oxytosis. Compound 14 and 40 were the most potent 4-phenoxyaniline cell death inhibitors in this paradigm, and for the N-phenyl-substituted thiazolidinediones, compounds 6, 7 and 16 provided the best inhibition potency with EC50 values between 6.78-9.87 μM .

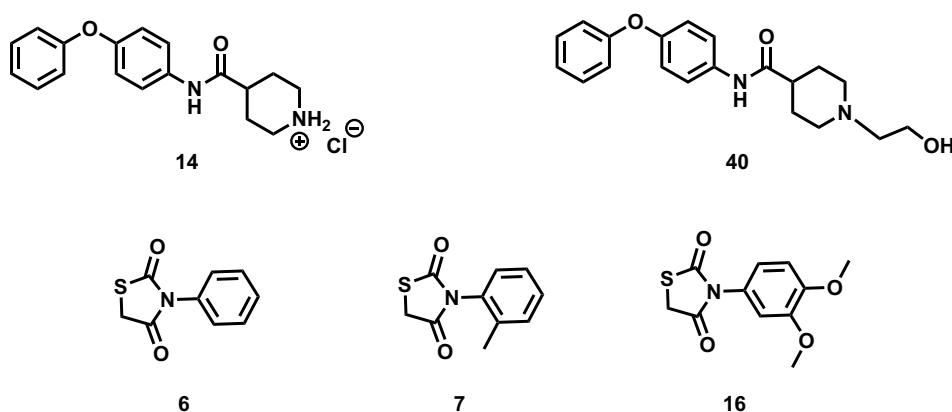
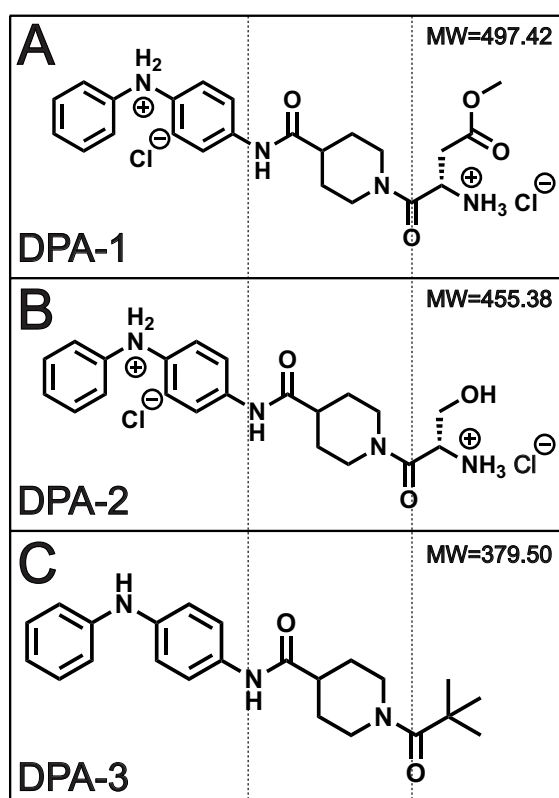


Figure 8. BID inhibitors designed by a medicinal chemistry approach using BI-6c9 as a scaffold molecule. In this figure, the most potent BID inhibitors are depicted based on the 4-phenoxyaniline structure (compounds 14 and 40)¹⁴⁵ and on the N-phenyl-substituted thiazolidinedione structure (compounds 6,7 and 16)^{99,146}.

Evidence for the BID-targeting mechanism of the compounds was provided by the protective effects in a t-BID overexpression assay and docking studies^{145,146}. Furthermore, for the N-phenyl-substituted thiazolidinediones, a binding to recombinant, immobilized BID was shown by a cell-free binding assay. However, xCELLigence measurements revealed that only transient protection against glutamate toxicity was reached at lower concentrations (<25 μM) for both compound classes. For sustained protection, inhibitor concentrations of 25-50 μM were needed. Moreover, the ability for mitochondrial protection in oxytosis was further analyzed for the thiazolidinedione derivatives. Mitochondrial parameters such as mitochondrial membrane potential and mitochondrial respiration were maintained at concentrations of 20 μM .

All in all, the thiazolidinediones and 4-phenoxyaniline derivatives were very effective in preventing t-BID induced cell death, although in the oxidative cell death paradigm the compounds were less effective than BI-6c9 which provided full protection in a concentration of 10 μM ^{145,146}.

Therefore, in the doctoral thesis of Dr. Anna Lena Pfaff, novel compounds were developed under consideration of the previously discussed findings to increase the inhibitory effect against oxidative cell death ¹⁴⁷. The diphenylthioether of the scaffold compound BI-6c9 was replaced by a diphenylamine (DPA) structure to additionally insert an antioxidant moiety. The antioxidative effect of the diphenylamine structure is due to the relatively labile N-H bond which is prone to transfer its H-atom in a radical reaction ^{148,149}. Moreover, as already established for the previous compounds, the central γ -aminobutyric acid-linker sequence of BI-6c9 was exchanged by the more rigid piperidine-4 carboxamide structure to ensure



less flexibility of the compounds. The piperidyl-N-substituent was individually designed, whereby the esterified aspartic acid (Figure 9 A) the serin derivative (Figure 9 B) and the tert-butyl residue (Figure 9 C) provided the best inhibition properties in a first preliminary MTT screening upon the addition of glutamate ¹⁴⁷.

Figure 9. Structure of novel inhibitors against oxidative cell death. A) DPA-1 compound (Schl-30172); **B)** DPA-2 compound (Schl-30174), **C)** DPA-3 compound (Schl-30736).

However, it remains to be investigated, whether the compounds are also effective in the ferroptosis paradigm and how the compounds interfere with the oxidative cell death cascade to exert their protective effects.

1.6. Aims

In the last decade, *in vitro* and *in vivo* studies showed that caspase-independent oxidative cell death mechanisms like oxytosis and ferroptosis are dominant in dying neurons. The related hallmarks such as ROS and lipid ROS formation, and mitochondrial demise were found in several neurodegenerative diseases. For promoting these deleterious effects, the BID protein is central and thus provides a promising target for drug development. Therefore, pharmacological BID inhibitors were developed that protected neuronal cells from oxidative cell death, however, with limited potency. Additionally, structure-based BID inhibitor design has been constrained in the past due to the lack of high-resolution X-ray data of the BID protein, as the gold standard for accurate structure determination.

In the first part of the thesis, approaches for BID crystal structure determination were continued based on previous work conducted by Dr. Oppermann and Dr. Jelinek. The best crystallization conditions for the established Bid3CCSS construct were further optimized in order to develop a protocol that aimed at yielding crystals sufficient for high resolution X-ray measurements to determine the BID protein structure.

In the second part of this thesis, novel promising diphenylamine (DPA) compounds (DPA 1-3) were extensively investigated in model systems of ferroptosis with the following objectives:

1. Elucidating the inhibition potency and specificity against ferroptotic cell death.
2. Clarifying the potential role of abrogation of different reactive oxygen species, including cytosolic, lipid and mitochondrial ROS in the protective mechanism.
3. Unravelling a potential protective interaction with the upstream antioxidative machinery including effects on glutathione levels and GPX4 expression.
4. Characterizing the contribution of mitochondrial protection as part of the mechanism of action.
5. Deciphering BID-binding as a putative target structure.

2. Materials and methods

All stated salts and sugars for the different buffers were purchased from reliable manufactures (Sigma-Aldrich, Munich, Germany; Merck KGaA, Darmstadt, Germany). For buffer and solution preparation ultrapure, demineralized water from SG Ultra Clear UV Plus Pure Water System (VWR, Darmstadt, Germany) was used, which was additionally sterilized by a Systec V-40 steam autoclave or sterile filtration (0.22 µm pore size; Sarstedt, Nümbrecht, Germany).

2.1. Software

Table 1 Software

Software	Company
Winstat standard statistical software (Microsoft Excel Add-In) 2012.0.96	R.Fitch Software, Statcon GmbH, Witzenhausen, Germany
ImageJ (Fiji) 2.0.0	National Institutes of Health, Bethesda, USA
GraphPad Prism 8.2.1	GraphPad Software Inc., La Jolla, USA
GuavaSoft 3.1.1	Luminex Munich GmbH, Munich, Germany
Image Lab 4.0.1	Bio-Rad, Munich, Germany
Seahorse Wave 2.6.1	Agilent Technologies, Waldbronn, Germany
LAS X 3.4.2.	Leica, Wetzlar, Germany
Prime View 5.0 / Prime View evaluation 5.0	GE Healthcare, Freiburg, Germany
Optima Software 2.20	BMG Labtech, Offenbach, Germany
RTCA Software 1.2	Roche Diagnostics, Penzberg, Germany

2.2. Cell Culture

Materials for cell culture that were not sterilized by the manufacturer were autoclaved in advance to usage (Systec V-40 s).

Table 2 Cell culture material

Material	Company
Pipette tips	Gilson, USA Greiner, Germany
Eppendorf tubes	Sarstedt, Germany
0.22 µm Whatman Puradisc™ sterile filter	Whatman, Germany
1, 5, 10 mL syringes	Braun, Germany
15 and 50 mL tubes	Greiner, Germany
Whatman puradisc™	Sarstedt, Germany
Cell scraper	Sarstedt, Germany
T75 flasks	Greiner, Germany
T175 flasks	Greiner, Germany
6-well plates	Greiner, Germany
µ slide 8 well	Ibidi GmbH, Germany
24-well plates	Greiner, Germany
96-well plates	Greiner, Germany
White walled 96-well plates	Greiner, Germany
96-well plates (for BCA measurements)	Roche, Applied Science, Germany
96-well E-plate	Omni Life Science GmbH, USA
XF96-well microplates and cartridges	Agilent Technologies, USA

If not stated differently, the experiments conducted in this thesis were performed in the neuronal HT22 cell line. HT22 cells were generated upon immortalization of the primary mouse hippocampal HT4 cell line using a temperature-sensitive SV-40 T antigen and following subselection upon glutamate sensitivity^{150,151}.

HT22 cells as well as the mouse hypothalamus mHypo-CLU190 cell line (Cedarlane®, Cellutions Biosystems Inc., Burlington, Canada) were cultured at 5 % CO₂/ 37 °C (HERAcell®, Haereus/ThermoFisher, Darmstadt, Germany) in Dulbecco's Modified Eagle's Medium (DMEM) (Sigma-Aldrich, Munich, Germany) which was additionally enriched with 10 % heat-inactivated fetal calf serum, 100 U/mL penicillin, 100 mg/mL streptomycin and 2 mM glutamine (Merck KGaA, Darmstadt, Germany). All cell lines were regularly checked for mycoplasma contamination (every 3-4 months) and split twice in a week (1:10 – 1:20).

2.2.1. Standard solutions for cell culture

Table 3 Standard cell culture medium

Ingredients	Quantity
DMEM medium (+ 4.5 mg/L glucose/ 110 mg/L Na-pyruvate)	440 mL
Heat-inactivated fetal calf serum (FCS)	50 mL
L-Alanyl-L-glutamine 200mM	5 mL
Penicillin 10,000 U/mL, Streptomycin 10,000 µg/mL	5 mL

Table 4 1 × Phosphate buffered saline solution

Ingredients	Quantity
NaCl	9 g
Na ₂ HPO ₄	0.527 g
KH ₂ PO ₄	0.144 g
HCl (0.1 M)	pH 7.4
Bidest. H ₂ O	Ad 1 L

Table 5 Trypsin solution (0.05 %)

Ingredients	Quantity
Trypsin 7.500 U/ mg	100 mg
EDTA	40 mg
1x PBS	Ad 200 mL

2.2.2. Splitting of the cells

The described procedure was applied for all cell lines in use.

DMEM growth medium of the cells was removed by vacuum. Following, a washing step was performed with 10 mL of phosphate buffered saline (PBS) (Table 4) to remove remnant medium that could interfere with trypsinization. Thereafter, 2 mL of trypsin solution (Table 5) was applied for detachment of the cells on the bottom of the flasks. After several minutes, complete detachment was checked under the microscope and subsequently stopped with 5-fold amount of DMEM medium. Following, cell suspension was transferred to a 15 mL tube and centrifuged (5 min 1,000 RPM). The supernatant was removed again, and the resulting cell pellet was resuspended in fresh DMEM culture medium. For quantification, 5 μ L of cell suspension was transferred in a Neubauer counting chamber (Neubauer Zählkammer, Brand, Wertheim, Germany) and counted under the microscope. Afterwards, the needed number of cells were seeded in the plates depending on treatment time point, cell's sensitivity to treatment, plate size and type of experiment (Table 6).

Table 6 Number of cells seeded for respective well formats

	Cells/ plate
96-well plates	6,000 – 8,000
XF96-well microplates	8,000 – 10,000
96-well E-plate	6,000 – 9,000
24-well plates	40,000 – 60,000
6-well plates	200,000 – 300,000
8-well ibidi plates	15,000 – 20,000

2.3. Cell death induction

2.3.1. Induction of cell death by compounds

Cell death induction was conducted 24 – 36 h after initial cell seeding. Before treatments, cells were checked for proper cell morphology and density. Experiments were only performed, when the cells showed a healthy spindle-shaped structure, and the cell density was 60 – 90 %. The following table shows the cell death inducers used with the main cell death pathways each elicits (Table 7). All compound stock solutions were stored at -20°C and diluted to the respective in-use concentration subsequently before treatment with DMEM medium.

Table 7 Cell death inducers

Compound	Company	Cell death pathway	Stock solution
Erastin	Merck KGaA, Darmstadt, Germany	Ferroptosis	1 mM in DMSO
1S, 3R RSL-3 (RSL-3)	Synthesized by AK Diederich, (Department of Pharmaceutical Chemistry, University of Marburg) ^{34,35}	Ferroptosis	1 mM in DMSO
Staurosporine	Sigma Aldrich, Taufkirchen, Germany	Apoptosis	2 mM in DMSO
H ₂ O ₂	Sigma Aldrich, Taufkirchen, Germany	Unspecific generation of oxidative stress	1 M in DMEM

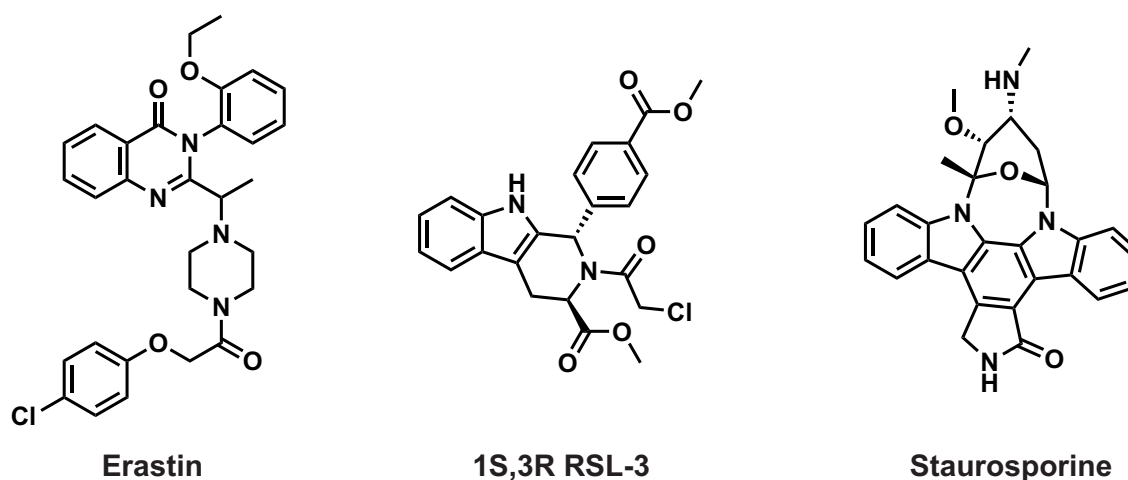


Figure 10. Structure of the used cell death inducers.

2.3.2. t-BID induced cell death

t-BID induced cell death was evoked by pIRES-tBID vector (Landshamer et al., 2008) transfection. To control for unspecific toxicity that resulted due to transfection, PcDNA3.1+ vector (Invitrogen, Karlsruhe, Germany) was used as a negative control.

Vector transfection was performed according to the manufacture's protocol. In short, Lipofectamine 2000 (Invitrogen, Karlsruhe, Germany) (1 μ L/ well) was diluted in OptiMEM I reduced serum medium (OptiMEM) (Invitrogen, Karlsruhe, Germany) and incubated for 5 min. In the meantime, the different plasmids (0.5 μ g) were diluted in OptiMEM. Thereafter, plasmid solution and Lipofectamine 2000 solution were combined and incubated for another 20 min at room temperature (RT). After incubation, the transfection solution was applied drop-wise to the cells previously seeded in 24-well plates and incubated overnight.

2.4. Inhibition of cell death

The BID inhibitor BI-6c9 was either purchased (Sigma-Aldrich, Taufkirchen, Germany) or synthesized by the group of Prof. Dr. Schlitzer (Schl-30300) (Department of Pharmaceutical Chemistry, University of Marburg). BI-6c9 was dissolved in DMSO to a stock concentration of 10 mM and stored at -20 °C.

Synthesis of the novel DPA compounds that were studied in this thesis was performed by Dr. Anna Lena Pfaff (AK Prof. Dr. Schlitzer, Department of Pharmaceutical Chemistry, University of Marburg). A detailed description of the synthesis is provided in the doctoral thesis of Dr. Pfaff¹⁴⁷. DPA 1-3 were diluted to a 100 mM stock in DMSO. On this basis, further stock solutions of 10 mM in DMSO and 1 mM in DMEM were produced. All solutions were stored at -20 °C.

The treatment of cell death inhibitors was performed, if not stated differently, simultaneously to respective cell death induction (co-treatment). Although, for some experiments cell death inhibitors were treated either before (pre-treatment) or 2-10 h after initial cell death induction (post-treatment).

2.5. Assessment of cell viability

2.5.1. Microscopic images

For representative bright field images of cell morphology, cells were seeded in 8-well ibidi plates and treated with erastin or RSL-3 +/- compounds for the respective treatment period. Afterwards, bright field images were captured using a Leica DMI6000 epifluorescence microscope (Leica, Wetzlar, Germany). After that, microphotographs were further edited in Fiji software and adjusted for color and brightness. When images are additionally enlarged using digital zoom, this is mentioned in the figure legend.

2.5.2. MTT assay and EC-50 determination

Only living cells with active metabolism can reduce the yellow MTT (3-(4,5-dimethylthiazol-2-yl)-2,5-diphenyltetrazolium bromide) to the purple formazan mainly in mitochondrial dependent pathways ¹⁵². Thus, the intensity of purple staining is a direct indicator for metabolic activity and cell viability.

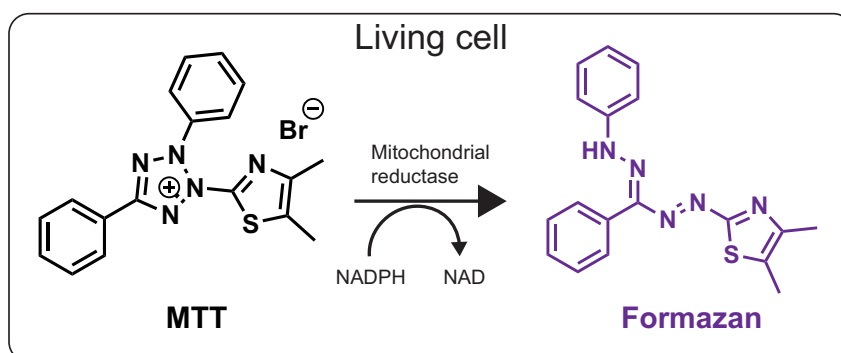


Figure 11. MTT assay.

These experiments were performed in 96-well plates. After 24 - 36 h of cell incubation in standard growth medium, the medium was exchanged for the respective treatment solution and incubated for the respective times. For MTT assay, 20 μ L of a MTT stock solution (2.5 mg/ mL in PBS) was added and incubated for 1 h at 37°C. Afterwards, the supernatant was removed, and the plates were frozen for at least 1 h at -80 °C. The resulting purple-colored formazan was dissolved in 70-80 μ L DMSO and incubated on a shaker for one more hour at 37°C

before absorbance (570 nm/ 630 nm) was measured with FluoStar OPTIMA photometer (BMG Labtech, Offenbach, Germany). The results were normalized to untreated control as 100% to ensure comparability between different experiments.

On the basis of 3 - 5 independent MTT experiments for each individual concentration, EC50 values were calculated exploiting the GraphPad Prism Software 8.2.1 (non-linear fit: log (inhibitor) vs. response, variable slope) in accordance to earlier EC50 calculations (Jelinek et al., 2018).

$$Y = Bottom + \frac{X^{Hillslope} * (Top - Bottom)}{X^{Hillslope} + EC50^{Hillslope}}$$

Top/ Bottom: Top and bottom plateaus of the curve; HillSlope: Steepness of the curve

2.5.3. XCELLigence measurements

Real-time cell viability measurements were conducted utilizing the xCELLigence Real-Time Cell Analyzer RTCA-MP (Roche Diagnostics, Mannheim, Germany) as described previously¹⁵³. Briefly, the cells were seeded on plates with implanted gold microelectrodes that measured changes in impedance. Cell growth caused an increase in impedance which was reflected by an increase in cell index (CI). Cell shrinkage or detachment of the cells from the bottom of the plate for instance due to cell death stimuli resulted in a decrease in cell index.

After blank measurement of the DMEM medium was performed, HT-22 cells were seeded in the 96-well E-plates and incubated for up to 24 h until the average cell index reached approximately a value of 1.0. Thereafter, cells were treated as indicated at the distinct experiments and impedance was measured over at least 24 h. To correct for differences in cell growth at the beginning of the experiments, the start value directly before applying the treatment solutions were set to 1.0. After the experiments, E-plates were washed several times with sterile bidest. H₂O before trypsin was applied for 30 min to several hours at 37°C. After removing the trypsin solution, the E-plate was washed again at least three time with sterile bidest. H₂O. The complete removal of all cells was checked under the microscope. When there were still attached cells visible, the procedure was repeated. If not, plates were again sterilized using UV light under the benches for 30 min.

2.6. Flow cytometry measurements

Lipid peroxidation (BODIPY) (Invitrogen, Karlsruhe, Germany), cellular ROS formation (2',7'-dichlorodihydrofluorescein diacetate (DCF) (Invitrogen, Karlsruhe, Germany), mitochondrial ROS formation (MitoSOX) (Invitrogen, Karlsruhe, Germany), mitochondrial membrane potential (TMRE) (MitoPT™, Immunochemistry Technologies, Germany and cell death) and Annexin V FITC/propidium iodide (Annexin V/PI) (Invitrogen, Karlsruhe, Germany) were measured utilizing the fluorescence-activated cell sorting (FACS) system. For endpoint measurements, ~40,000 HT22 cells were seeded in 24-well plates. On the following day, cells were treated with the indicated treatment solutions and incubated for another 15 - 24 h. For experiments measured until 10 h of total treatment time, ~60,000 HT22 cells were seeded in 24-well plates 24 h in advance of the respective treatment. After treatments, cells were stained and measured with the FACS Analyzer Guava Easy Cyte 6-2 L system (Luminex Munich GmbH, Munich, Germany). The assays are described in further detail in the respective sections. For data analysis GuavaSoft Software package was used. For every FACS experiment at least three wells per condition were measured analyzing 5,000 cells per well.

2.6.1. DCF assay

For DCF assay the chlormethyl-H₂DCF diacetate dye (CM-H₂DCFDA) was used. As shown in the figure below (Figure 12 A), the diacetate derivative penetrates the cell membranes due to its nonpolar nature. Once in the cell, the diacetyl structure is cleaved by intracellular esterases to hydroxyl groups so that the now polar molecule is trapped inside the cell. Now, the H₂DCF is prone to oxidation by ROS that results in an increase in green emission at 517 - 527 nm.

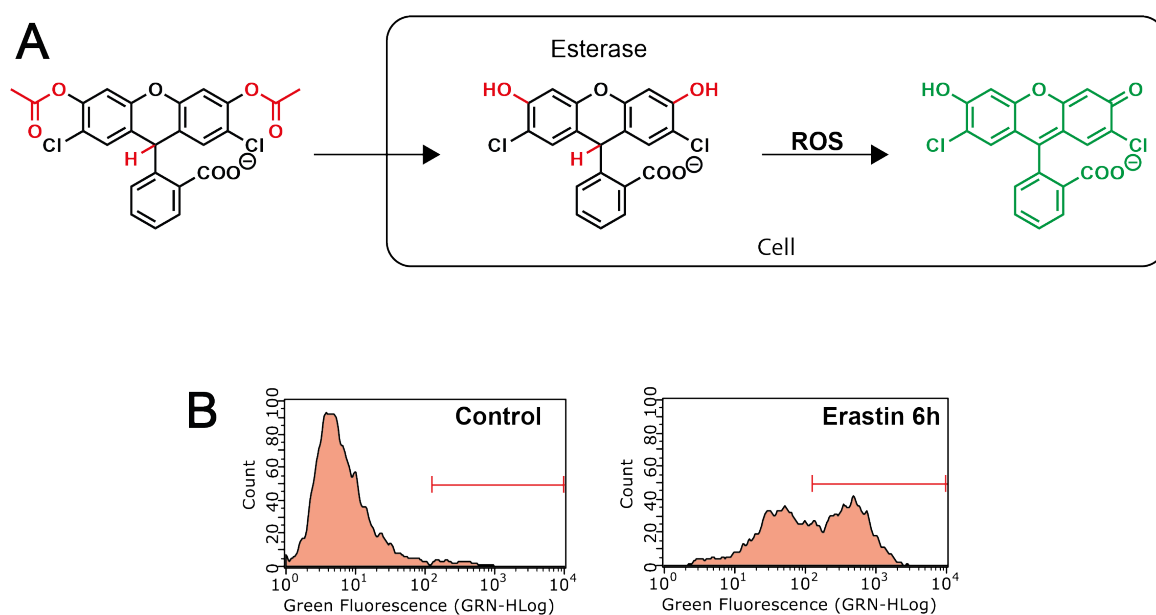


Figure 12. DCF assay. **A)** Scheme of DCF fluorescence signal formation. **B)** Development of green fluorescence signal after 6 h of erastin treatment. Red bar shows representative gating for quantification.

For the experiments, at the indicated time points after treatments, treatment solutions were exchanged by serum-free medium containing DCF dye to a final concentration of 2.5 μ M for 30 min at 37 °C. Afterwards, cells were incubated with DMEM medium containing serum for additional 30 min at 37 °C, harvested, washed once with PBS and re-suspended in 150 μ L PBS. Fluorescence was excited at 488 nm wavelength and emission was recorded at 525/ 30 nm. For data analysis, the increase in fluorescence was determined as representatively demonstrated (Figure 12 B).

2.6.2. BODIPY assay

BODIPY-C11 (Figure 13 A) is used to analyze lipid peroxidation in cells and membranes and is therefore frequently used in ferroptosis research. Upon oxidation of the polyunsaturated butadienyl portion the fluorescence emission peak shifts from the red spectrum (~590 nm) to the green spectrum (~510 nm).

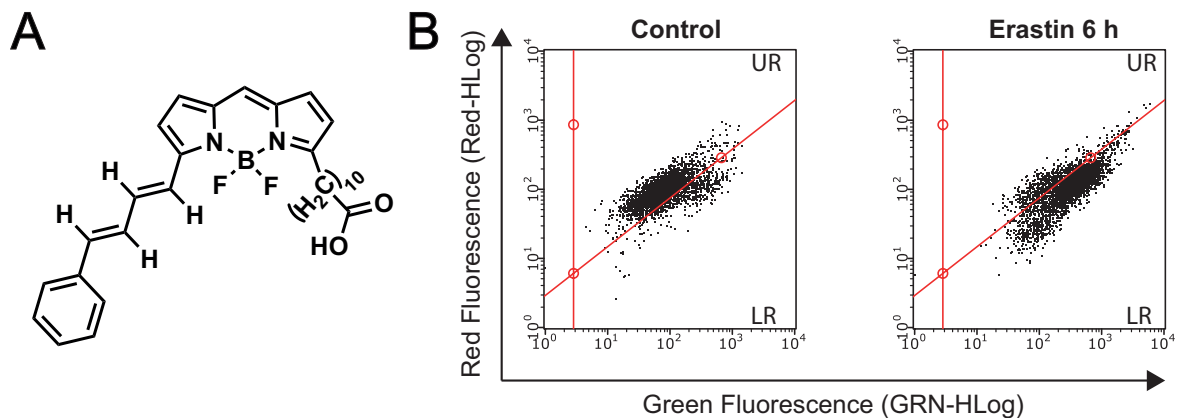


Figure 13. BODIPY assay. **A)** Structure of BODIPY-C11. **B)** Representative plots showing the BODIPY signal switch from the upper right (UR) corner to the lower right (LR) corner after 6 h of erastin treatment. For quantification, percentage of the cells in the LR corner was determined.

In this thesis, cells were stained after the treatments with BODIPY for 0.5 - 1 h at 37 °C in DMEM medium at a final concentration of 2 μ M. Afterwards, the staining solution was removed, cells were harvested, washed, and resuspended in 150 μ L PBS. The BODIPY signal, representing lipid peroxidation, was analyzed at 488 nm excitation and 525/ 30 nm emission wavelengths as indicated in the representative plots (Figure 13 B).

2.6.3. MitoSOX assay

MitoSOX is a mitochondrial targeted dye for superoxide detection. To assure selective allocation of the dye to the mitochondria the dye consists of a positively charged tetraphenylphosphonium moiety. Upon oxidation of MitoSOX an increase in red fluorescence (~ 580 nm) is detected (Figure 14 A).

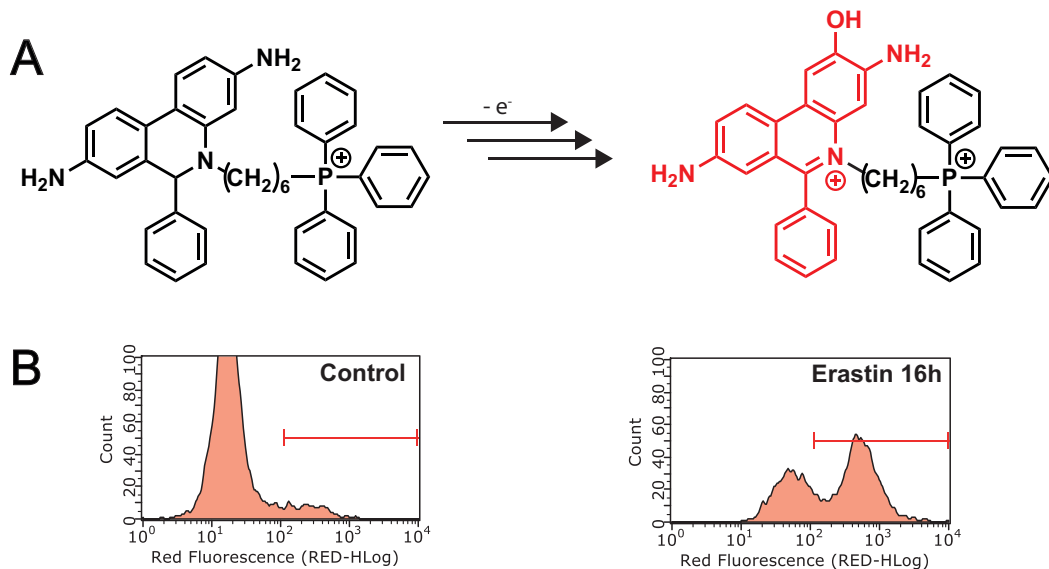


Figure 14. MitoSOX assay. **A)** Fluorescence activation by mitochondrial ROS (modified from ¹⁵⁴). **B)** Representative gating of the red MitoSOX fluorescence after medium (control) treatment and after 16 h of erastin treatment.

In the used protocol, cells were incubated with MitoSOX red ($1.25 \mu\text{M}$) for 30 min at 37°C after respective treatments. Next, the staining medium was removed from the cells, harvested, washed once and resuspended in $150 \mu\text{L}$ PBS and subjected to immediate FACS analysis (excitation: 488 nm, emission: $690/50$ nm) (Figure 14 B).

2.6.4. TMRE assay

For determination of the mitochondrial membrane potential the lipophilic fluorescent dye TMRE (tetramethyl rhodamine ethyl ester) was used. Due to its positive charge, TMRE accumulates at the negatively charged mitochondria. When the charge is vanished due to break down of the mitochondrial membrane potential, TMRE dye is diluted in the cytosol resulting in a decrease of the red fluorescence signal (Figure 15 A).

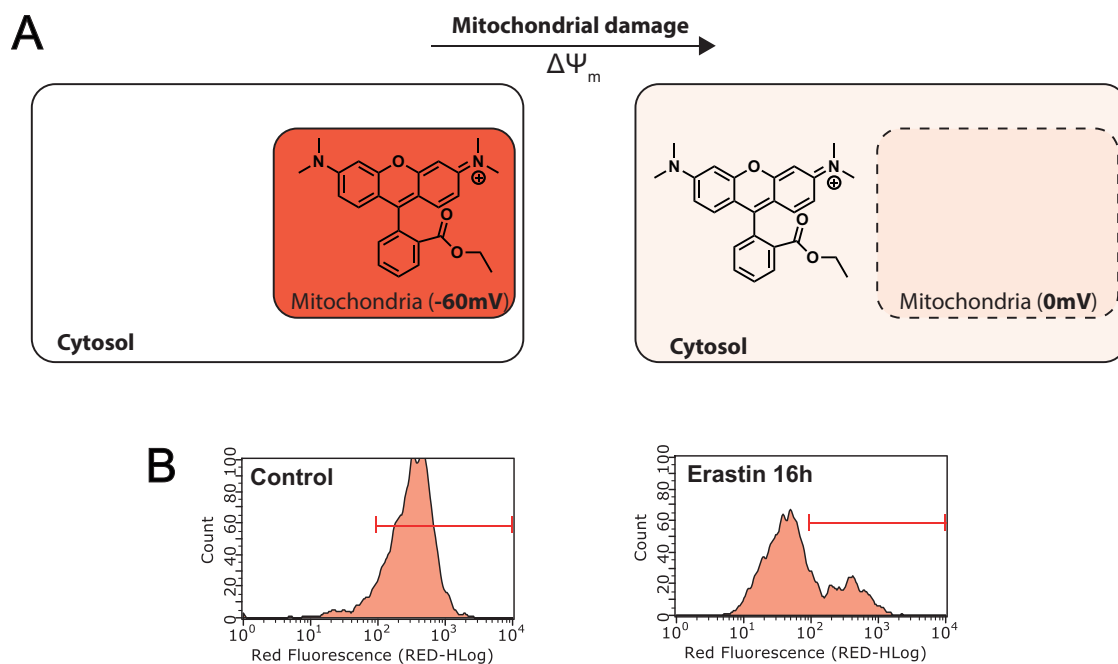


Figure 15. TMRE assay. A) Scheme of TMRE enrichment in mitochondria when mitochondrial membrane potential is intact (60mV) and after loss of mitochondrial membrane potential (0mV). **B)** Representative gating of TMRE staining at control conditions and after 16 h of erastin treatment.

To the certain time points, 1 μL TMRE dye (0.4 μM in the well) was added to the cells and incubated for 30 min at 37 $^{\circ}\text{C}$. After harvesting, and washing the cells once with PBS, HT22 cells were resuspended in 150 μL PBS. FACS measurements were exerted with a excitation wave length of 488 nm and emission was detected using a 690/ 50 nm filter (Figure 15 B).

2.6.5. Annexin V FITC/ PI assay

Annexin V FITC in combination with PI (propidium iodide) is used for staining early and late apoptotic cells. In early stages of cell death, phosphatidylserine (PS), which is normally located on the inner cytoplasmic surface of the cell membrane (Figure 16 A Healthy cell) is translocated to the outer plasma membrane, which than could be bound via the 35-36 kDa fluorescein labeled Annexin V protein in the presence of calcium ions (Figure 16 A Early cell death). PI on the other hand can only penetrate the cell and bind to the DNA when the membranes are already strongly disrupted making it a staining for late necrotic cell death (~650 nm) (Figure 16 A Late cell death).

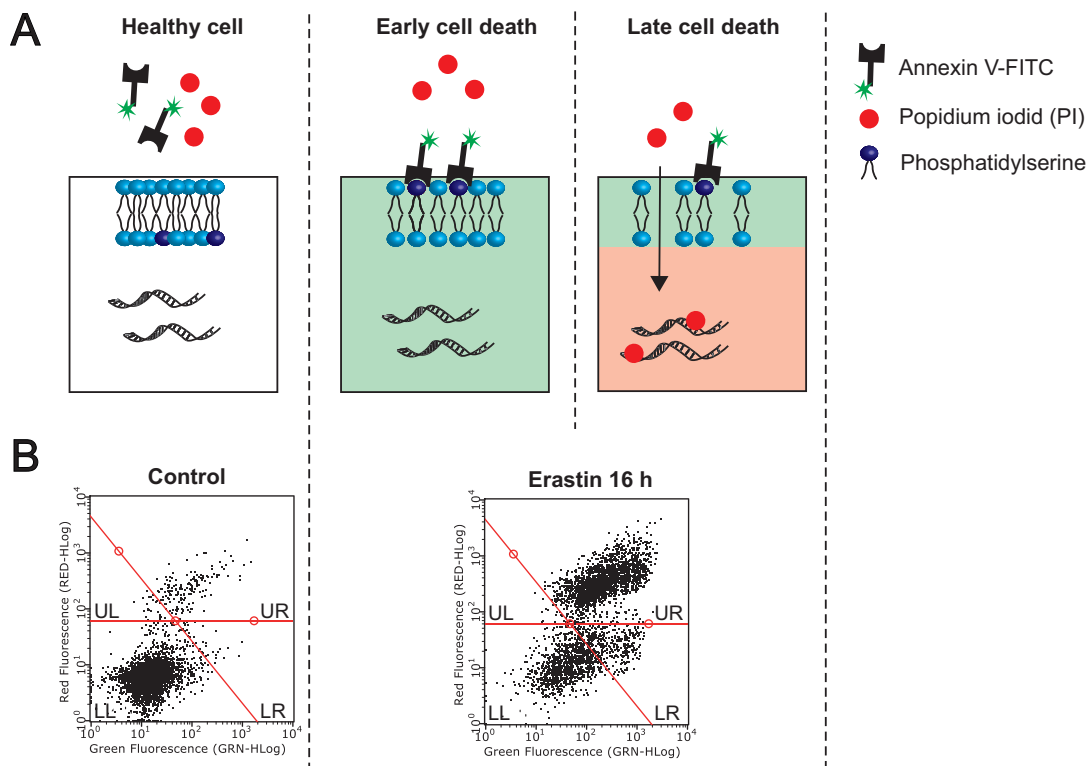


Figure 16. Annexin V/ PI assay. A) Mechanism of Annexin V and PI binding in the progression of cell death. **B)** Representative gating of Annexin/ PI cell death measurements. For quantification of total cell death, cell count from upper right (UR; Annexin V+ PI positive cells) and lower right (LR; Annexin V positive cells) segments were summed up.

In this study, cells were washed once with PBS, trypsinized, centrifuged and resuspended in 150 μ L Annexin V/ PI binding buffer containing 0.2-0.5 μ L Annexin V and PI solution for every well and incubated for another 10 min at RT in the dark. The staining was detected via flow cytometry (excitation: 488 nm, emission: red filter: 690/ 50 nm, green filter: 525/ 30 nm) (Figure 16 B).

2.7. DPPH assay

Radical scavenging activity of the compounds was measured using DPPH assay (2,2-diphenyl-1-picrylhydrazyl) (Cayman Chemical Company, Ann Arbor, USA). DPA compounds and Trolox were prepared in 75 % ethanol in respective concentrations. Afterwards, 90 μL DPPH solution (150 μM) and 10 μL sample solution were incubated in 96-well plates in the dark for 30 min and absorbance was assessed at 517 nm using a plate reader (SPARK 20M, TECAN, Germany). Respective DPPH scavenging effect was calculated in accordance to the formula:

$$\frac{(A_0 - A_x)}{A_0} * 100$$

A_0 reflects the intrinsic absorbance of ethanol and A_x reflects the absorbance of the individual samples.

2.8. Glutathione assay

Glutathione levels were measured in a colorimetric reaction of DTNB (5,5'-dithio-bis(2-nitrobenzoic acid), Ellman's reagent) with the reactive thiol group of glutathione (GSH). Thereby, glutathione reductase is able to recycle the GSH and the reaction can continue several times. The yellow colored TNB (405 – 414 nm) is directly proportional to the concentration of GSH in the samples (Figure 17).

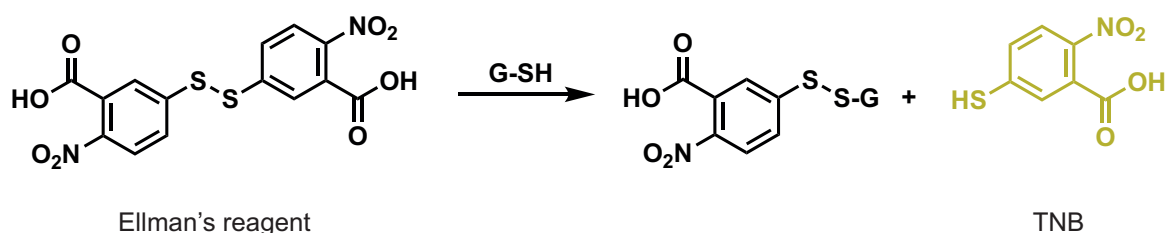


Figure 17. Glutathione assay.

To determine glutathione levels in our experimental settings, 200,000 – 300,000 HT22 cells were seeded in 6-well plates 24 h before treatment. For each condition, three wells were treated similarly. At indicated time points, the cells were harvested in DMEM by scratching, and similarly treated conditions were pooled. Thereafter, cells were centrifuged (1,000 RPM, 5 min), washed once with PBS and centrifuged again. The PBS was removed, cell pellets were immediately frozen in N₂ (l) and stored at -80 °C until all samples were collected. Thereafter, glutathione assay was performed in accordance with the manufacturer's protocol (Cayman Chemical Company, Ann Arbor, USA). Briefly, cell pellets were resuspended in MES-buffer (0.4 M 2-(N-morpholino) ethanesulphonic acid, 0.1 M phosphate, 2 mM EDTA, pH 6.0) and sonicated (Branson Sonifier Cell Disrupter S-450D, Branson Ultrasonics, Dietzenbach, Germany) for several seconds. Cell debris was removed by centrifugation at 10,000 × g for 15 min. Next, metaphosphoric acid (1.25 M) was applied to the supernatants for protein precipitation. After incubation for 5 min, the samples were centrifuged at 17,000 × g for 10 min. Thereafter, the pH of the supernatants was increased using 4 M triethanolamine solution, before the samples were transferred into a 96-well plate. Subsequently, the freshly prepared assay cocktail (containing Ellman's reagent) was added to the supernatants in the 96-well plate and incubated in the dark for 10 min. Absorbance was measured at 405 nm in a Tecan spark photometer (SPARK 20M photometer, TECAN, Germany). GSH amounts were normalized to the respective protein contents. Data is compared to control, which was set to 100 %.

2.9. Analysis of protein levels

For the determination of protein level, 2 – 3 wells of a 6-well plate per condition were treated similarly. After indicated treatment times, treatment media were removed, and cells were washed once with PBS. Afterwards, cells were harvested with a cell scraper in 70 – 100 μ L western blot lysis buffer for each condition. The cell suspensions were collected in an Eppendorf tube and directly frozen in N₂ (l). Thereafter, samples were either stored at -80°C or directly thawed up on ice for further use. The thawed samples were centrifuged (10,000 RPM, 10 min, 4°C) to separate the cell debris from the protein solution. The supernatants were transferred to a fresh Eppendorf tube before protein content was determined using BCA assay and prepared for western blot analysis. Remaining protein solution was stored at -80 °C.

Table 8 Western blot lysis buffer

Mannitol	0.25 M
Tris	0.05 M
EDTA	1 M
EGTA	1 M
PhosSTOP	1 tablet
Complete Mini Protease Inhibitor Cocktail	1 tablet
Bidest. H ₂ O	Ad 10 mL
<hr/>	
DTT 100 mM (right before use)	1:100
Triton-X-100 (right before use)	1:100
<hr/>	

2.9.1. BCA assay

For determination of the protein content, the bicinchoninic acid (BCA) assay (Pierce BCA Protein Assay Kit, Thermo Fisher Scientific, Darmstadt, Germany) was performed. In this assay, the proteins reduce Cu^{2+} to Cu^+ in alkaline medium (biuret reaction), which is then chelated by two BCA molecules. This results in the formation of a purple-colored complex (562 nm).

For analysis, 2.5 μL of the samples or protein standards (Bovine serum albumin standard containing 0-190 μg) were mixed with 100 μL BCA solution (reagent A: reagent B 1:50). Following, all samples were incubated for 30 minutes (60 °C, shaking). Thereafter, samples were shortly centrifuged and transferred to a 96-well plate for absorbance measurements in the FluoStar Optima plate reader (595 nm). Protein content of the respective samples were analyzed with regard to the BSA standard curve using the Wizard function of the BMG Labtech Data Analysis Software.

2.9.2. Polyacrylamid gel electrophoresis (PAGE)

Table 9 5x SDS sample buffer

1.5 M Tris-HCl pH 6.8	1.81 mL
Glycerol	5 mL
SDS	1 g
β -Mercaptoethanol	2.5 mL
1 % Bromophenol blue	0.5 mL
Bidest. H_2O	Ad 10 mL

Table 10 Ammonium persulfate (APS)

APS	1 g
Bidest. H_2O	10 mL

Table 11 Sodium dodecyl sulfate (SDS) 10%

SDS	10 g
Bidest. H_2O	100 mL

Materials and methods

Table 12 Stacking gel 3.5%

Bidest. H ₂ O	6.2 mL
0.5 M Tris-HCl buffer pH 6.8	2.5 mL
Sodium dodecyl sulfate solution 10 %	0.1 mL
Acrylamide/bisacrylamide (37.5:1) 30 %	1.2 mL
Ammonium persulfate solution (APS) 10 %	0.05 mL
Tetramethylethylenediamine (TEMED)	0.02 mL
Phenol red (optional)	q.s.
Total	10 mL

Table 13 Running gel 10% / 12.5%

	10 %	12.5 %
Bidest. H ₂ O	4 mL	3.35 mL
1.5M Tris pH 8.8	2.5 mL	2.5 mL
SDS 10 %	0.1 mL	0.1 mL
Acryl/bis (30 %)	3.34 mL	4 mL
10 % APS	0.05 mL	0.05 mL
TEMED	0.01 mL	0.01 mL
Total	10 mL	10 mL

Table 14 SDS-Page buffer 10x

Tris base	30 g
SDS	10 g
Glycine	144 g
Bidest. H ₂ O	ad 1 L

10x SDS buffer is diluted with bidest H₂O (1:10) ultimately before use

To separate the proteins by size, polyacrylamide gel electrophoresis was performed. Therefore, 5x SDS (Sodium dodecyl sulfate) sample buffer was added to the respective amount of protein (~50 – 70 µg, maximal 60 µL) in the ratio 1:5 and heated (95 °C, 2 – 5 min, 500 – 600 RPM) before being loaded to the gels together with the PageRuler™ Prestained Ladder (ThermoFisher Scientific, Schwerte, Germany) as a molecular weight marker. Gels were prepared beforehand and were composed of 3.5 % stacking gel and 10 – 12.5 % running gel. First, electrophoresis was performed at 60 V until the samples were concentrating at the separation gel. Then, proteins were separated at 100 – 120 V.

2.9.3. Western blot

Table 15 10x Western blot transfer buffer

Tris base	30 g
Glycine	144 g
HCl	pH 8.3
Bidest. H ₂ O	ad 1 L
10x western blot transfer buffer is diluted with bidest. H₂O 1:10 and 20 % EtOH	

Table 16 10x TBS

NaCl	292 g
Tris base	24.2 g
HCl	pH 7.5
Bidest. H ₂ O	1 L

Table 17 1x TBST

TBS 10x	100 mL
Tween 20	0.5 mL
Bidest. H ₂ O	ad 1 L

Table 18 Blocking milk 5 %

Skim milk powder	5 g
Bidest. H ₂ O	ad 100 mL

Western blot was performed in order to transfer the separated proteins obtained in the SDS-PAGE to a polyvinylidene fluoride (PVDF) membrane (Roche Diagnostics, Germany). On these membranes the different proteins could be analyzed in regard to their expression patterns using specific antibodies for the individual proteins.

The transfer was conducted in MiniTrans-Blot Cell tank (Bio-Rad, Munich, Germany) at 350 mA for 1.5 h. After protein transfer, the membrane was washed once with 1x TBS before equilibration of the membrane was performed for 1 h in 5 % blocking buffer, following primary antibody (AB) incubation over night at 4°C. On the following day, the primary AB was additionally incubated for 1 h at RT, before being washed three times with TBST and incubated with the corresponding HRP-labelled secondary antibodies for 1-2 h. Thereafter, the membrane was washed again (TBST, 3x 10 minute), before being developed using HRP-Juice (PJK GmbH, Kleinblittersdorf, Germany). Western blot bands were detected via the Chemidoc system (ChemiDoc XRS system, Bio-Rad Laboratories, USA). Quantification was performed using the Image Lab Software (Bio-Rad, Munich, Germany). Background-corrected intensities of the western blot bands were determined, followed by intrinsic normalization to the respective loading control. To assure comparability between different experiments, band intensities were compared to their respective control set as 100 %.

Table 19 Antibodies

Primary Antibody	Dilution in milk	Host	Company
GPX-4	1:500	Rabbit	Abcam
Vinculin	1:20,000	Mouse	Sigma Aldrich

Secondary Antibody	Dilution in milk	Host	Company
Peroxidase-labeled anti-mouse IgG (H+L)	1:3000	Horse	Vector laboratories
Peroxidase-labeled anti-rabbit IgG (H+L)	1:3000	Goat	Vector laboratories

2.10. Mitochondrial analysis

2.10.1. Mitochondrial morphology and categorization

In order to analyze mitochondrial morphology, HT22 cells were seeded in 8-well ibidi dishes. Twenty-four hours later, cells were incubated for another 10 h with 0.4 μ M erastin and with or without compound co-treatment, before they were stained with MitoTracker™ DeepRed (0.2 μ M, 633 nm) and DAPI (1 μ g/ mL, 360 nm) for 30 min at 37 °C and subsequently fixed for 20 min with PFA 4 % (paraformaldehyde) solution and washed with PBS before mitochondrial analysis was conducted.

Mitochondrial appearance was classified as previously described in three different categories¹³⁸. Category I: mitochondria were elongated and equally distributed in the cell. Category II: mitochondria appeared largely dotted (not coherent) but were still widely distributed in the whole cell. Category III: mitochondria were completely fragmented and located around the nucleus. At least 500 cells per condition were analyzed based on this classification system and calculated as percentage of all cells for each category. For quantification, the results of three independent experiments were taken into consideration. Representative images were acquired via 63 x oil objective of the Leica DMI6000 epifluorescence microscope. Microphotograph magnifications were performed using digital zoom.

2.10.2. Seahorse measurements

Mito stress test

The Seahorse system XF96-Analyzer (Agilent Technologies, Waldbronn, Germany) was utilized to investigate alterations in energy metabolism of the cell via analysis of the oxygen consumption rate (OCR), as an indicator of mitochondrial energy metabolism and extracellular acidification rate (ECAR), as an indicator for energy supply via glycolysis (Figure 18).

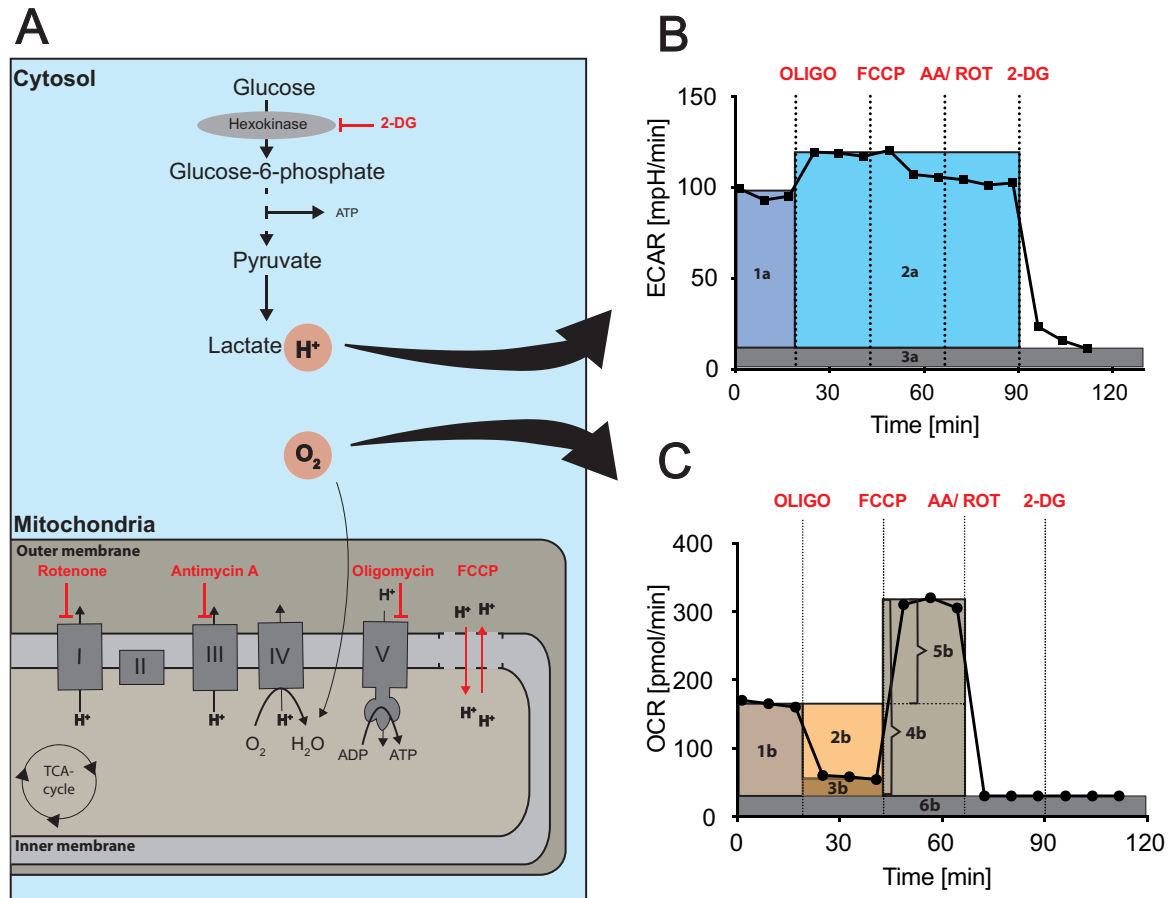


Figure 18. Seahorse measurement. A) Energy supply via glycolysis and mitochondrial respiration. Red marked are the compounds used in the mito stress test. **B)** Representative ECAR graph: 1a: glycolysis, 2a: glycolytic capacity; 3a: non-glycolytic acidification **C)** Representative OCR graph: 1b: basal respiration; 2b: ATP production; 3b: Proton leak; 4b: maximal respiration; 5b: spare capacity; 6b non-mitochondrial respiration

For these measurements, 7,000 cells were seeded in XF96-well microplates. Different treatments were performed 36 h later. After ferroptosis initiation and compound co-treatments overnight (16 h), treatment solutions were replaced by Seahorse assay medium (4.5 g/l glucose, 2 mM glutamine, 1 mM pyruvate, pH 7.35) and incubated at 37 °C for 60 min without CO₂. In the meantime, the injection

solutions were prepared as follows: injection A (OLIGO): oligomycin (3 μM); injection B (FCCP): FCCP (0.5 μM); injection C (AA/ ROT): antimycin A (0.1 μM)/ rotenone (1 μM); injection D (2-DG): 2-desoxyglucose (50 mM). Three measurements were conducted before the first injection, representing the commencement of OCR followed by three measurements after each injection. Immediately after each injection, a three-minute mixing step was performed to ensure proper compound distribution in the well before measurements started for additional three minutes. For evaluation, the respiration rates were normalized to respective cell density, determined as protein content of each well. Therefore, cells were washed once with PBS after the measurement, before 50 μL lysis buffer (10 mM Tris base, 0.1% (v/v) Triton X-100) were added. Thereafter, plates were frozen for at least 1 h at -80°C , before BCA assay was performed as described in 2.9.1.

Basal respiration was determined by subtracting the OCR generated by non-mitochondrial respiration (after AA/ROT application) from the commencement of OCR (before oligomycin injection). Maximal respiration was determined by subtracting the OCR, generated by non-mitochondrial respiration (after AA/ROT application), from the maximal OCR (after FCCP injection). To ensure comparability between the single experiments when three independent experiments were pooled, untreated controls of basal respiration and maximal respiration were set to 1 for each experiment. All other values were calculated according to the respective untreated controls.

2.10.3. ATP measurement

To assess ATP levels, measurements were performed in accordance with the ViaLight™plus Bioassay Kit protocol (Lonza, Verviers, Belgium). Briefly, 8,000 cells were plated in a 96-well cell culture plate. After the indicated treatments, cells were lysed with the respective lysis buffer. Afterwards, cell lysates were transferred to a white-walled luminescence plate (Greiner, Frickenhausen, Germany), AMR plus reagent was added and incubated for 2 min in the dark. Then, ATP is converted to AMP by luciferin under stoichiometric bioluminescence emission, which was measured via FluoStar OPTIMA photometer.

2.11. Isolation of mitochondria from rat brains

Table 20 1x Isolation buffer

	Final concentration	
Sucrose	300 mM	103 g
TES	5 mM	1.15 g
EGTA	200 μ M	0.076 g
Bidest H ₂ O		ad 1 L
Adjust pH with 1 M KOH		pH 7.2

Table 21 1x MSHE-BSA buffer (mitochondrial isolation buffer)

	Final concentration	
Sucrose	70 mM	24 g
Mannitol	210 mM	38.3 g
HEPES	5 mM	1.19 g
EGTA	1 mM -	0.38 g
Bidest H ₂ O		Ad 500 mL
Adjust pH with 1 M KOH		pH 7.2
BSA (added ultimately before use)	0.5 % (w/v)	5 g

Sprague Dawley rats were kindly provided by the AG Prof. Dr. Wöhr (Department of Psychology, University of Marburg). The experiments were performed with male and female animals at ages between 6–8-month. All steps of the brain extraction and mitochondrial isolation were performed on ice.

On experiment days, rats were anesthetized using isoflurane. After absence of the foot withdrawal response, the animals were killed by decapitation followed by brain dissection. ~50 mg of the prefrontal cortex were extracted and subsequently transferred to 1 mL of isolation buffer.

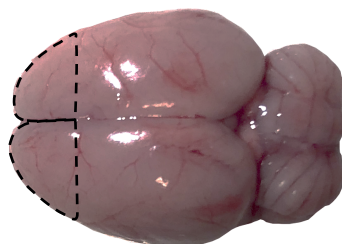


Figure 19. Isolated brain of a Sprague Dawley rat. After brain dissection, the olfactory bulbs were removed and the prefrontal cortex (dotted area) was extracted for the experiments.

Mitochondrial isolation was performed similarly to an already established protocol¹⁵⁵.

Briefly, the tissue of the prefrontal cortex was homogenized by trituration of the tissue using a 20 G Neoject needle (Dispomed, Gelnhausen, Germany) and a 1 mL syringe 10-15 times. Finally, the roughly homogenized solution was strained through a 100 µm cell strainer (Corning Incorporated, Corning, NY, USA) to remove remaining large pieces. The suspension was filled in a 1 mL gas-tight syringe (Sulpeco, Germany) that were subsequently attached to the pump cell homogenizer (Isobiotec, Heidelberg, Germany). The pump system was previously equilibrated using isolation buffer. The isolation of mitochondria was conducted by three successive pumping steps (0.7 mL/ min, 10 µm clearance (diameter tungsten carbide ball)). Following, a centrifugation step (800 x g, 10 min, 4°C) was conducted separating the cell debris from the supernatant containing the mitochondria. The supernatant was transferred to a new 1.5 mL tube and centrifuged again (9000 x g, 10 min, 4 °C) to obtain a pellet of crude mitochondria (Heraeus™ Fresco™ 17 Mikrozentrifuge; Thermo Fisher Scientific, Darmstadt, Germany). The supernatant was discarded, and the mitochondria palette was resuspended in 500 µL MSHE-BSA buffer. Protein content was determined by BCA assay as described in 2.9.1..

2.11.1. Seahorse measurements in isolated mitochondria

Coupling assay

The coupling assay for determination of the respiration states in isolated mitochondria was performed as recommended in the manufactures protocol. This setup allows for evaluation of the coupling between the electron transport chain (ETC), and the oxidative phosphorylation machinery and thus can provide critical information upon mitochondrial constitution when, for example, being exposed to different compounds ¹⁵⁶.

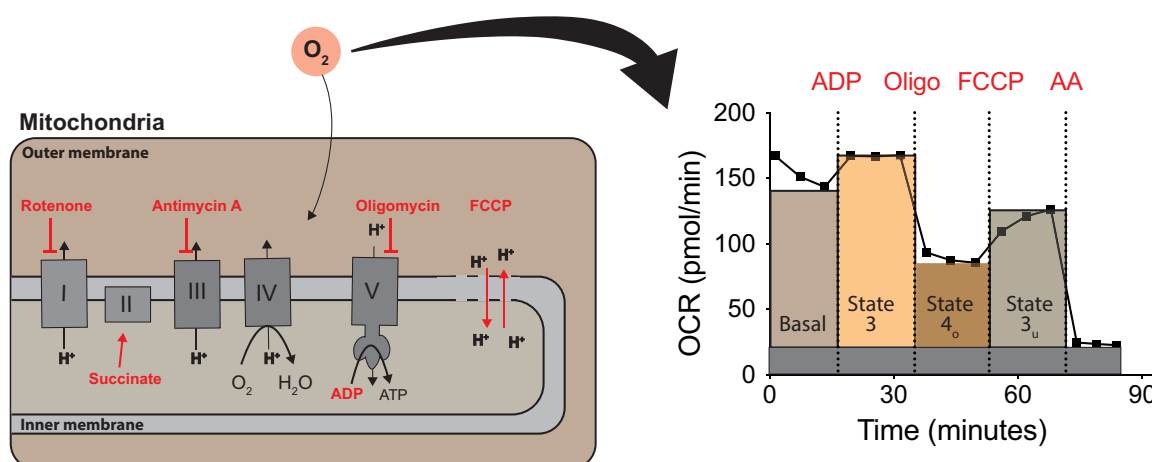


Figure 20. Coupling assay in isolated mitochondria. Red marked are the compounds used in the coupling assay. Complex II substrate succinate and the complex I inhibitor rotenone were directly added to the MAS buffer. A representative Seahorse measurement is shown on the right. The calculations of the respective states are described in Table 23.

Table 22 MAS buffer

	Concentration	1L
Sucrose	70mM	24g
Mannitol	220mM	40,08g
KH ₂ PO ₄	10mM	1,36g
MgCl ₂	5mM	0,476g
HEPES	2mM	0,476g
EGTA	1 mM	0.38 g
Bidest. H ₂ O		1 L
Adjust pH with 5 M KOH		7.2
BSA (added ultimately before use)	0.2 % (w/v)	2 g

Injection solutions were prepared with MAS buffer without sucrose and mannitol

Briefly, isolated mitochondria from Sprague Dawley rats (2.11) were diluted to a final concentration that equals 8 µg per well in MAS buffer (supplied with complex II substrate succinate (10 mM) and the complex I inhibitor rotenone (2 µM)), before respective treatments were conducted as follows: To 8 µg mitochondria per well the respective volumes of PBS or Bid3CCSS in PBS were added on ice. The final volume was adjusted to 25 µL/ with MAS buffer (+ succinate/ rotenone) before the solutions were incubated in the water bath (37 °C) for 15 min. Thereafter, the volume corresponding to 8 µg mitochondrial protein were transferred in each well of the Seahorse cell culture plate and centrifuged in a plate centrifuge (Heraeus Megafuge 40R; Thermo Fisher Scientific, Darmstadt, Germany) (2000 x g, 20 min, RT). Thereafter, 155 µL pre-warmed MAS buffer (+ succinate/ rotenone) were added to adjust the volume to a total of 180 µL/ well, before the Seahorse measurements were started. Injection solutions were prepared in MAS buffer without sucrose and mannitol (Final concentrations: 4 mM ADP, 2.5 µg/ml oligomycin, 4 µM FCCP and 4 µM antimycin A)

To normalize for variation in the starting OCR, the basal respiration of the PBS controls was set to 100% for each experiment. Therefore, the change of the OCR due to the application of the respective modulators of the electron transport chain were always regarded with respect to the respective basal respiration.

Table 23 Calculation of the respiratory states in this thesis

Basal respiration (%)	$\frac{\text{min (before ADP injection)} - \text{min (after Anitmycin A (AA)injection)}}{\text{min (before ADP injection) - min (after AA injection)}} * 100$
State 3 (%)	$\frac{\text{max (after ADP injection)} - \text{min (after AA injection)}}{\text{min (before ADP injection) - min (after AA injection)}} * 100$
State 4 _o (%)	$\frac{\text{min (after oligomycin injection)} - \text{min (after (AA)injection)}}{\text{min (before ADP injection) - min (after AA) injection)}} * 100$
State 3 _u (%)	$\frac{\text{min (after FCCP injection)} - \text{min (after Anitmycin A (AA)injection)}}{\text{min (before ADP injection) - min (after AA injection)}} * 100$
RCR	$\frac{\text{State 3 (\%)}}{\text{State 4o (\%)}} * 100$

2.12. *In silico* ADME and toxicity analysis

In silico ADME and toxicity studies were performed using the freely available PreADMET online tool ¹⁵⁷ and admetSAR online server ¹⁵⁸.

2.13. Protein Purification

2.13.1. Bid3CCSS-GST construct

For crystallization, the Bid3CCSS-Glutathione-S-transferase (GST) construct was used. This construct was previously cloned and transformed in *Escherichia coli* Rosetta2 (DE3) cells. A glycerol stock was prepared and stored at -80 °C. Rosetta2 (DE3) cells possess a chromosomal copy of the T7 RNA polymerase gene regulated by the lacUV5 promoter where protein expression could be induced via Isopropyl β -D-1thiogalactopyranoside (IPTG) treatment. Therefore, Bid3CCSS-GST was cloned in an expression vector containing a T7 promoter that enables strong protein expression upon IPTG treatment.

Table 24 Bid3CCSS construct

Box-Nr.	Plasmid	Bacteria	Resistance	Date generated	Gene origin
3-32	pGEX delta13-Y47 Bid3 CCSS-GST	Rosetta2(De3)	Amp./ Chloramp.	20.03.15	mouse

2.13.2. Buffers and solutions for protein purification

All buffers and solutions were sterile-filtered and if necessary degassed for several hours before usage.

Table 25 LB medium

Tryptone	10 g
Yeast extract	5 g
NaCl	5 g
Bidest. H ₂ O	1 L

Materials and methods

Table 26 GSH binding buffer for GSH HiCap column 20 mL

Tris base	20 mM	2.42 g
NaCl	100 mM	5.84 g
EDTA	1 mM	0.29 g
DTT	1 mM	1 mL (1 M stock)
Bidest. H ₂ O		ad 1 L
HCl		pH 7.6
0.03 % Na-azide (After pH adjustment)		1 mL (30% aqueous solution)

Table 27 GSH elution buffer for GSH HiCap column 20 mL

Tris base	50 mM	6.06 g
Reduced L-glutathione	10 mM	3.07 g
EDTA	1 mM	0.29 g
DTT	1 mM	1 mL (1 M stock)
Bidest. H ₂ O		ad 1 L
HCl		pH 8.0
0.03 % Na-azide (After pH adjustment)		1 mL (30% aqueous solution)

Table 28 Gel filtration buffer for HiLoad 16/600 Superdex 75 pg gel filtration column 120 mL

Tris base	20 mM	2.42 g
NaCl	50 mM	2.92 g
(TCEP)		1 g (optional)
Bidest. H ₂ O		ad 1 L
HCl		pH 7.4
0.03 % Na-azide (After pH adjustment)		1 mL (30% aqueous solution)

2.13.3. Bid3CCSS expression

For expression of the Bid3CCSS-GST construct, a pipette-tip (~1 μ L) of frozen Rosetta2 containing the Bid3CCSS-GST vector was pipetted in 200 mL LB medium (+ 1:1000 ampicillin/ chloramphenicol) and incubated at 37 °C overnight. On the next day, 10 mL of the e-coli culture solution were added to 4 x 300 mL fresh LB medium and incubated at 37 °C for several hours. Cell density was checked every 30 min using the Bio-Rad SmartSpec TM Plus spectrophotometer (AG Bünemann, Bio-Rad, Munich, Germany). When OD₆₀₀ reached ~ 0.6, 1 mM IPTG (Stock: 1 M in H₂O) was added to the cells to start protein expression. Protein expression was then performed for 5-6 h before cells were harvested. From now on, all steps were carried out on ice. Bacteria culture was transferred to 250 mL centrifuge tubes, carefully tared and centrifuged (Beckman JC-MC, Beckman Coulter, Krefeld, Germany) (15 min, 5,000 RPM, JA-10 rotor). Thereafter, LB medium was discarded, and bacterial pellets were pooled and resuspended in 20 mL GSH binding buffer containing two Complete Mini Protease Inhibitor Cocktail tablets. This bacterial suspension was then stored at -80°C until purification.

2.13.4. Protein purification

Protein purification was performed using the small-scale liquid chromatography system ÄKTA prime plus (GE Healthcare, Freiburg, Germany). The runs were monitored via a UV/Vis and conductivity measurements and pH analysis using the PrimeView software. After the respective runs the data was analyzed and exported using Prime View evaluation program.

Before starting the protein purification, the ÄKTA system was cleaned with sterile-filtrated, degassed bidest. H₂O two times using the preinstalled “system wash” program. Thereafter, the respective column was installed and purged with sterile-filtrated, degassed bidest. H₂O with at least three-times the volume of the column capacity to remove the EtOH 20% at manual run (0.5-1 mL /min depending on the maximal pressure limit for the individual column). Thereafter, the column was equilibrated with two volumes of the respective buffer. After finishing the purifications, the columns were washed with two volumes of sterile-water and two volumes of degassed EtOH 20% to avoid contamination while column storage.

For application of the sample solution, a 5 mL sample loop was used. When protein was applied, the valve had to be adjusted to the “load” position. For application of the protein solution to the column the valve had to be switched to the “inject” position. The exact procedure for sample application is described in the manufacture’s manual (p. 47-48).

2.13.5. Cell lysis

To extract the desired protein, the previously prepared bacterial suspension (2.13.3) was thawed on ice before the cells were subsequently lysed using the Branson Sonifier system with the macro tip (10:00 min, Amplitude: 20%, Pulse on: 1.0, Pulse off: 1.0). To remove the cell debris, cell suspension was centrifuged (20-30 min, 35,000 RPM, 4°C) in an ultracentrifuge (Beckman Optima XE-90, Ti70.1 rotor, Beckman Coulter, Krefeld, Germany). The supernatant was then sterile filtered using a 0.22 µm filter and a 50 mL syringe.

2.13.6. Glutathione affinity chromatography

To separate the desired protein from the remaining proteins of e-coli, glutathione affinity chromatography was performed using the GSH HiCap column 20 mL (max. pressure limit: 0.5 MPa) (Qiagen, Düsseldorf, Germany). The Bid3CCSS construct was tagged with the 25 kDa Glutathione-S-transferase (GST) protein. During purification the GST protein binds to the immobilized glutathione in the column with high affinity. Hence, when a mixture of several proteins was applied to the column, only the GST-tagged protein could sufficiently sequester the glutathione molecules in the column and therefore restrained the tagged protein from subsequent elution. Elution of the sequestered protein was performed using GSH elution buffer containing glutathione. The purified fractions were detected using the UV/ Vis spectra and gel electrophoresis and subsequent Coomassie staining. The purified fractions were pooled together for further usage.

Table 29 Method 30 GSH affinity chromatography

	Breaking point	Volume [mL]	Concentration Buffer B [%]	Flow rate [mL/ min]	Fractions [mL]	Valve position
Equilibration	1	0.0	0	0.8	0	Load
	2	10.0	0	0.8	0	Load
	3	12.0	0	0.8	5.0	Inj
	4	17.0	0	0.8	2.0	Load
	5	19.0	0	0.8	5.0	Inj
	6	24.0	0	0.8	2.0	Load
Sample Loading/	7	26.0	0	0.8	5.0	Inj
	8	31.0	0	0.8	2.0	Load
Sample Binding	9	33.0	0	0.8	5.0	Inj
	10	38.0	0	0.8	2.0	Load
	11	40.0	0	0.8	5.0	Inj
	12	45.0	0	0.8	2.0	Load
	13	47.0	0	0.8	5.0	Inj
	14	52.0	0	0.8	5.0	Load
	15	132.0	0	0.8	2.0	Load
Protein Elution	16	134.0	100.0	0.8	2.0	Load
	17	174.0	100.0	0.8	2.0	Load
Equilibration	18	180.0	0	0.8	2.0	Load
	19	210.0	0	0.8	2.0	Load

GSH affinity chromatography was conducted either using the respective method 30 or in a similar way using manual run. Buffer A: GSH binding buffer; buffer B: elution buffer.

2.13.7. Coomassie staining

In order to determine the purified fractions of the proteins, first SDS-PAGE was performed as described earlier (2.9.2), with 20 μ L of each fraction. Thereafter, the gel was transferred and incubated in Coomassie Blue R-250 staining solution (Table 30) (ThermoFisher Scientific, Schwerte, Germany) at 37°C for 1 h. The blue Coomassie staining unspecifically stains proteins on basic amino acids. Afterwards, gels were incubated in a destaining solution (Table 31) overnight (RT, shaking), to remove the excessive dye. Images were acquired using the Chemidoc-XRS System using the “white transillumination” mode.

Table 30 Coomassie Blue R-250 staining solution

Coomassie Blue R	1 g
Methanol	450 mL
Acetic acid (100 %)	100 mL
Bidest. H ₂ O	ad 1 L

Table 31 Coomassie destaining solution

Methanol	450 mL
Acetic acid (100 %)	100 mL
Bidest. H ₂ O	ad 1 L

2.13.8. Thrombin cleavage

To remove the GST-Tag from the desired protein, Bid3CCSS-GST was cleaved by thrombin. In advance, GSH-elution buffer had to be exchanged to gel filtration buffer (Table 28), since EDTA as well as DTT could disturb thrombin activity. Therefore, the pooled fractions obtained in the GSH affinity chromatography were transferred to a 3 kDa Amicon® Ultra Centrifugal Filter Units (15 mL) and centrifuged (4,000 RPM, 10-20 min). Between every centrifugation step, flow-through was discarded and gel filtration buffer was added to the protein solution and thoroughly mixed. This procedure was repeated until approximately three times of the previous GSH elution buffer volume was added to the protein solution as gel filtration buffer.

12 mM CaCl₂ was added to the protein solution to enhance cutting efficiency of thrombin and ~20 U of thrombin (Novagen/Merck, Darmstadt, Germany) were applied and incubated at 37°C for 16-18 h. Thrombin cleavage was stopped on the next day using 1 mM phenylmethylsulfonyl fluoride solution (PMSF). The removal of the well-soluble GST-tag often resulted in a significant Bid3CCSS protein precipitation. The precipitated protein was removed by centrifugation (4,500 RPM, 10 min) and sterile filtration using a 0.45 µm filter. 5 mL of the resulting sample solution was then subjected to size exclusion chromatography.

2.13.9. Size exclusion chromatography (SEC)

To separate the Bid3CCSS protein from uncleaved educt and the removed GST-tag, size exclusion chromatography was performed using the ÄKTA prime plus system. Analogously, as described before, 4-5 mL protein solution was applied to the system via the 5 mL sample loop. Purification was performed using the HiLoad TM 16/600 Superdex 75 pg gel filtration column 120 mL (max. pressure limit: 0.3 MPa) (GE Healthcare, Freiburg, Germany). In the column, dextran is covalently bound to highly cross-linked agarose, to form a distinct polymer structure that enables bigger proteins to cross the column in a shorter time than smaller proteins that could interfere with the polymers. The 75 pg Superdex column is designed to separate proteins between 3,000-70,000 kDa. Eluted fractions were collected in 2 mL steps and stored at 4°C after the purification was finished.

Table 32: Method 14 Size exclusion chromatography

	Breaking point	Volume [mL]	Concentration Buffer B [%]	Flow rate [mL/ min]	Fraction size [mL]	Valve position
Sample Loading	1	0.0	0	0.8	0	Load
	2	10.0	0	0.8	0	Inject
Sample fractionation	3	16.0	0	0.8	5.0	Load
	4	20.0	0	0.8	2.0	Load
	5	45.0	0	0.8	5.0	Load
Wash-out	6	160.0	0	0.8	2.0	Load

Size exclusion chromatography was performed either using the method 14 or in a similar way using manual run.

After SEC different samples were analyzed using SDS-PAGE/ Coomassie staining (2.13.7). Highly pure sample fractions were pooled together and concentrated in 5 mL Amicon filters (Millipore, Schwalbach, Germany) (3 kDa cut-off, 4000 rpm, 4 °C).

Thereby, protein concentration was continuously monitored using the Implen NanoPhotometer (NanoDrop) (Implen, Munich, Germany). This determination is based on aromatic amino acids such as tyrosine, tryptophan and phenylalanine in the protein which have a specific absorption maximum at 280 nm. Hence, the absorption of an individual protein is represented by the protein-specific extinction

coefficient, which depends on the number of the aromatic amino acids in the respective protein sequence. The Bid3CCSS protein was measured using 4 μL sample volume (Bid3CCSS: M: 17.536 g/ mol, extinction coefficient (ϵ)=2980 $\text{M}^{-1} / \text{cm}^{-1}$ (<https://web.expasy.org/protparam/>), Lid factor 10). The final protein solution was always adjusted to 10-15 mg/mL. Finally, the solution was thoroughly sterile-filtered through a 0.22 μm Restek Syringe Luer-Lock filter (Wicom Germany GmbH, Germany) and stored at 4 °C before crystallization.

2.13.10. Mass spectrometry

To confirm the identity and purity of the purified Bid3CCSS protein, the purified protein solution was analyzed using mass determination of intact proteins at the service department of the chemical department (FB15) using ESI-MS techniques. That allows for very accurate determination of the protein mass to detect possible impurities or structure defects of the Bid3CCSS molecule.

2.13.11. Buffer exchange

For treatment of Bid3CCSS in isolated mitochondria, gel filtration buffer was exchanged to PBS using the PD Mini Trap G-25 kit (GE Healthcare, Freiburg, Germany), as described in detail in the manufacture's manual on page 6.

2.14. Protein crystallization

A basic requirement for crystal structure determination of a protein is to produce a highly pure protein with a high conformational homogeneity (2.13). This highly pure protein solution is then transferred to an environment, where the protein solution is in a hypotonic state in comparison to a reservoir solution (vapor diffusion). This drives water molecules to diffuse towards the concentration gradient into the hypertonic reservoir solution to equilibrate the system, thereby leading to a successive increase in the concentration of the protein solution. At some point, formation of crystals from the components in the meta stable solution is entropically favorable, to release water molecules previously located at their surfaces (nucleation). During this process the proteins form a well-ordered three-dimensional lattice, with a repeating structure (unit cell). This lattice is held together by weak interactions and is often disrupted or includes less ordered regions (mosaicity). Due to the highly periodical arrangement of the molecules the electrons are located in a specific position. When X-rays hit these electrons, they are not diffracted at random, but in a very specific way, resulting in a very specific diffraction pattern for each single protein. From these data combined with the respective phases the structure can be determined.

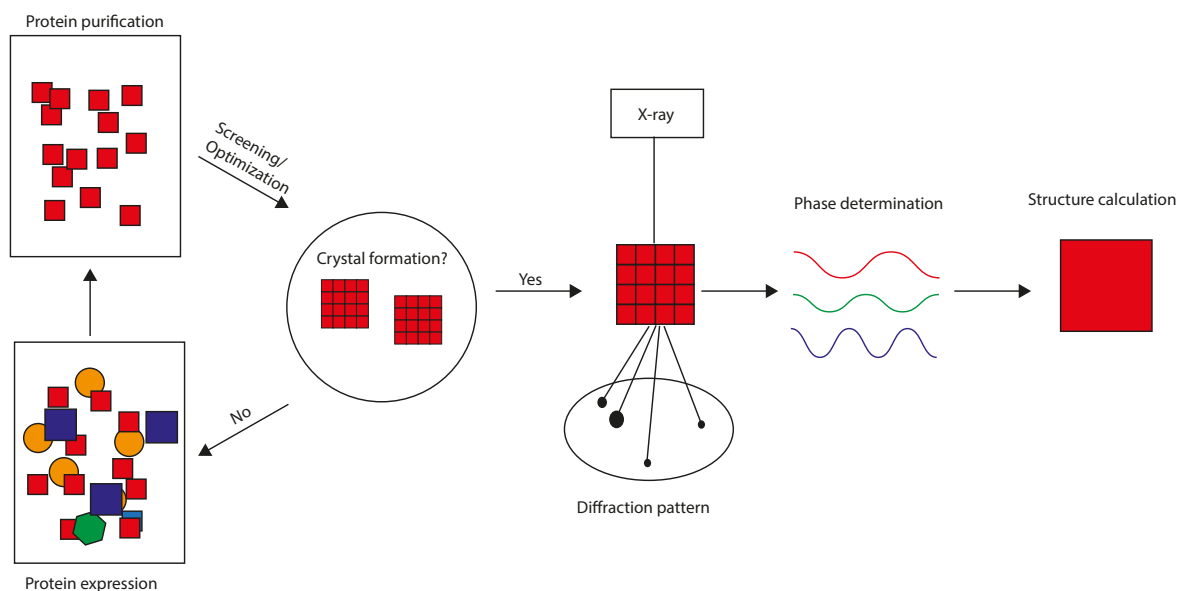


Figure 21 General workflow of the crystallization process.

Protein crystallization was done in collaboration with CrystalsFirst GmbH, a spin-out from the group of Prof. Dr. Klebe (Department of Pharmaceutical Chemistry, University of Marburg), who are highly experienced in operating with hard to crystallize proteins.

All reagents used for the crystallization solutions were purchased from Fluka/Sigma-Aldrich (Sigma-Aldrich, Taufkirchen, Germany) or Roth (Karlsruhe, Germany).

2.14.1. Crystallization technique

Vapor crystallization technique was applied for all experiments using a sitting drop protocol at 18 °C on 24-well Cryschem-Plates from Hampton Research (Aliso Viejo, CA, USA). Reservoir solutions were prepared in advance and thoroughly mixed. Thereafter, experiments were performed at least in triplicates using 500 µL of reservoir solution. The crystallization drops in each well consisted of 1 µL protein solution and 1 µL reservoir solution which were dispensed without homogenization. The plates were sealed using Shark tape (Hampton research, Aliso Viejo, CA, USA). Crystals were usually fully grown after 2-5 days at 18°C. To distinguish between protein crystals and salt crystals, polarizing microscopy was used.

2.14.2. Seeding

To increase the number of well-formed crystals with a suitable size, a seeding protocol was applied. Seeding allows crystallization to occur at designated template crystals and thus bypasses the statistical event of forming a suitable nucleus for a well-formed crystal¹⁵⁹. For this purpose, crystals that were already well-grown were crushed in the crystallization drop using a pipette tip (or crystal tool) to obtain small seed crystals. A thoroughly washed horsehair was drawn through the prepared microcrystalline seed solution once or twice. The hair was then successively passed through the 24-wells containing the crystallization buffer without washing the hair or extracting new crystals from the microcrystalline stock solution.

2.14.3. Harvesting and measurements of the crystals

Prior to the X-ray measurements, crystals were flash-frozen in liquid nitrogen to protect them from damage due to X-ray radiation. To minimize crystal deterioration during the flash-freezing process, the crystals were harvested directly from the crystallization drop using cryo-loops (Hampton Research, Aliso Viejo, CA, USA) and transferred into a new solution containing 25 % PEG 400 as cryoprotectant. Afterwards, they were harvested with a cryo-loop, flash frozen with liquid nitrogen and stored under liquid nitrogen. Initial diffraction tests were measured in-house at a MAR345 at 100 K at the department of pharmaceutical chemistry. Promising crystals were then measured at DESY, ESRF or BESSY at 100 K.

2.14.4. Crystal data analysis and structural refinement

Structural determination and refinement were performed by CrystalsFirst with the kind support of Prof. Dr. Heine (Department of Pharmaceutical Chemistry, University of Marburg).

2.14.5. Heavy metal soaking

For heavy metal soaking, a crystal was harvested from the crystallization drop via a cryo-loop and transferred into a new 2 μ L drop consisting of 50 % reservoir solution, 50 % gel-filtration buffer supplemented with e.g. gadolinium-acetate (final concentration 10 mM). After 1 h the crystal was transferred into a 2 μ L drop of cryoprotectant-solution for 10 min and flash frozen afterwards.

2.14.6. Compound co-crystallization/ Soaking

For soaking, 1-2 crystals were transferred into a new 2 μ L drop of cryoprotectant supplemented with 1 mM of ligand. The crystals were incubated for 1 h or 24 h depending on crystal stability and directly harvested via cryo-loop and flash frozen afterwards.

For co-crystallization, 90 % protein-solution were incubated with 10% DMSO containing 10 mM of ligand (final concentration 1 mM) for 15 min. Then crystallization drops were set up analogously to the standard-protocol.

2.15. Microscale thermophoresis assay (MST)

Microscale thermophoresis assay is a powerful method to detect interaction of proteins with biomolecules or compounds ¹⁶⁰. During the measurement, a small region of a solution containing labeled protein is heated via an infra-red (IR) laser. The labeled molecules then diffuse alongside the generated temperature gradient (Figure 22). When the laser is turned off, diffusion of the labeled protein occurs in the opposite direction. The diffusion of the biomolecules is thereby studied which is dependent on size, charge and solvation. Ligand binding to proteins changes these parameters, hence leading to a changed diffusion behavior.

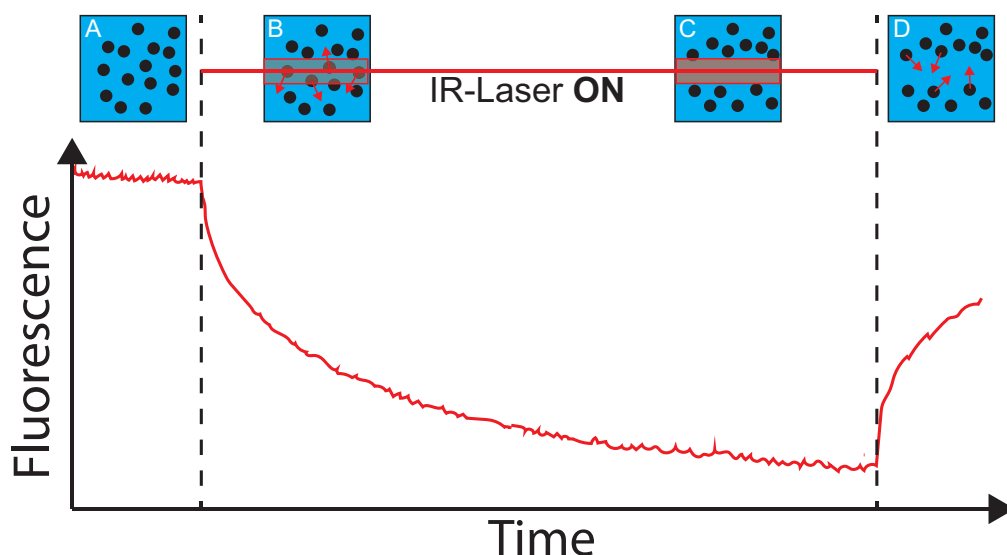


Figure 22. MST measurement curve. **A)** At the beginning of the experiment the IR laser is off, and the molecules are equally distributed in the solution. **B)** Turning on the IR-laser leads to a locally increased temperature. The molecules diffuse according to the temperature gradient, usually out of the heated area (thermophoresis), which cause a drop in fluorescence intensity. **C)** Equilibrium with no further changes in fluorescence intensity. **D)** IR-laser inactivation cause a back diffusion of the molecules to the protein deprived zone, resulting in a subsequent increase in fluorescence signal. The time frame for each measurement is normally between 20 – 30 seconds.

MST measurements were performed at the department of pharmaceutical chemistry.

The basic requirement for a protein to be measurable in the MST assay is that it can be labeled with a fluorescent dye. The Monolith Protein Labeling Kit Red-NHS 2nd generation Kit (NanoTemper Technologies, Munich, Germany) was used for this purpose. The labeling procedure was performed in compliance with the manufacturer's protocol.

Briefly, before starting the labeling procedure, 100 μ L of an approximately 10 μ M protein solution was prepared in gel filtration buffer.

Since Tris in the gel filtration buffer interferes with the labeling procedure, the buffer was replaced with labeling buffer NHS as recommended in the protocol.

For this purpose, the column material of the A-column was homogenized, before the storage solution was removed by centrifugation (1500 x g, 1 min). After that, column equilibration was conducted using the Labeling Buffer NHS provided in the kit. Afterwards, 100 μ L of the prepared protein solution was applied to the column and again centrifuged at 1500 x g for 2 min. The flow-through contained the protein in the Labeling Buffer NHS. Thereafter, protein concentration was measured using the NanoDrop 2000 Spectrophotometer (ThermoFisher Scientific, Schwerte, Germany).

Afterwards, protein labeling was performed. Initially, the labeling dye was reconstituted with 25 μ L of DMSO resulting in a 600 μ M dye solution. This solution was again diluted 1:1 with Labeling Buffer NHS to a final stock concentration of 300 μ M. The appropriate volume of labeling buffer (300 μ M) was then added to the protein, so that a 3-fold excess of dye was achieved. The protein-dye solution was incubated for 30 min in the dark at room temperature.

Meanwhile, the B-column was equilibrated using PBS, as assay buffer, as described in the protocol.

Following the 30 min incubation time, protein-dye solution was applied to the B-column. After the sample was completely rinsed through the column material, 550 mL PBS was applied, before protein was eluted with additional 450 μ L PBS. The flow-through was collected containing the labeled protein, which was now ready for MST measurements.

DMSO or a DMSO-stock of the ligand was then added to a sample of the labeled protein solution to a final volume of 10 μL .

The solutions were filled in a capillary (Monolith premium capillary) and placed in the Monolith NT.115 system (NanoTemper Technologies, Munich, Germany) as shown in Figure 23.

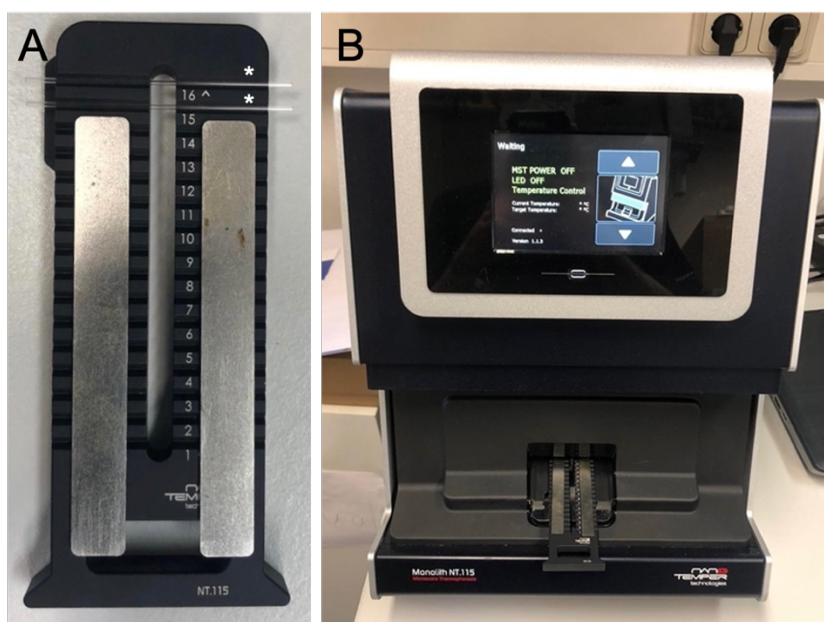


Figure 23. Monolith NT.115 system for MST measurement. A) Sample tray of Monolith NT.115 with inserted capillaries *. **B)** Monolith NT. 115 system with inserted sample trail.

2.16. NMR measurements

For sample preparation compounds were diluted in D₆-DMSO to a stock concentration of 2 mM before these stocks were further diluted to a final concentration of 100 μM (5% D₆-DMSO) in gel filtration buffer in presence or absence of Bid3CCSS (final concentration 5 μM). The solutions were then filled in 1.7 mm NMR tubes kindly provided by Dr. Christian Richter (AK Prof. Dr. Schwalbe, Institute for Biophysical Chemistry, Goethe University of Frankfurt). NMR measurements (600 MHz Spectrometer/ Sample head: 1.7 mm He cooled CryoProbe 1H {¹³C, ¹⁵N}) and data analysis was performed by Dr. Christian Richter.

2.17. Statistical analysis

The statistical analysis was mainly performed using Winstat standard statistical software (R. Fitch Software, Statcon GmbH, Witzenhausen, Germany). For multiple comparisons, analysis of variance (ANOVA) was conducted combined with Scheffé's post-hoc test. All data are presented as mean and standard deviation.

For statistical analysis of the respiratory states from the Seahorse measurements of isolated mitochondria Kruskal-Wallis statistics were performed as a nonparametric test followed by Dunn's multiple comparison test. The test was conducted using the prism software package. Results were considered as statistically significant if $p < 0.05$.

3. Results

3.1. BID crystallization

The pro-apoptotic protein BID is of major importance in cell death pathways that are involved in neurodegenerative diseases. However, only two NMR structures for the BID protein are available so far. The presence of a high-resolution BID crystal structure would be of great advantage for developing novel compounds by structure-based ligand design supported by *in silico* docking analysis. Successful and reproducible crystal formation for the Bid3CCSS construct was previously accomplished in the Morpheus A5 condition (Table 33), although the crystal quality was not sufficient for X-ray measurements and crystal structure determination. In this thesis, the Morpheus A5 condition was subjected to intensive optimization to enhance the crystal quality so that high-resolution X-ray data sets could be measured which are sufficient for BID structure determination.

3.1.1. Bid3CCSS purification

The Bid3CCSS-GST construct was previously transformed in Rosetta2 (DE3) *Escherichia coli* and frozen as a glycerol stock at -80°C. The glutathione-S-transferase (GST)-tag is used for protein purification in a glutathione affinity column and strongly enhances the water solubility of the Bid3CCSS protein. The protein construct was expressed for 5-6 h before bacteria were centrifuged and frozen in GSH binding buffer at -80°C for further use.

On the day of protein purification, the bacteria were lysed by sonification. Cell debris was removed by a centrifugation step followed by filtration through a 0.22 µm filter. Afterwards, Bid3CCSS-GST was subjected to GSH affinity chromatography using the ÄKTA prime plus system. Therefore, the obtained Bid3CCSS-GST solution was applied in several steps to the Glutathione HiCap Column. Bid3CCSS-GST sequestered the column-bound glutathione, whereas the bacterial proteins were directly eluted and thus were found in the first elution fractions (Figure 24 A 0-50 mL). After intense washing with approximately 100 mL of GSH binding buffer to remove weakly bound unspecific proteins, Bid3CCSS-GST was eluted from the column using GSH elution buffer. This resulted in an intense second peak that was visible in the UV/Vis spectrum after approximately

150 mL (Figure 24 A). In order to decide which protein fractions should be collected for further use, Coomassie staining was conducted. The total lysate fraction (TL) that was collected before the purification procedure showed a clear band at around 40 kDa representing the overexpressed Bid3CCSS-GST protein (~42 kDa), which was contaminated with bacterial proteins (Figure 24 B TL). As already observed in the chromatogram, these contaminations were not bound to the column and subsequently eluted (Figure 24 B F16). In contrast, Bid3CCSS protein bound to the column and was therefore barely present in the flow-through fractions. In the sample of the washing step no further protein was detected (Figure 24 B F30), while the fractions eluted with the GSH elution buffer were highly enriched in purified Bid3CCSS-GST protein (Figure 24 B F50-56). F51-54 were subsequently pooled, before GSH elution buffer was exchanged to gel filtration buffer. This step was required since DTT and EDTA could compromise the following thrombin cleavage, performed to remove the GST-tag from the Bid3CCSS protein.

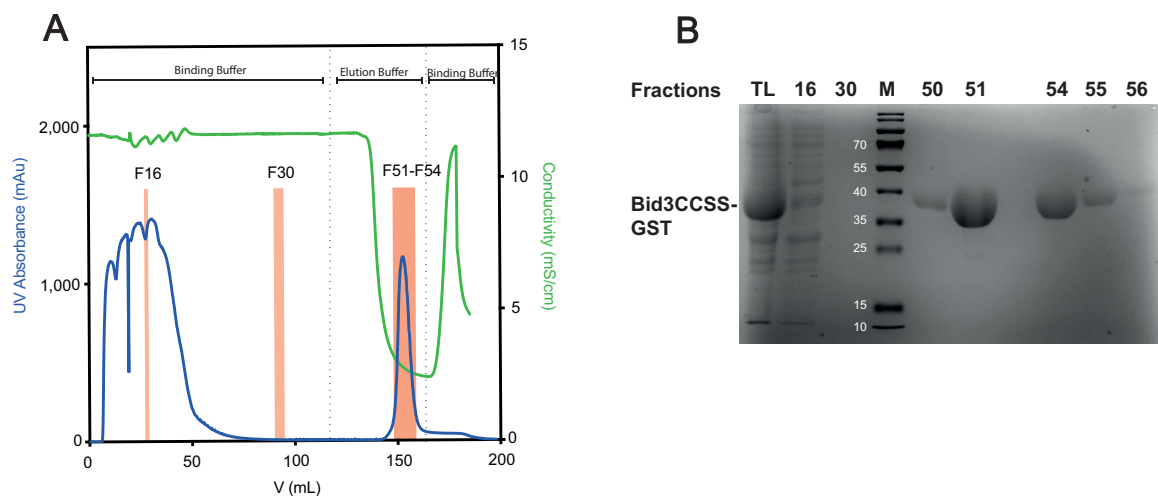


Figure 24. Representative result of Bid3CCSS-GST purification using GSH HiCap column. A) Purification chromatogram of BidCCSS-GST. Blue curve represents the UV/Vis absorption that shows a prominent peak at around 150 mL when Bid3CCSS is eluted from the column. **B)** Coomassie staining demonstrated a remarkable overexpression of Bid3CCSS (~40kDa) in the total lysate (TL). In the flow-through (F16) far less Bid3CCSS was detected, whereas in F30 no protein was found. After Bid3CCSS elution using the GSH elution buffer, most of the desired protein was detected in F51-54. These fractions were subsequently pooled and subjected to thrombin cleavage.

Results

Removal of the GST-tag often resulted in a partial precipitation of the largely hydrophobic Bid3CCSS protein. The precipitate was removed by centrifugation and sterile filtration to avoid disturbances during size exclusion chromatography (SEC).

SEC was performed using a HiLoad 16/1600 Superdex 75 column. The smaller Bid3CCSS protein was eluted following the bigger GST-tag after about 75 mL of gel filtration buffer was rinsed through the column (Figure 25 A). The successful purification was confirmed by SDS-PAGE/ Coomassie staining. The thrombin cleavage (TC) fraction, which was collected directly after the thrombin cleavage without further purification, showed only a very faint band at around 40 kDa representing the non-cleaved Bid3CCSS-GST construct (Figure 25 B TC). Instead, intense bands for the GST-tag (~25 kDa) and the cleaved Bid3CCSS protein (~17.5 kDa) indicated a successful cleavage of the former Bid3CCSS-GST protein (Figure 25 B TC). After SEC, the GST-tag and the purified Bid3CCSS protein were clearly separated. Bid3CCSS was usually obtained in the fractions 30-40 (Figure 25 B 32-37). In the depicted representative Coomassie staining result (Figure 25 B), F34+35 were most significantly enriched with Bid3CCSS (Figure 25 B F34, F35). Thus, these fractions were then pooled, and concentrated by centrifugation to a concentration of 10 - 15 mg/ mL.

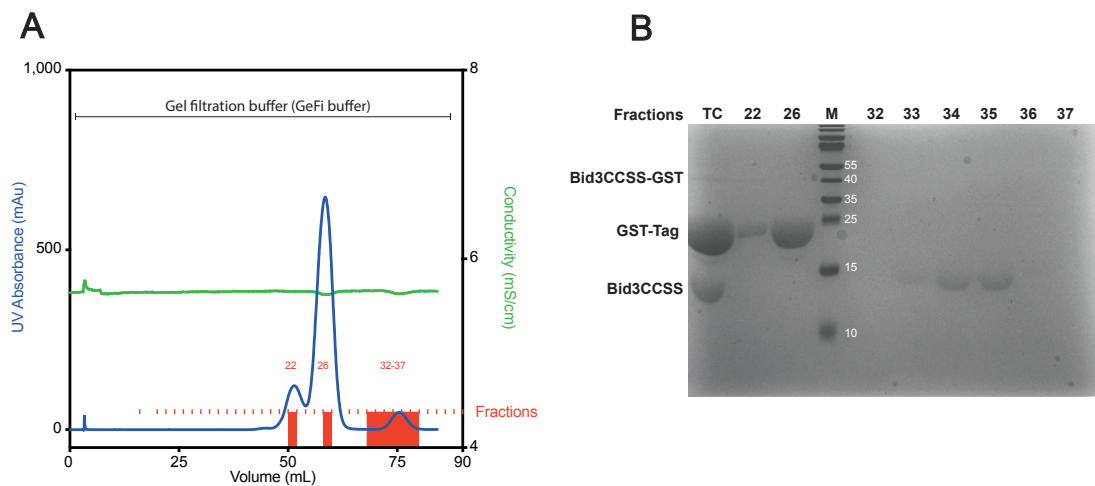


Figure 25. Representative result of Bid3CCSS purification using size exclusion chromatography. **A)** SEC chromatogram after Bid3CCSS-GST thrombin cleavage. UV absorption (blue curve): First peaks represent the GST tag, whereas the small peak at about 75 mL represents the Bid3CCSS construct. **B)** The representative Coomassie staining result additionally show the successful thrombin cleavage (Thrombin cleavage (TC); before SEC). In F22 + F26 the GST-tag was confirmed (~25 kDa). Furthermore, analysis of the fractions from the second peak revealed that the Bid3CCSS protein (~17.5 kDa) was mostly enriched in fractions 34+35.

To finally clarify the identity of the purified Bid3CCSS protein all batches were analyzed using mass spectroscopy (ESI-MS of intact proteins). Furthermore, this analysis was conducted to exclude the presence of impurities such as cleavage side products in the protein solution which could compromise the crystallization. These measurements confirmed that all protein batches used for Bid3CCSS crystallization were of high purity and without any contaminations (Figure 26).

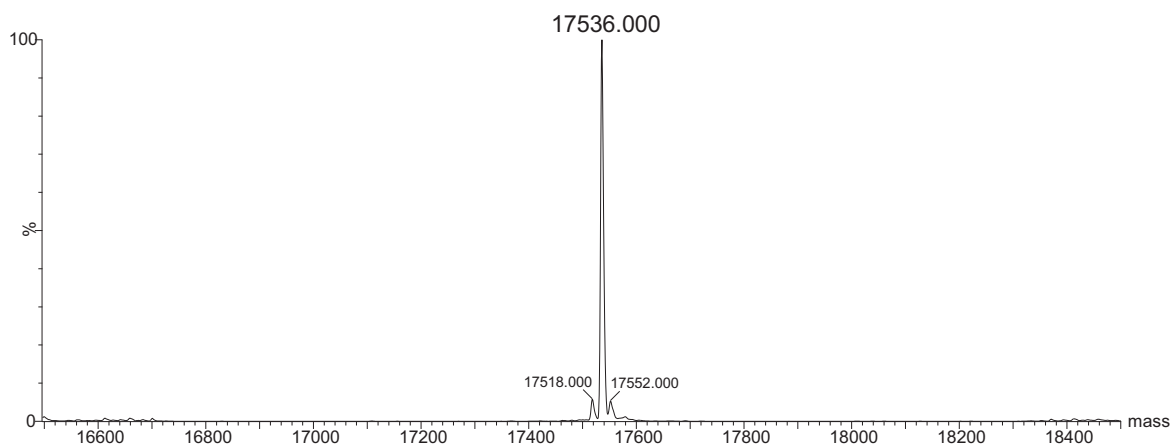


Figure 26. MALDI TOF analysis. Representative deconvoluted Maldi TOF (MS ES+) data showed that the Bid3CCSS protein (M (theoretical): 17.536 g/mol) was obtained in a highly pure fashion.

3.1.2. Optimization of the Bid3CCSS crystallization conditions

3.1.2.1. Bid3CCSS crystallization in the native Morpheus A5 condition

Previous crystallization attempts using the Bid3CCSS construct revealed that the best crystallization results were obtained in the Morpheus A5 condition (Table 33). Preliminary optimization of these first hit condition did not lead to an improvement of the crystal growth ¹⁰⁰.

Table 33 Original Morpheus A5 conditions

		Concentration stock solution	Final concentration
Divalent cations 10%	MgCl ₂	0.3 M	30 mM
	CaCl ₂	0.3 M	30 mM
Buffer System 2 10%	MOPS	0.5 M	50 mM
	Na-HEPES	0.5 M	50 mM
	pH	7.5	
Precip Mix 1 50%	PEG550 MME	40 % v/v	20% v/v
	PEG20000	20 % m/v	10% m/v

All subsequent crystallization experiments conducted in this study were done manually with stocks prepared by hand instead of the commercially available solutions from the Morpheus screen. Nevertheless, crystallization could be reproduced using the Morpheus A5 condition, resulting in small, very intergrown crystals (Figure 27), similar to those previously obtained ¹⁰⁰.

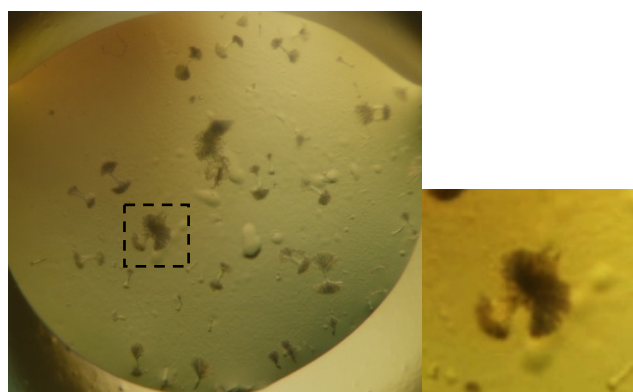


Figure 27. First crystals obtained in the Morpheus A5 condition.

Supplementing the crystallization condition with Jeffamine-M 600, which appeared to improve crystal quality in the Marxthal screens, did not improve the crystallization here. Furthermore, also the usage of detergents like 1% Triton X100, Tween 20 or Mega 8 in concentrations between 1-30 mM, did not change crystal shape towards less ingrown crystals. Hence, no further attempts using additive were performed.

Next, the influence of the protein concentration on crystallization behavior was investigated. Therefore, Bid3CCSS protein was further diluted from a 12 mg/ mL stock concentration with gel filtration buffer to concentrations of 9 mg/ mL and 6 mg/ mL, respectively, and tested in the native Morpheus A5 conditions. A decrease in protein concentration worsened crystal quality from large ingrown crystals (Figure 28 A) to a very high number of microcrystals (Figure 28 B, C). Therefore, protein concentrations of 10 - 15 mg/ mL were used for further experiments.

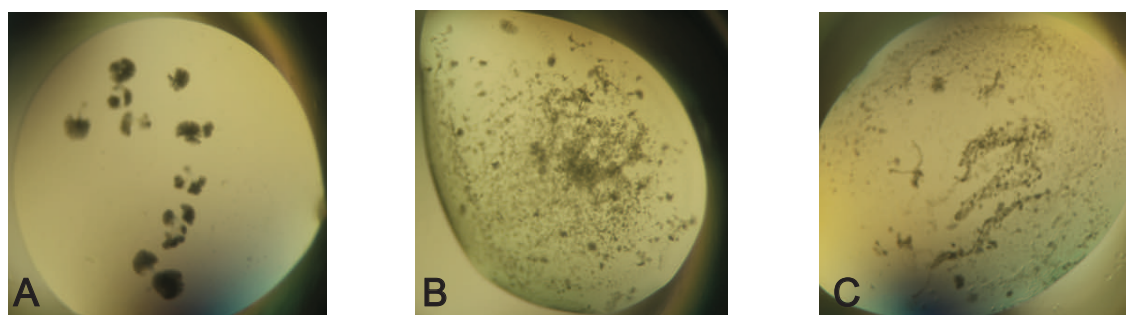


Figure 28. Effects on Bid3CCSS protein concentration on crystallization. Bid3CCSS were tested in protein concentrations of **A)** 12 mg/ mL, **B)** 9 mg/ mL and **C)** 6 mg/ mL in the Morpheus A5 condition. Protein concentrations above 10 mg/ mL resulted in the best crystal growth.

Moreover, flash-freezing of the Bid3CCSS protein solution with liquid nitrogen and subsequent storage at -80°C or extended protein storage over 3-4 month at 4°C worsened crystallization. Although crystal shape and length did not significantly differ from those obtained from fresh protein solution stored at 4°C , the probability for successful crystal growth decreased by almost 80%.

3.1.2.2. Decomposition screen

The Morpheus A5 crystallization condition is composed of two different divalent salts, two buffer reagents and two different precipitants (Table 33). These six different variables could have an individual influence on the crystallization behavior

Results

of the Bid3CCSS protein. Therefore, a decomposition screen was performed to test which substances were indispensable for crystal growth and which were superfluous. A crystallization protocol containing fewer reagents reduces screening variables and enhances reproducibility. Thus, the probability of successful optimization of the hit conditions is increased. Therefore, the Bid3CCSS was crystallized under Morpheus A5 conditions, sequentially omitting one of the components at a time (Figure 29).

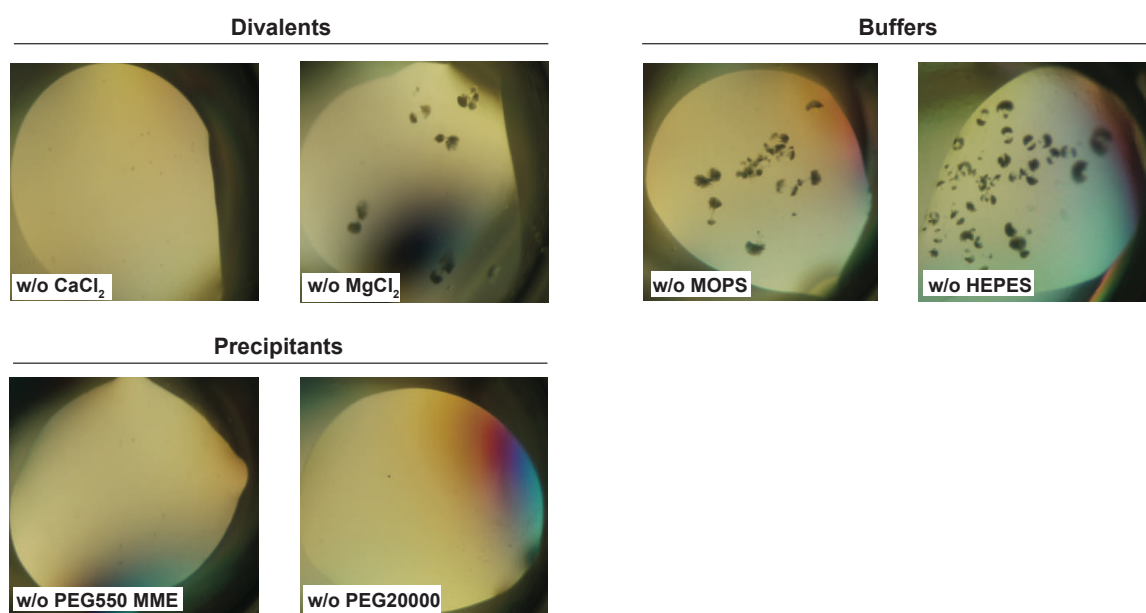


Figure 29. Decomposition screen. Bid3CCSS was crystallized in the Morpheus A5 condition, omitting one component at a time. The removal of CaCl₂ (w/o CaCl₂), PEG550 MME (w/o PEG550 MME) and PEG20000 (w/o PEG20000) subsequently abolish crystal growth, whereas crystallization was still possible without MgCl₂ (w/o MgCl₂) or without one of the buffer components (w/o MOPS)/ (w/o HEPES). Images show representative results from three wells per condition.

With respect to the divalent salts, it became obvious that CaCl₂ was of major importance for crystal growth, since crystallization was completely abolished when CaCl₂ was omitted. In contrast, the removal of MgCl₂ did not significantly affect Bid3CCSS crystallization, indicating that MgCl₂ is not necessary for crystal formation. For the buffer system (containing HEPES and MOPS), it was noted that one of the buffers was sufficient to maintain crystal growth. On the contrary, the removal of one of the precipitants (PEG550 MME + PEG20000) completely abolished crystal formation indicating that both precipitants were essential in the crystallization condition.

3.1.2.3. Matrix buffer screen

As demonstrated in the decomposition screen, when one buffer was omitted, crystallization was still. However, it was still questionable, whether both buffers together provided even better crystallization conditions than one buffer alone. The pH-value of the buffer solutions was fixed to pH 7.5 during these experiments.

At the start, different buffer concentrations of buffer system 2 (equal concentrations of HEPES and MOPS) were tested in the range from 0 – 190 mM. Moreover, both buffers were tested alone in the same ratio of 0 – 190 mM. These experiments indicated that buffer concentrations >160 mM resulted in the formation of more and thicker crystals. However, this effect was most prominent for buffer system 2 and MOPS (Figure 30 A-C).

Afterwards, HEPES and MOPS buffers were screened as described before, whereas one of the buffer components was fixed to 100 mM (Figure 30 D, E). The best crystals were obtained in the condition 180 mM MOPS/ 100 mM HEPES (Figure 30 E).

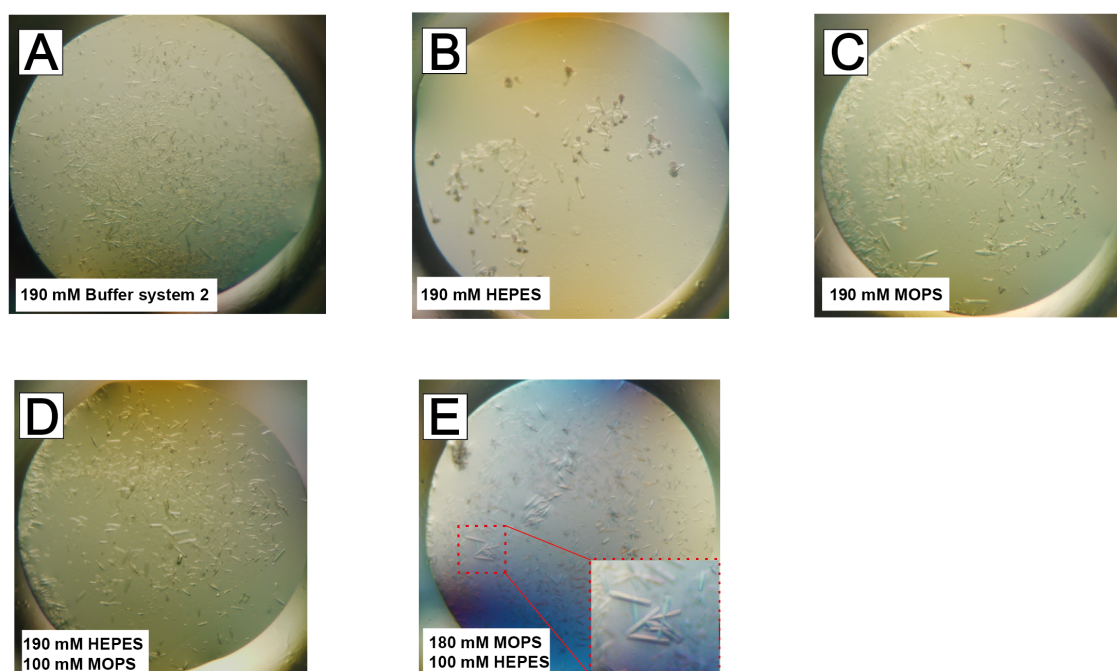


Figure 30. MOPS and HEPES buffer screen. Buffer screen was performed with 30 mM CaCl₂ and 50% Precip mix 1. Buffer system 2 contained HEPES and MOPS in equal quantities. For all buffer screens the following steps were applied: 50 mM-190 mM in 10 mM steps. **A-E)** Representative images of the best conditions in the respective screens. **E)** In the 180 mM MOPS/ 100 mM HEPES condition the best crystals were obtained which grew larger than all other crystals and were almost not ingrown.

3.1.2.4. PEG and pH screen

For the PEG screen either Precip 1 Mix was tested in a range from 0 – 75 % or PEG550 MME and PEG20000 were analyzed individually, whereas one of the components was fixed to 20%. However, the original condition of 50% Precip 1 Mix still provided the best crystal growth and thus was kept unchanged for the further experiments. Additionally, pH screening was conducted which did not result in the formation of better crystals. Therefore, pH 7.5 was retained for the buffer solutions.

3.1.2.5. Salt screen

CaCl₂ was screened in a range of 0 – 120 mM. Like the results from the buffer screen, higher salt concentrations enhanced crystal growth. However, this trend did not continue when a second screen was performed testing CaCl₂ concentrations of up to 200 mM. Therefore, 100 – 120 mM was identified to be the optimal CaCl₂ concentration which resulted in the formation of the best crystals obtained so far (Figure 31 A). Several of these crystals were measured at the DESY (Deutsches Elektronen-Synchrotron). X-ray measurements revealed diffraction patterns of a resolution of 1.96 Å at 0° (Figure 31 B left image). However, at 90°, no significant diffraction was observed (Figure 31 B right image). This indicated that the crystals were still too small in one dimension i.e., too thin, to measure a complete data set for structure determination. Furthermore, the crystals showed ice ring formation, even though 50% Precip Mix 1 was already used during crystallization.

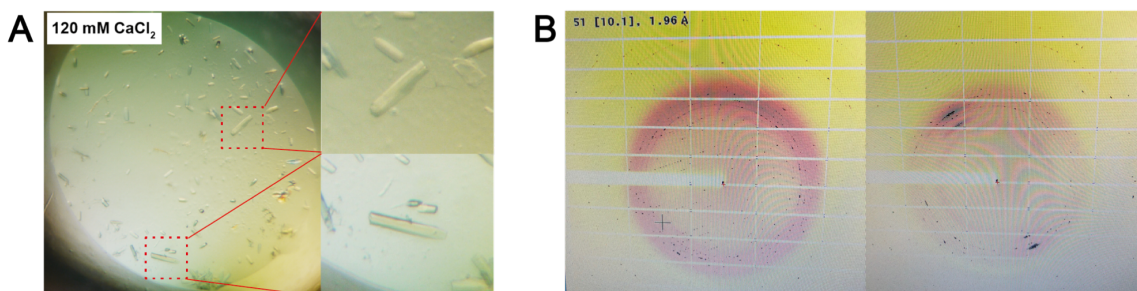


Figure 31. CaCl₂ screen and X-ray scattering images. Higher CaCl₂ concentrations (100 - 120 mM) yielded crystals with an improved crystal shape. **A)** Representative image of crystals obtained from the high salt conditions. **B)** X-ray scattering images revealed a good resolution of 1.96 Å at 0° (left image), but no diffraction was detected at 90° (right image) indicating that the crystals are still too thin.

In summary, after the optimization procedure the crystallization condition could be refined to the optimized Morpheus A5 condition as detailed in Table 34.

Table 34 Optimized Morpheus A5 condition

		Final concentration
Divalent cations 10%	MgCl ₂	---
	CaCl ₂	100 mM
Buffer System 2 10%	MOPS	180 mM
	Na-HEPES	100 mM
Precip Mix 1 50%	PEG550 MME	20% v/v
	PEG20000	10% m/v

3.1.2.6. Seeding protocol and cryoprotection

The best apo crystals (without ligands) obtained in the salt screen were used as seeding crystals for a streak seeding protocol using a horsehair. This approach yielded nicely shaped crystals of a proper size (Figure 32). Since the crystals were prone to ice ring formation, suitable cryo-conditions were determined in regard to 10% DMSO based on the original buffer and with 25% PEG400 as cryo-protectant. These cryo-protected crystals diffracted to 3.3-3.7 Å inhouse without ice rings, making them suitable for further measurements at the DESY.



Figure 32. Bid3CCSS crystals obtained after streak seeding. To further enhance crystal growth and shape, nicely grown apo crystals from the salt screen were crushed in the crystallization buffer and subjected to a seeding protocol using a horsehair. Images show that this approach yielded non-ingrown crystals of a good size. (Images were captured using a polarization filter).

3.1.3. First crystal structure of Bid3CCSS

The apo crystals obtained using the seeding protocol were measured at the synchrotron where several complete data sets were received with a resolution of 2.0 - 2.3 Å at stringent quality criteria (Completeness > 95 %, $R_{\text{sym}} < 60$ %, $I/\sigma > 2$). However, attempts to solve the Bid3CCSS crystal structure by phase determination using molecular replacement with the available NMR structure did not work. Therefore, several Bid3CCSS crystals were subjected to heavy metal soaking (gadolinium acetate, lanthanum chloride, yttrium chloride) in order to determine the phase. For the crystals soaked with gadolinium acetate, a strong anomalous signal was detected in an anomalous signal scan at BESSY and a single-wavelength anomalous diffraction (SAD)-dataset with a resolution of ~2.8 Å was collected. The phases, determined using the Autosol program from the Phenix-suite, were then applied to the 2.15 Å native data set (Figure 33 A). From this data, the first crystal structure of Bid3CCSS was modeled (Figure 33 B), although several loops had to be rebuilt and relinked.

Interestingly, Bid3CCSS crystallizes in a trimeric assembly. Even though, Bid3CCSS is a highly helical protein, some regions of two monomers were largely disordered so that the quality criteria for refinement were worse than it would be expected for a crystal structure with a resolution of 2.0 Å – 2.3 Å (Figure 33).

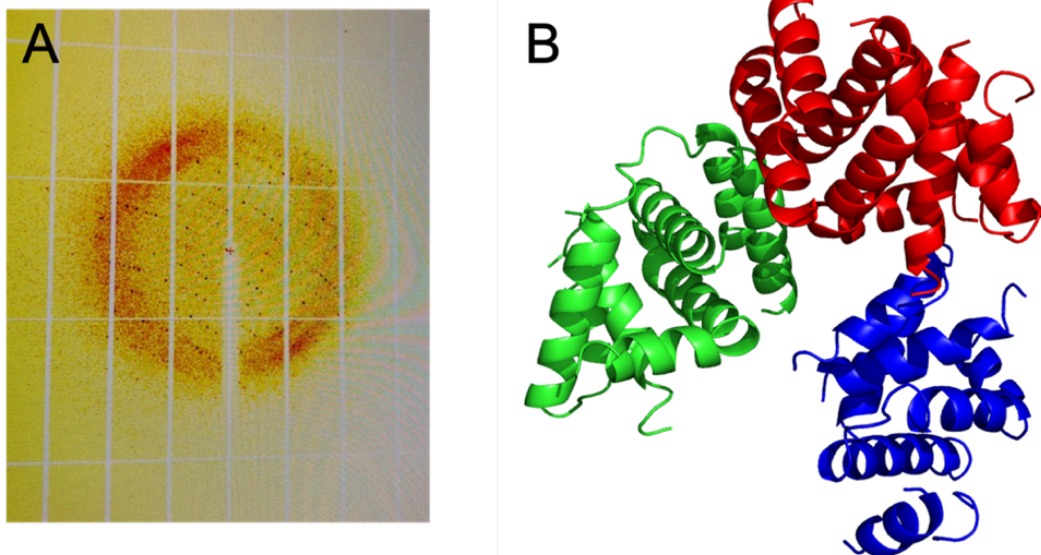


Figure 33. Diffraction pattern of a representative Bid3CCSS apo crystal and the modeled Bid3CCSS structure. A) Diffraction pattern of a crystal obtained with seeding. **B)** The first crystal structure of Bid3CCSS modeled from the data sets obtained in A. Phase determination was conducted using gadolinium acetate-soaked crystals ($R_{\text{work}} = 31.16 < R_{\text{free}} = 34.25$, $R_{\text{expected}} \sim 21$). Each monomer of the trimer is depicted in a different color.

3.1.4. Functional analysis of the Bid3CCSS protein

To investigate whether the recombinant Bid3CCSS construct exhibited biological effects, the protein was tested on isolated mitochondria from the prefrontal cortex of Sprague-Dawley rats in the coupling assay using the Seahorse system. This enables the analysis of alterations in the oxidative phosphorylation (OXPHOS) in mitochondria, i.e., after compound application.

Isolated mitochondria were diluted in MAS buffer containing complex II substrate succinate to fuel the oxidative phosphorylation machinery and the complex I inhibitor rotenone to avoid reverse electron flow¹⁶¹. Bid3CCSS was assayed at concentrations of 0.1 and 1 μg Bid3CCSS protein per well. To avoid issues with the gel filtration buffer of Bid3CCSS in the Seahorse assay, the buffer was exchanged to PBS before starting the experiments. Interestingly, PBS alone already altered OCR (Figure 34 A) so that the total PBS volume was adjusted to 2 μL for every condition. In the experiments, Bid3CCSS or PBS was added to the isolated mitochondria and incubated for 15 min at 37°C in a water bath before the coupling assay was performed. The representative results revealed that treatment with 0.1 μg of the Bid3CCSS only showed a slight tendency towards decreased mitochondrial respiration, whereas 1 μg Bid3CCSS clearly impaired mitochondrial OXPHOS (Figure 34 B).

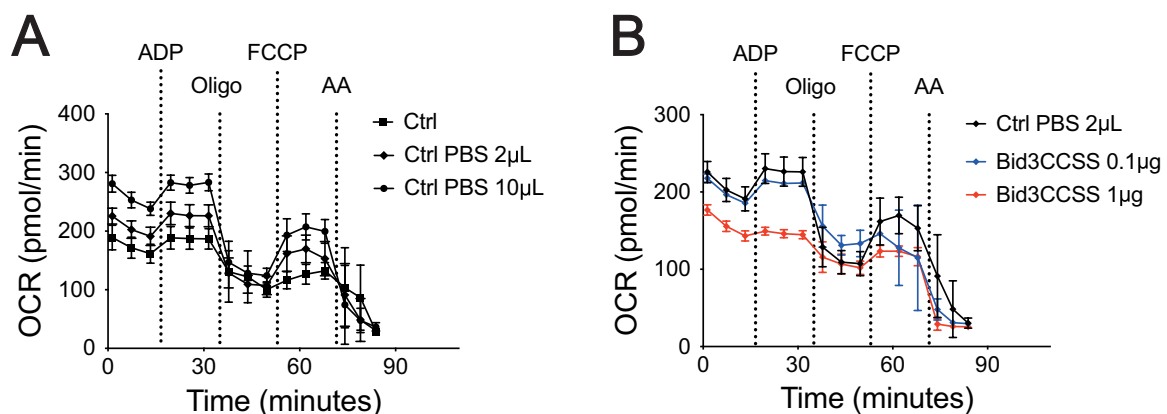


Figure 34. Seahorse assay of the Bid3CCSS protein on isolated mitochondria. Both figures show representative results of $n=3-6$ wells of isolated mitochondria (8 μg mito protein/ well) incubated at 37°C for 15 min with either PBS alone or with 0.1 or 1 μg of Bid3CCSS protein per well diluted in 2 μL PBS. **A)** OCR was increased by increasing PBS concentrations. **B)** 0.1 μg Bid3CCSS treatment only caused a slight decrease in OCR, whereas a striking reduction in OCR was observed upon 1 μg Bid3CCSS treatment.

To investigate the effect of the Bid3CCSS construct on the mitochondria in greater detail, the results of five individual measurements were pooled. In order to adjust for differences in basal respiration, basal OCR of the PBS control was set to 100 % for each single experiment. All other respiratory states were determined with respect to the respective basal OCR (Figure 35).

Basal respiration, that is mainly driven by complex II activity in an ADP-independent way ¹⁶¹, was strikingly decreased by 1 µg Bid3CCSS application. ADP driven oxidative respiration (state 3) was initiated by ADP injection that led to a subsequent increase in oxidative phosphorylation and consequently to an increase in OCR. 0.1 µg Bid3CCSS application attenuated this increase, whereas the treatment of 1 µg of Bid3CCSS led to a significant reduction in state 3 respiration compared to control. Thereafter, state 4_o was analyzed which was initiated by application of the ATP synthase inhibitor oligomycin. In this state, the resulting OCR is attributed to proton leakage, which is, however, not altered by Bid3CCSS application. Afterwards, the protonophore FCCP was injected that caused a disruption of the proton gradient. Hence, OCR was uncoupled from the ATP generation process, facilitating state 3_u respiration. Even though a tendency towards decreased state 3_u respiration was detectable upon Bid3CCSS construct application, this was not statistically significant. Additionally, the respiratory control ratio (state 3/ state 4_o) was calculated as an intrinsically controlled measure for overall mitochondrial energetic dysfunction ¹⁶². This marker was again only attenuated but not significantly changed upon 0.1 µg Bid3CCSS application. However, a significant decline in the overall energetic constitution of the mitochondria was demonstrated when the mitochondria were treated with 1 µg Bid3CCSS, in particular, due to the strong detrimental effects of the Bid3CCSS construct on mitochondrial OXPHOS.

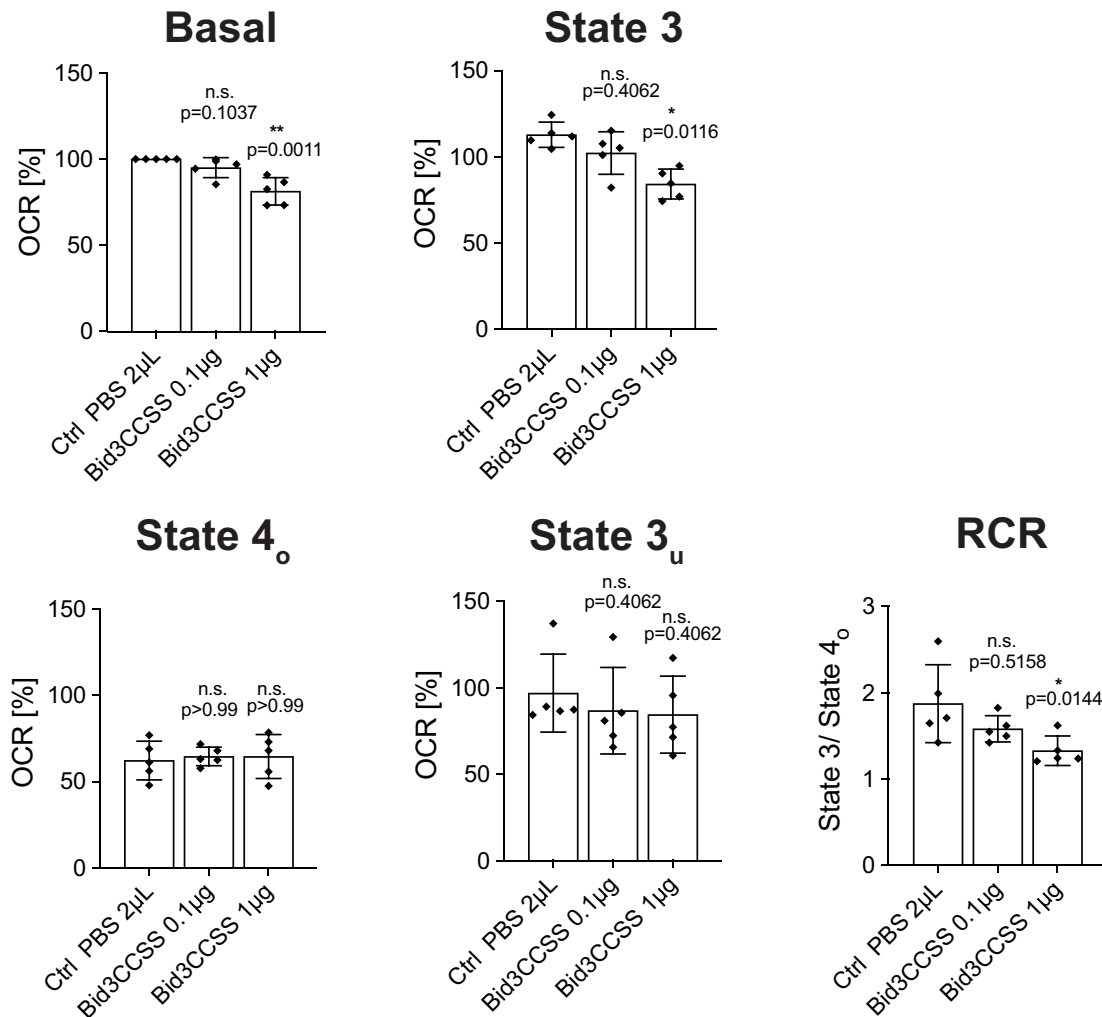


Figure 35. Analysis of the respiratory states in isolated mitochondria after Bid3CCSS treatment. Determination of the respiratory states in relation to each PBS control, as detailed in the method section, from $n=5$ independent results from the coupling assays (diamond-shaped dots). Basal state (ADP independent respiration): Before ADP injection, state 3 (oxidative phosphorylation): after ADP injection, state 4_o (non-phosphorylating respiration/ Proton leak): after oligomycin injection, state 3_u (maximal respiration): after FCCP injection. Results are depicted as mean \pm S.D.; statistical analysis was performed using Kruskal-Wallis test followed by Dunn's multiple comparison; * $p < 0.05$, ** $p < 0.01$ compared to PBS control.

3.2. Characterization of novel diphenylamine compounds as ferroptosis inhibitors

Having set a basis for future structure-based design of novel BID inhibitors in the future in the first part of this thesis, simultaneously the promising approach of developing novel compounds through a medicinal chemistry approach using BI-6c9 as a scaffold structure was further pursued.

In order to increase the potency against oxidative cell death pathways, the antioxidative diphenylamine (DPA) structure was introduced into the BI-6c9 backbone for the development of new compounds. In addition, the ability for mitochondrial protection should be preserved. Preliminary MTT screenings confirmed that the DPA compounds 1-3 were the most protective derivatives against glutamate induced oxytosis. Therefore, in the second part of this thesis, these compounds were further characterized in erastin, and RSL-3 induced ferroptosis. Moreover, important markers of ferroptosis, i.e., ROS development, mitochondrial impairments and other cellular and biochemical endpoints were investigated, to gain a more detailed insight into the potential mode of action of the compounds.

3.2.1. Erastin and RSL-3 induced cell death in HT22 cells

For most experiments the immortal mouse hippocampal HT22 cell line was used. When these cells were treated with ferroptosis inducers such as erastin or RSL-3, cells undergo a concentration dependent cell death response. Concentrations of 0.1 μM of erastin were sufficient to kill approximately 50 % of HT22 cells. Concentrations between 0.3 – 1 μM typically resulted in a cell death rate above 80 % (Figure 36 A). In comparison, RSL-3 treatment induced oxidative cell death regularly at 0.03 μM , whereas concentrations higher than 0.1 μM usually resulted in cell death rates over 80 % (Figure 36 B). For most experiments, erastin concentrations between 0.4 – 0.6 μM and RSL-3 concentrations between 0.1 – 0.2 μM were chosen. However, the cell death responses to these ferroptosis inducers could sometime vary between cell passages, cell densities and cell lines. Hence, the amount of cell death inducers applied were adjusted for some experiments to achieve similar control cell death rates between experiments. Nevertheless, doses beyond 1 μM of both ferroptosis inducers were avoided to exclude unspecific effects of erastin or RSL-3 on biomolecules apart from their main target structures.

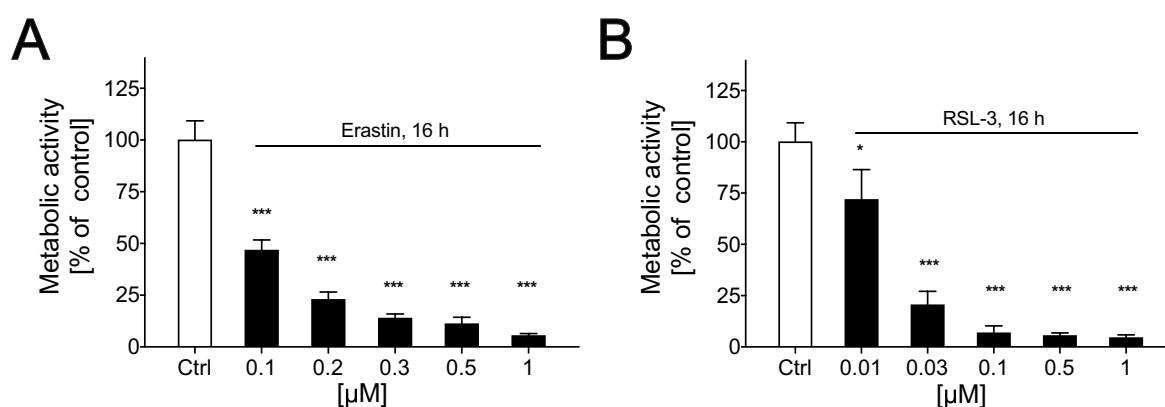


Figure 36. Ferroptosis induction in HT22 cells upon erastin and RSL-3 treatment. Concentration dependent induction of ferroptotic cell death upon erastin **A**) and RSL-3 **B**) measured in MTT assays 16 h after the treatments. Erastin showed substantial decrease in cell viability from 0.3 - 1 μM , whereas RSL-3 showed its maximal cell toxic effect already between 0.1-1 μM . Data are shown as mean + SD. * $p < 0.05$; *** $p < 0.001$ compared to untreated control (ANOVA, Scheffé's test).

Erastin and RSL-3 treatment resulted in strong morphological cellular and mitochondrial alterations. Non-treated HT22 cells display a spindle-shaped elongated structure (Figure 37 BF Control). After 10 h of erastin exposure, the cell morphology was changed to a circular shape with loosened cell contacts (Figure 37 BF Erastin). For RSL-3, at the 10 h time point an even advanced cell death stadium was observed (Figure 37 BF RSL-3), where the cells were already completely rounded-up, largely separated from each other, and a significant proportion of the cells were already detached from the well bottom. This is, however, not surprising, since RSL-3 is a direct inhibitor of GPX-4 and, therefore the time for the upstream effects of cystine and GSH depletion was circumvented. Moreover, the cell death response was accompanied by strong mitochondrial impairments. In healthy HT22 cells, mitochondria were elongated and distributed in the whole cell (Figure 37 MT/ Composite Control), whereas 10 h of erastin and RSL-3 application led to intense fragmentation of the mitochondria (Figure 37 MT/ Composite Erastin, RSL-3).

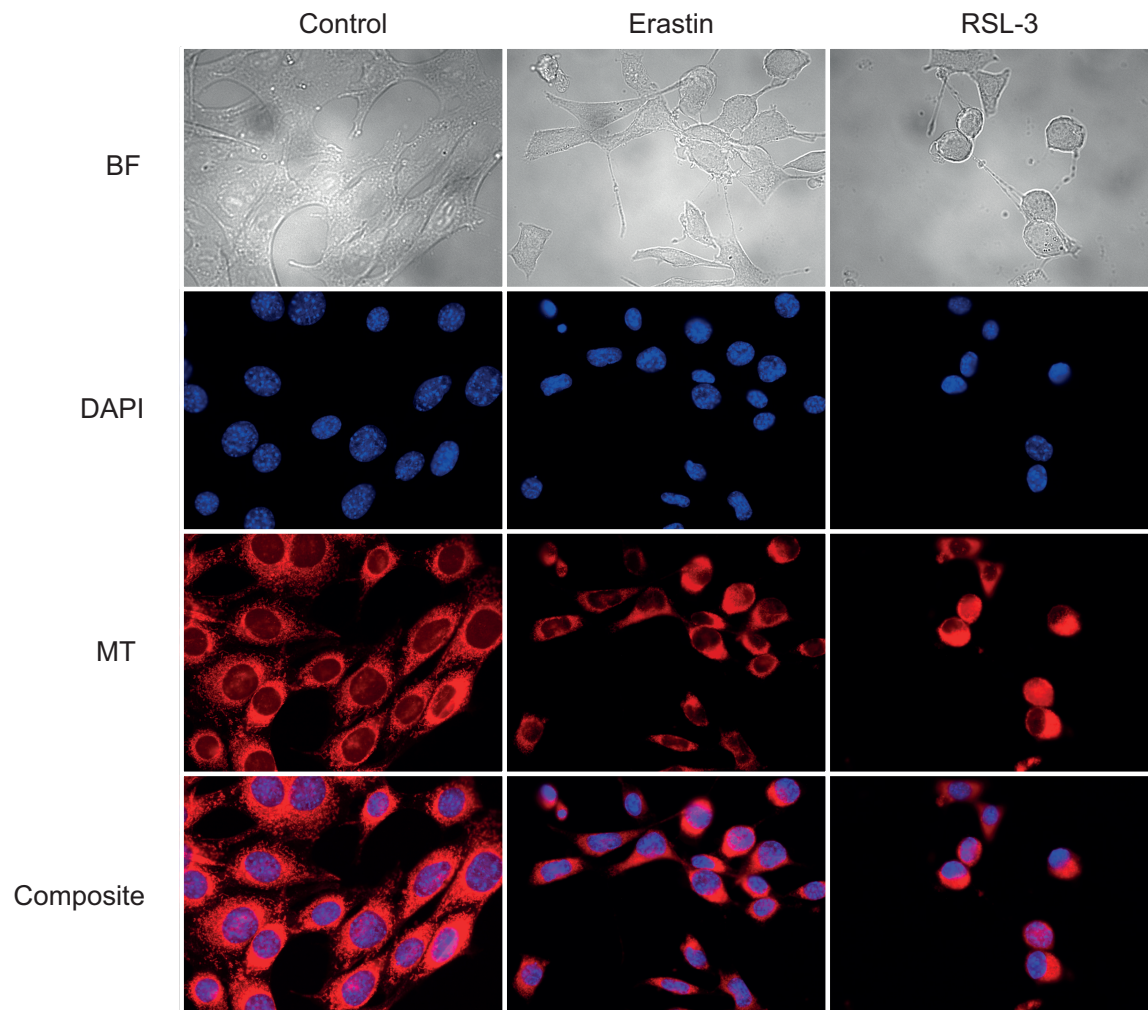


Figure 37. Alterations of cells and mitochondrial morphology due to ferroptosis induction. Bright field (BF) and fluorescence images (DAPI, MT=Mitotracker deep red) after 10 h of erastin and RSL-3 treatment. **BF images** show that cell morphology changed from a spindle-shaped form of the control cells to rounded-up cells as depicted for erastin and RSL-3. Moreover, mitochondrial morphology (**MT images**) was also significantly impaired by erastin and RSL-3 treatment resulting in condensed mitochondria which were located around the nucleus (**DAPI**). **Composite:** merged images of DAPI and MT channel. Images were received after respective staining (MT: 0.2 μ M, 30 min, DAPI: 1 μ g/mL 30 min) and subsequent fixation using 4% PFA solution with the Leica fluorescence microscope. (Magnification 63x oil; scale bar: 100 μ M)

3.2.2. Time dependent development of ferroptosis hallmarks

To shed more light on the mechanisms of how ferroptosis hallmarks evolve in HT22 cells that lead to mitochondrial damage and cell death, time course experiments were executed. Understanding this process is critical for the following examination of how the novel DPA compounds might interfere with the ferroptosis signaling pathways.

To follow the ferroptosis cascade, the first emerging event is the decrease of glutathione levels, starting 3 h after ferroptosis induction, but was most strongly reduced after 6 h of erastin treatment (Figure 38 A). Concurrent with the decreased glutathione levels, cytosolic and lipid ROS formation were at their peak concentrations at 6 h after ferroptosis initiation and then persistent over time (Figure 38 B, C). On the contrary, at earlier time points of 2 h and 4 h after onset of erastin exposure, ROS and lipid ROS levels were still at control levels.

Interestingly, mitochondria were not harmed at all at the 6-hour time point. This is reflected from both, the absence of mitochondrial ROS (Figure 38 D) and the fully intact mitochondrial membrane potential (Figure 38 E). However, at the 8 h time point, mitochondrial ROS formation increased to ~50% of its maximal effect, and simultaneously mitochondrial membrane potential was decreased to approximately the same extent (Figure 38 D, E), representing the onset of mitochondrial impairment. Furthermore, this fatal trend proceeded for the next two hours, so that after 10 h mitochondrial ROS formation reached its peak and most of the cells had lost their mitochondrial membrane potential. Remarkably, the temporal evolution of the impairments of mitochondrial parameters largely parallels cell death development (Figure 38 F). Similarly, after 8 h of erastin treatment, cell death rate started to increase, reaching its maximal manifestation after 10 h, which afterwards did not significantly change any further over the next 14 h. These results demonstrated a close relationship between mitochondrial constitution and cell viability.

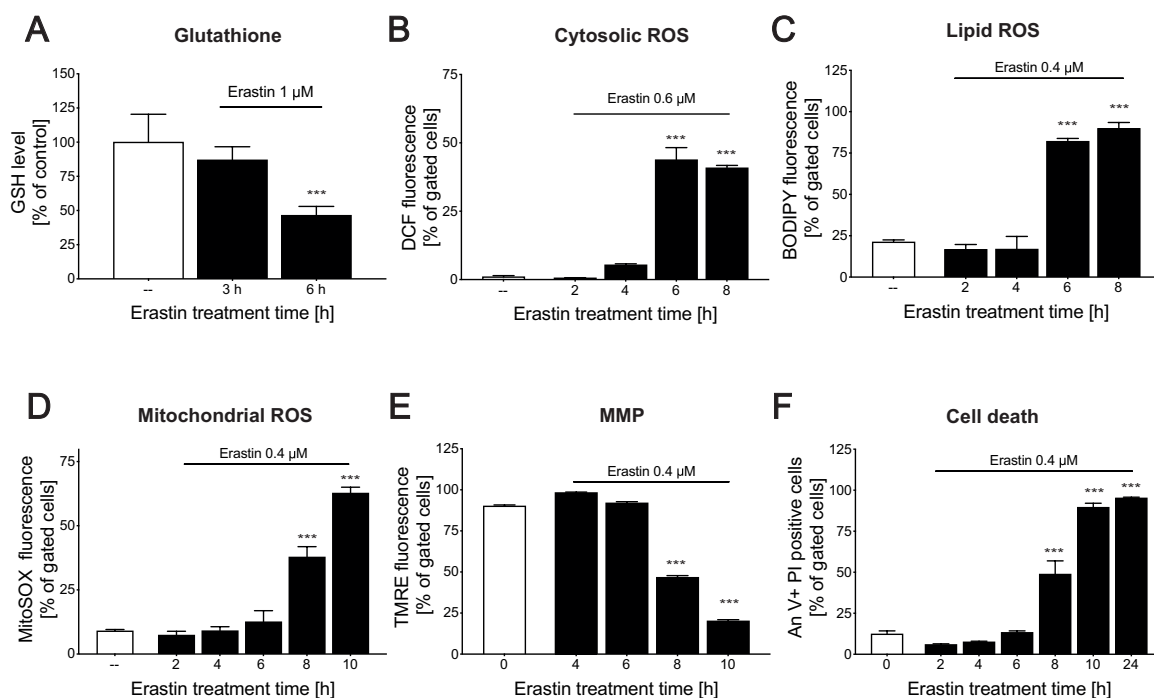


Figure 38. Development of ferroptosis hallmarks over time. Ferroptosis was induced with erastin (0.4 -1 μ M) for the indicated time span, before the respective hallmarks were analyzed. **A)** Measurements of glutathione levels revealed a strong decrease after 6 h of erastin induction. Coinciding with this event, cytosolic ROS **B)** and lipid ROS **C)** were also significantly increased after 6 h. Mitochondrial ROS formation **D)** and a loss of mitochondrial membrane potential (MMP) **E)** were not detected until 8 h after ferroptosis initiation. Similar results were found for cell death **F)** that occurred not before 8 h after erastin treatment. Data are shown as mean + SD of **A)** $n = 5$ and **B-F)** $n = 3$. *** $p < 0.001$ compared to untreated control (ANOVA, Scheffé's test).

3.2.3. DPA compounds provided protection against ferroptosis

To start the characterization process of the DPA compounds, the protective potency against ferroptosis was analyzed in HT22 cells. Therefore, increasing concentrations of the novel compounds between 0.025 - 1 μM were applied with co-treatment of erastin for 16 h. After 16 h, metabolic activity was analyzed via MTT assay, depicting a clear concentration-dependent protection of these compounds (Figure 39 A – C). Results from at least three independent MTT experiments were then pooled and fitted for EC50 determination. The calculations revealed EC50 values at a low micromolar range between 0.30 μM (Figure 39 D) and 0.32 μM (Figure 39 E) for the amino acid derivatives and 0.23 μM for the tert-butyl derivative (Figure 39 F). Notably, compound concentrations of 1 μM provided full protection against ferroptotic cell death for all three compounds.

In addition, real-time impedance measurements using the xCELLigence system confirmed the results of the MTT assays (Figure 39 G – I). After 8 – 12 h of erastin treatment a drop in impedance was detected, reflecting the detachment of the dying cells from the well bottom (Figure 39 G – I ✖). At EC50 the compounds were only able to attenuate the decline in cell index following ferroptosis induction (Figure 39 G – I ↻), whereas erastin induced decline of the cell index was fully prevented at EC100 (Figure 39 G – I ↻), without intrinsically altering the cell index in absence of erastin (Figure 39 G – I ■/ ■/ ■).

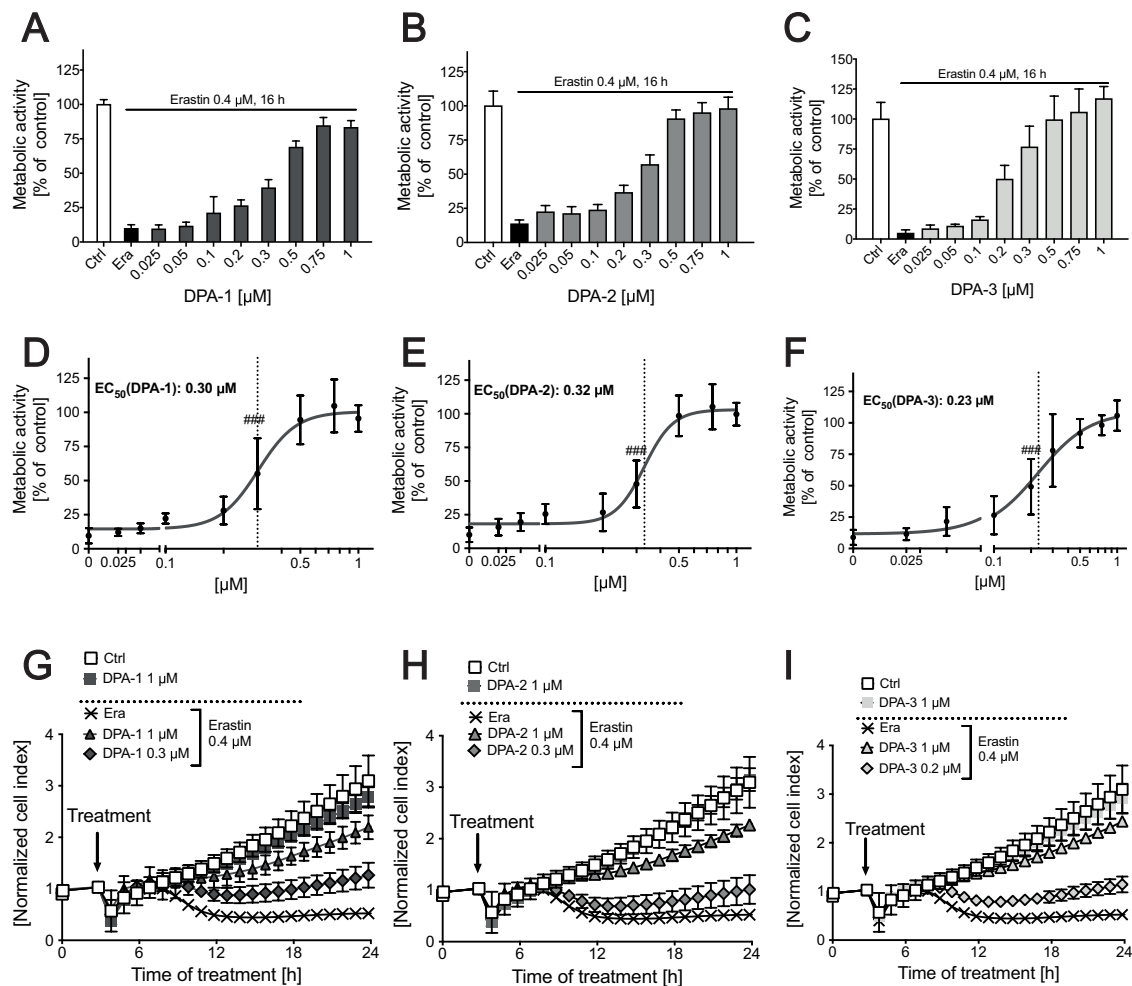


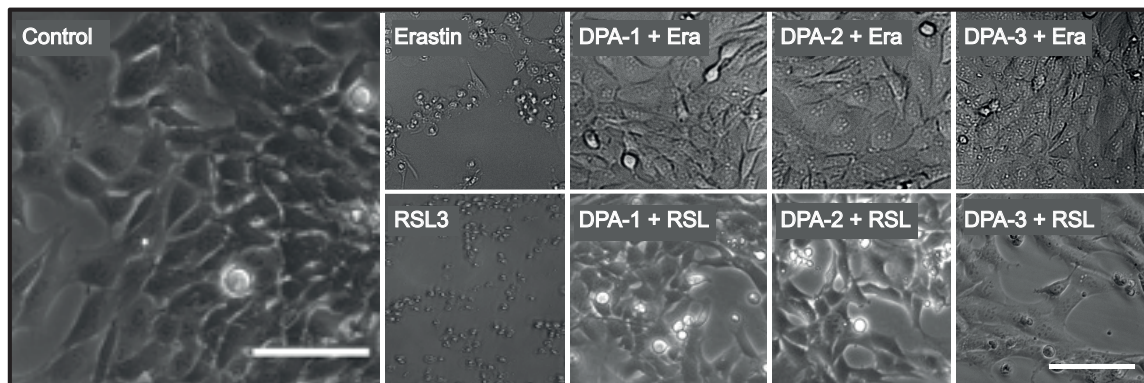
Figure 39. EC₅₀ determination and real-time impedance measurements revealed a marked anti-ferroptotic effect of the novel diphenylamine compounds. **A-C)** Representative MTT measurements after co-treatment of erastin (0.4 μ M) with respective concentrations of the diphenylamine compounds in HT22 cells for 16 h. **D-F)** EC₅₀ determination, based on 3 – 5 independent MTT experiments as shown in A) revealed a dose-dependent protection against ferroptotic cell death. EC₅₀ values (dotted lines) were calculated using the prism software: **D)** EC₅₀ (DPA-1): 0.30 μ M; **E)** EC₅₀ (DPA-2): 0.32 μ M; **F)** EC₅₀ (DPA-3): 0.23 μ M. **G-I)** Real-time impedance measurements demonstrated a dose-dependent protection of the novel DPA compounds over 24 h. Compounds alone did not affect the cell index. Each curve contains different measurement point of n = 6 - 8 wells. All data are shown as mean +/- S.D. ###p < 0.001 compared to erastin treated control (ANOVA, Scheffé's test).

Moreover, the protective effect against RSL-3 was tested to exclude a direct interaction between the novel compounds and erastin that possibly led to the cell protection. Exposure to erastin and RSL-3 for 16 h resulted in massive cell death (Figure 40 A, Erastin; RSL-3). However, when cells were co-treated with 1 μ M of each DPA compound these lethal effects were markedly counteracted in both erastin and RSL-3 treated conditions (Figure 40 A DPA 1-3 + Era/ RSL-3). Additionally, the overall elongated and healthy morphology of the cells was maintained, which was similar to the medium-treated control (Figure 40 A).

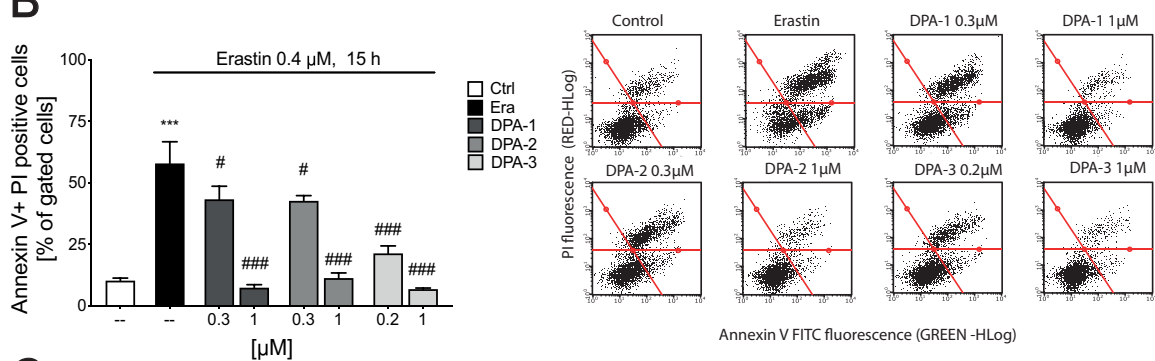
Correspondingly, cell death measurements using Annexin V/ PI staining were conducted to confirm this impression from the microscopic images in a quantitative manner. Subsequent FACS measurements revealed that when erastin and RSL-3 were treated together with the EC50 of the respective compounds, fewer cells showed green (Annexin V) or combined green and red (Annexin V + PI) fluorescence than cells solely treated with erastin and RSL-3 (Figure 40 B, C). Furthermore, when cells were treated with EC100 in co-treatment with erastin and RSL-3, ferroptotic cell death was completely inhibited (Figure 40 B, C).

Hence, the results indicate that the compounds were able to prevent ferroptotic cell death by interfering with the ferroptosis pathway and not by direct interaction with the ferroptosis-inducing molecule erastin.

A



B



C

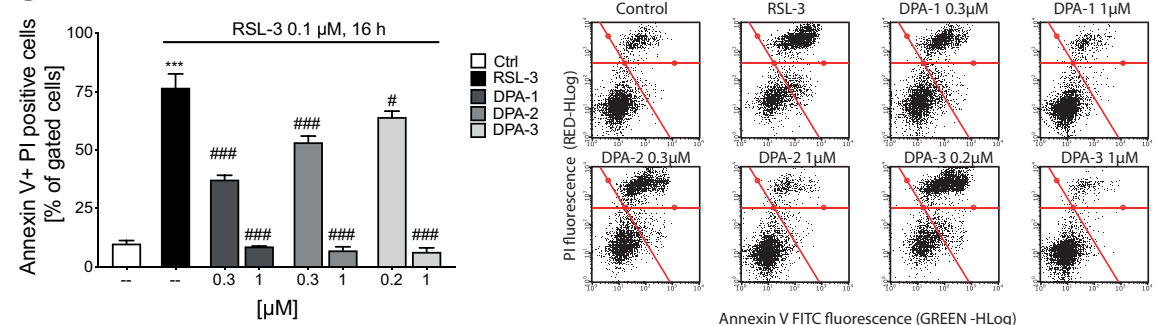


Figure 40. DPA compounds abrogated cell death upon different ferroptosis inducers in HT22 cells. **A)** Representative bright field image of HT22 cells (20x + 5x digital zoom for control and 3x digital zoom for other images) treated with either erastin (0.4 μ M) or RSL-3 (0.2 μ M) for 15 - 16 h in absence or presence of novel diphenylamine compounds (1 μ M) revealed pronounced protection against both ferroptosis inducers. Scale bars: 100 μ m. **B), C)** Cell death measurements using Annexin V/ PI staining unveiled a dose-dependent protection of cell demise upon erastin (0.4 μ M) **B)** and RSL-3 (0.1 μ M) **C)**. The quantification shows the summarized cell count of the lower right corner (representing Annexin V positive cells) and of the upper right corner (representing Annexin V + PI positive cells). **B), C)** Quantifications show representative results from n = 3; all experiments were repeated at least three times with similar outcomes; all data are shown as mean + S.D. ***p < 0.001 compared to untreated control; #p < 0.05, ##p < 0.01, ###p < 0.001 compared to erastin or RSL-3 treated control (ANOVA, Scheffé's test).

Next, it was tested whether the compounds were exclusively preventing ferroptotic cell death or if they could also block the caspase-dependent apoptotic cell death pathway induced by staurosporine. Prior to staurosporine treatment, the cells were pre-incubated with the novel compounds at the respective concentrations for 1 h. In addition to the DPA compounds, the scaffold molecule BI-6c9 and the broad-spectrum caspase inhibitor QVD, as a positive control, were also tested under these pre-treatment conditions. After the pre-incubation phase, the pre-treatment solutions were exchanged to the treatment solutions containing the different compounds in the presence of 1 μ M staurosporine and incubated for 17 h. Annexin V/ PI FACS analysis on the following day revealed that only the broad-spectrum caspase inhibitor QVD but neither the DPA compounds nor BI-6c9 were able to block staurosporine induces apoptosis. This result indicated that the novel DPA compounds specifically inhibited caspase-independent cell death pathways.

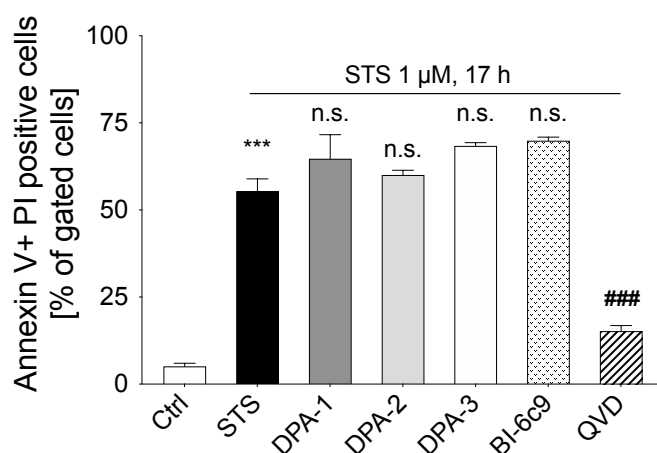


Figure 41. DPA compounds and BI-6c9 did not prevent apoptosis in HT22 cells upon staurosporine treatment. Cells were pre-incubated with diphenylamine compounds (1 μ M), BID inhibitor BI-6c9 (10 μ M) and QVD (10 μ M) for 1 h. Afterwards, cells were treated with staurosporine (STS) and staurosporine/ compound co-treatment solution for 17 h. Only the caspase inhibitor QVD prevented cell death in this apoptosis cell death paradigm. All data are shown as representative examples with mean + S.D. *** $p < 0.001$ compared to untreated control; ### $p < 0.001$ compared to STS treated control (ANOVA, Scheffé's test).

3.2.4. Investigations on potential neurotoxicity

In order to assess the neurotoxic potential of the novel compounds, HT22 cells were treated with DPA compounds in concentrations that were 10 – 100-fold higher than the concentrations needed for the maximal protective effect (1 μ M). As Figure 42 A) demonstrates, none of the compounds significantly altered cell viability tested in the MTT assay at these doses. Additionally, the toxic potential was tested via Annexin V/ PI staining, where none of the compounds did show increased cell death rates using the EC100 of 1 μ M for 15 h (Figure 42 B).

These results indicate that the novel compounds were well-tolerated at concentrations of 1 μ M and show no deleterious effects on neuronal cells even at further increasing concentrations up to 100 μ M.

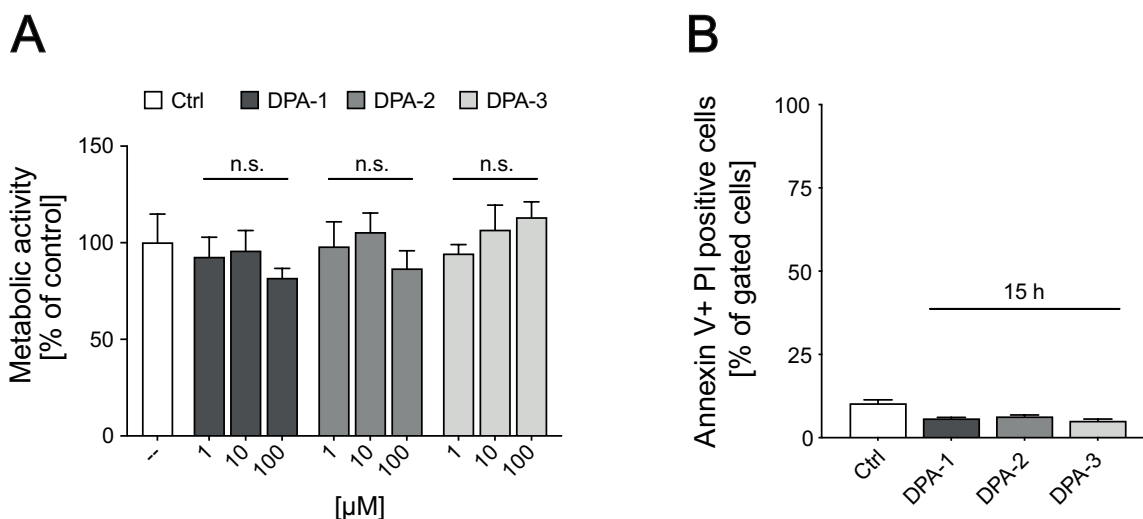


Figure 42. DPA compounds were well tolerated and showed no neurotoxic effects. A) Cell viability was not altered compared to control, when HT22 cells were treated with DPA compounds at concentrations of 1 – 100 μ M for 16 h ($n = 8$). **B)** AnV/PI cell death measurements demonstrated that the DPA compounds alone did not lead to increased cell death rates after 15 h of treatment in their respective EC100 of 1 μ M.

3.2.5. Major ROS dependent hallmarks of ferroptosis were effectively blocked by the novel compounds

The previous experiments were extended to determine whether the novel compounds affected different pivotal hallmarks of ferroptosis. As demonstrated in chapter 3.2.2., lipid peroxide levels, as the most conclusive hallmark of ferroptosis, as well as soluble, cytosolic ROS levels, were most significantly increased 6 – 8 h after ferroptosis induction. Hence, these ROS species were measured in this time frame. These detrimental processes were inhibited in a concentration-dependent manner by all novel DPA compounds (Figure 43 A, B).

Following soluble and lipid ROS formation, the cell death response was next transferred to mitochondria where mitochondrial ROS formation was triggered. Using the MitoSOX dye, mitochondrial superoxides were measured 15 h after ferroptosis induction. In line with the previous results, the DPA compounds only attenuated mitochondrial ROS formation at EC50, whereas superoxide formation in the mitochondria was fully suppressed at EC100 (Figure 43 C).

Moreover, to exclude adverse effects of the novel DPA compounds on the applied fluorescent dyes, the novel compounds were also tested without erastin. None of the novel compounds exhibited significantly changed fluorescence signals under basal conditions, suggesting that the DPA compounds neither altered basal levels of any of the detected ROS species nor interfered with any of the respective fluorescent dyes (Figure 43 D-F).

To validate that the suppression of the ferroptosis hallmarks by the DPA compounds was also applicable when ferroptosis was initiated by GPX-4 inhibition, the cells were treated at similar time points with 0.1 – 0.2 μM RSL-3, and the aforementioned hallmarks of ROS formation were re-determined. Indeed, all three ROS species were effectively blocked in a concentration dependent manner (Figure 43 G-I).

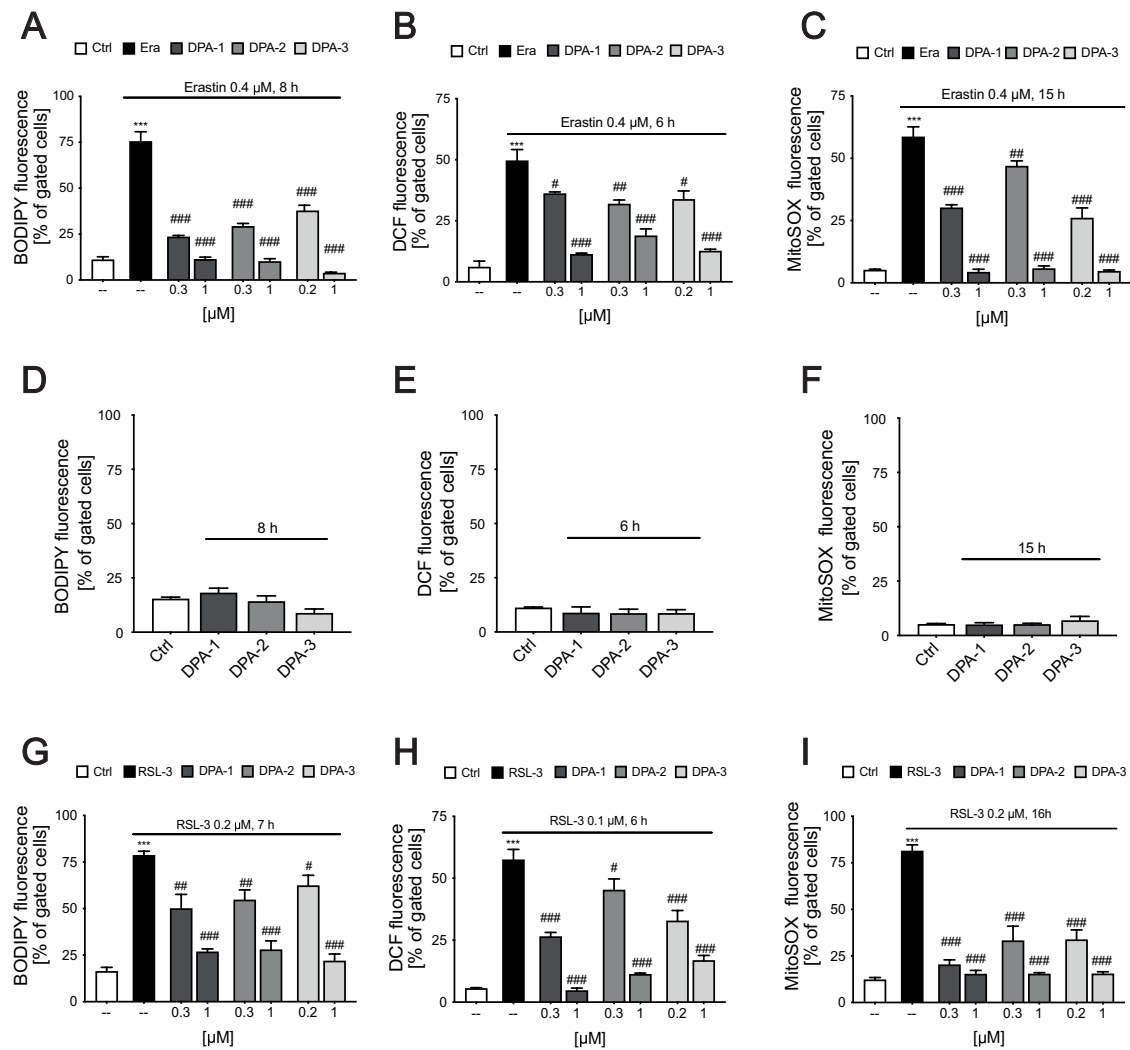


Figure 43. DPA compounds prevented lipid and soluble, cytosolic ROS as well as mitochondrial ROS formation without direct interaction with these dyes. HT22 cells were treated with erastin 0.4 μM (A-C) or RSL-3 (G-I) with or without co-treatment of the indicated concentrations of differing compounds. Additionally, cells were treated with 1 μM of the compounds without ferroptosis inducers for the indicated times (D-F). Following, cells were stained with BODIPY (A, D, G), DCF (B, E, H) or MitoSOX (C, F, I) and subjected to FACS analysis. Lipid peroxidation, soluble ROS formation and mitochondrial ROS formation were prevented in a dose-dependent manner according to the EC50 and EC100 concentration upon erastin (A-C) or RSL-3 (G-I) treatment. (D-F) Intrinsic effects of the DPA compounds (1 μM) on (D) BODIPY, (E) DCF and (F) MitoSOX staining were not found. In this figure representative results from $n = 3$ are presented; all experiments were repeated at least three times with similar outcomes; all data are shown as mean + S.D. *** $p < 0.001$ compared to untreated control; # $p < 0.05$, ## $p < 0.01$, ### $p < 0.001$ compared to erastin/RSL-3 treated control (ANOVA, Scheffé's test).

To investigate the DPA compound's potency to directly scavenge radicals, the established DPPH assay was conducted. All compounds were diluted to the respective EC100 concentrations in ethanol. The well-established radical scavenger Trolox served as a positive control and ethanol served as the vehicle control. Surprisingly, only Trolox, but none of the novel DPA compounds showed a radical scavenging effect in this assay (Figure 44 A).

For this reason, additional tests were carried out in an H₂O₂ model. H₂O₂, as one of the ROS species formed in HT22 cells during ferroptosis, can easily pass membranes and thereby directly alter ROS levels within the cell ¹⁶³. To initiate cell death, 0.7 mM H₂O₂ solution was applied to the HT22 cells for 16 h and DPA-compounds as well as Trolox were applied as co-treatment to the cells. Remarkably, all DPA compounds protected roughly 50% of the cells from H₂O₂ induced cell death (Figure 44 B). However, Trolox was even more effective in this cell death paradigm and entirely prevented the decrease of cell viability.

Furthermore, it was investigated whether the discrepancies in the protection ability of Trolox and the DPA compounds against H₂O₂-induced cell death were also visible in the DCF assay. For this experiment, HT22 cells were treated with 0.7 mM H₂O₂ for 6 h in the absence or presence of the different compounds. Only Trolox, but none of the DPA compounds, were able to reduce H₂O₂-induced ROS formation detected as DCF fluorescence (Figure 44 C).

These results indicated that the radical scavenging activity of the novel compounds was not as pronounced as for the radical scavenging Trolox. This fact suggests that the antioxidative effect attributed to the DPA structure contributed to the anti-ferroptosis behavior but is probably not solely responsible for the protective mechanism.

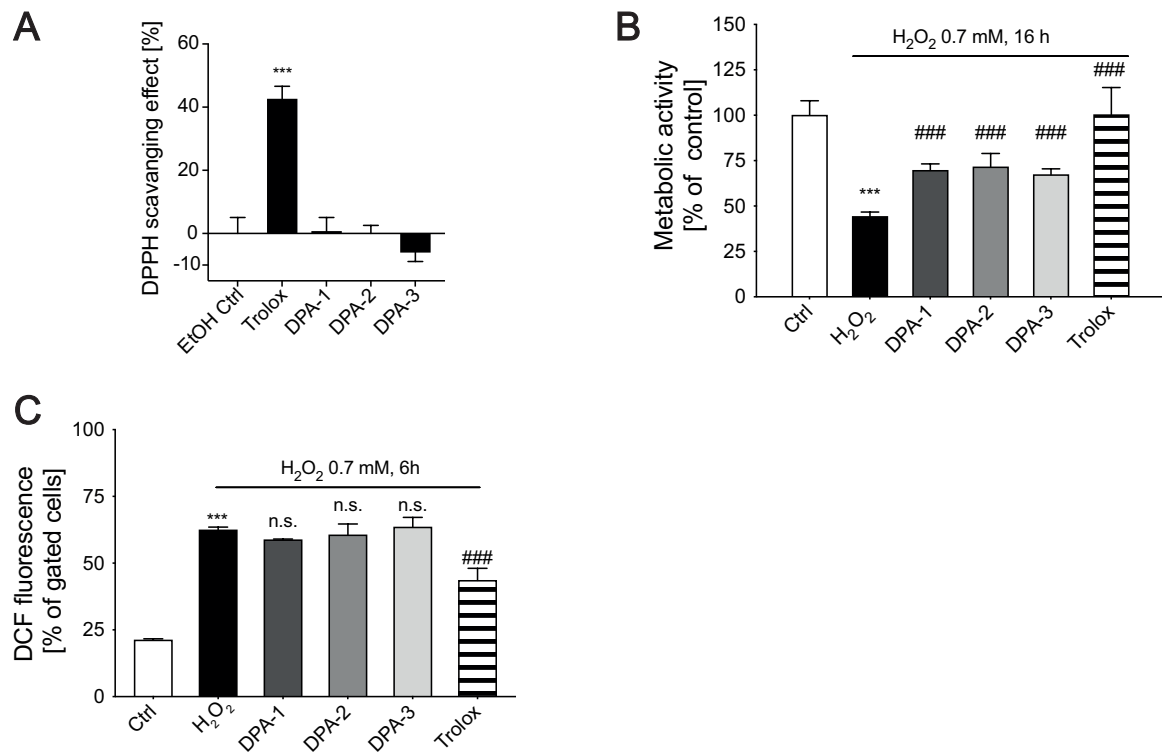


Figure 44. Novel compounds possessed only limited ROS scavenging activity. A) ROS scavenger Trolox (100 μ M), which served as a positive control, and DPA compounds (1 μ M) were diluted to the respective concentrations in ethanol and incubated with DPPH for 20 min. Ethanol alone served as a negative control and the ethanol effect was subtracted as background correction for all results ($n = 6$). **B-C)** For all experiments Trolox (100 μ M) and DPA compounds (1 μ M) were applied simultaneously to the respective treatments. **B)** DPA compounds only attenuated cell death induced upon 16 h of 0.7 mM H₂O₂ treatment, whereas Trolox completely protected the cells from H₂O₂ induced cell demise. **C)** Moreover, only Trolox was able to attenuate H₂O₂ induced cytosolic ROS formation detected as DCF fluorescence. **B, C)** show representative results from **B)** $n = 8$ and **C)** $n = 3$; **A-C)** all data are shown as mean + S.D. *** $p < 0.001$ compared to EtOH treated/untreated control, ### $p < 0.001$ compared to H₂O₂ treated control (ANOVA, Scheffé's test).

3.2.6. Upstream cascade of ferroptosis was not affected by DPA compounds

Next, the ability of the compounds to interfere with the upstream cascade of ferroptosis was examined, including glutathione levels and GPX4 regulation. Previous studies and results presented in this thesis showed that glutathione levels were depleted within the first 6 h after erastin treatment²⁷. In contrast, GSH levels were not altered by RSL-3 treatment since RSL-3 induces ferroptosis via direct GPX4 inhibition and subsequent downregulation of the protein^{2,35}. Therefore, glutathione levels were investigated 6 h after the respective treatments. The results clearly demonstrated that the DPA compounds neither affected glutathione levels under basal control conditions nor after RSL-3 treatment, nor did they prevent the decline of GSH levels during erastin-mediated ferroptosis (Figure 45).

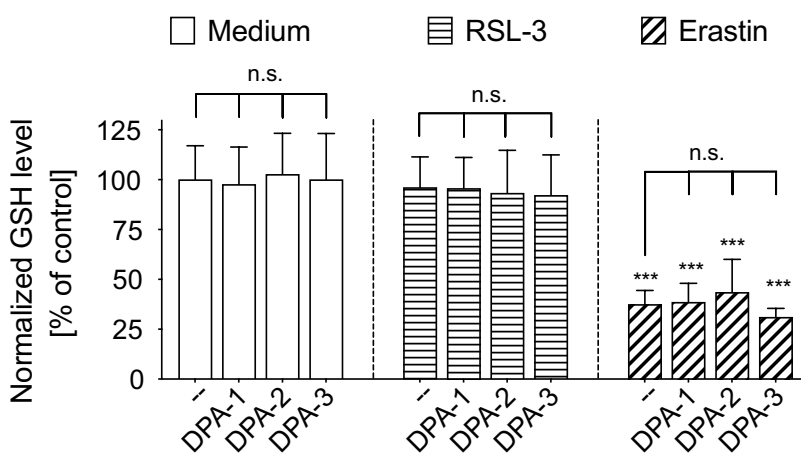


Figure 45. Novel DPA compounds did not affect glutathione levels. DPA compounds (1 μ M) were treated in absence or presence of erastin (1 μ M) and RSL-3 (1 μ M) for 6 h ($n = 5$) before HT22 cells were harvested and glutathione assay was performed. All data are shown as mean + S.D. *** $p < 0.001$ compared to untreated control. (ANOVA, Scheffé's test).

Using Western blot analysis of GPX4 levels, it was further investigated whether the novel compounds affected GPX4 expression. After sixteen hours of DPA compound treatments in absence of ferroptosis inducers, no alterations in GPX4 levels were detectable (Figure 46 A), as also demonstrated in the quantification (Figure 46 C). However, the representative Western blot result as well as the quantification of the GPX4 protein expression after 4 h of RSL-3 treatment clearly showed that GPX4 levels were already significantly decreased compared to control (Figure 46 B). This depletion of GPX4 protein could not be prevented by any of the DPA compounds (Figure 46 B, D).

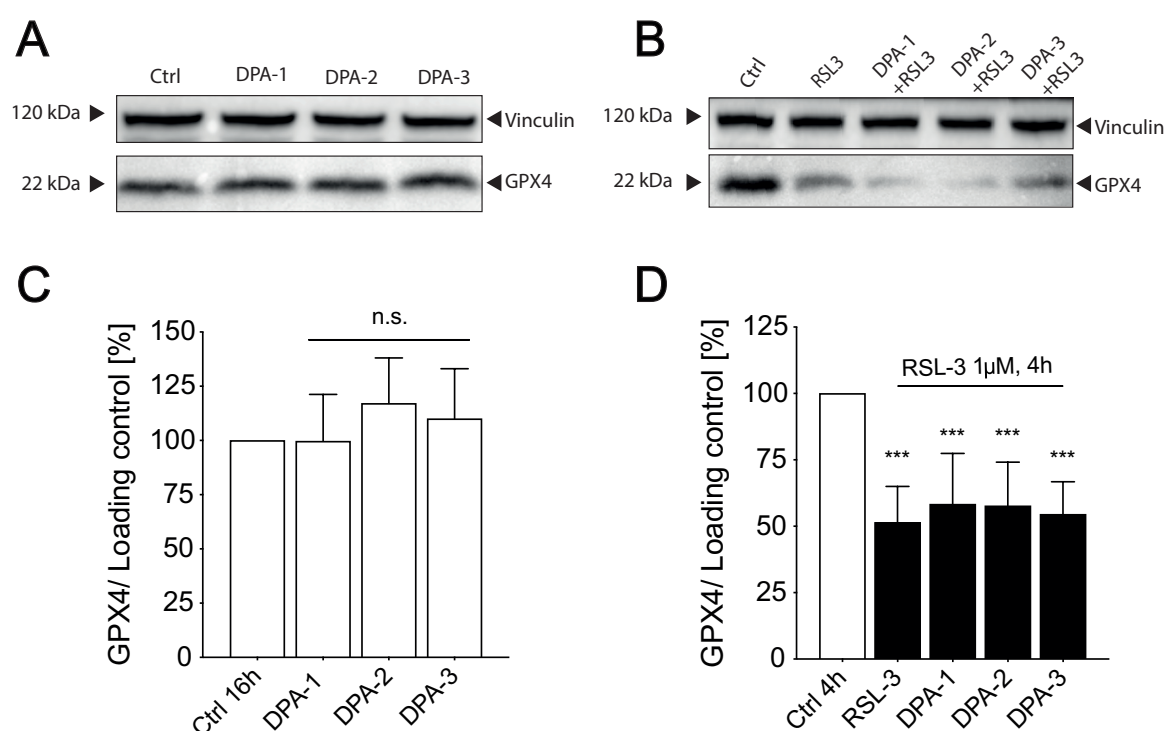


Figure 46. GPX4 levels were not affected by the novel compounds. **A, B)** Representative Western blots of GPX4 levels and vinculin as loading control after 16 h of DPA treatment alone **A)** or after a 4 h-co-treatment of the DPA compounds with RSL-3 (1 µM) **B)**. **C)** Quantification of n = 4 Western blot results from DPA treatments alone for 16 h or **D)** quantification of n = 5 Western blot results from DPA RSL-3 co-treatment for 4 h. **C, D)** All data are shown as mean + S.D. ***p < 0.001 compared to untreated control (ANOVA, Scheffé's test).

These results indicate that the novel compounds inhibit ferroptosis without affecting the detrimental effects upstream of ROS development like GSH depletion or GPX4 downregulation after ferroptosis induction.

3.2.7. DPA compounds preserved mitochondrial membrane potential and morphology

As previously reported (chapter 3.2.2), upstream effects of ferroptosis such as lipid and cytosolic ROS formation lead to mitochondrial impairments in the proceeding ferroptosis cascade. This results in fragmented mitochondrial morphology in combination with impaired mitochondrial function and a loss of mitochondrial membrane potential.

Hence, the novel compounds were tested for their ability to prevent these mitochondrial impairments. First, mitochondrial morphology was determined by fluorescence microscopic analysis after 10 h of erastin treatment. Ferroptosis induction caused a significant change from elongated mitochondria, which were distributed throughout the whole cell (referred to as category I) (Figure 47 Control) to fragmented mitochondria, which were located around the nucleus (referred to as category III) (Figure 47 A Erastin). All three compounds led to a fully preserved mitochondrial morphology when treated together with erastin for 10 h (Figure 47 A DPA 1-3 + Era). To quantify this observation, mitochondrial morphology of three independent experiments of at least 500 cells per condition were classified in accordance with the rating system and afterwards pooled for statistical analysis. As expected, the erastin conditions with DPA compound co-treatment showed a significant reduction in mitochondria classified as category III compared to erastin treatment alone (Figure 47 B).

Next, the capabilities of the compounds to protect mitochondria were studied at a functional level. Mitochondrial membrane potential was analyzed using TMRE FACS after erastin treatment or combined erastin and DPA compound treatment for 15 h (Figure 47 C). In this time scale, erastin treatment strongly decreased mitochondrial membrane potential. The decrease was abrogated in a dose-dependent manner by the DPA compounds with respect to the EC50 and EC100 (Figure 47 C). Similar results were observed when the cells were exposed to RSL-3. Although no significant protection was achieved at the EC50 concentration, there is still a clear tendency towards an increased mitochondrial membrane potential, which was fully restored at EC100 of the DPA compounds (Figure 47 D).

Moreover, when the DPA compounds (1 μM) were applied without additional treatment with a ferroptosis inducer for 15 h, no changes in the TMRE fluorescence with respect to the control were detected (Figure 47 E).

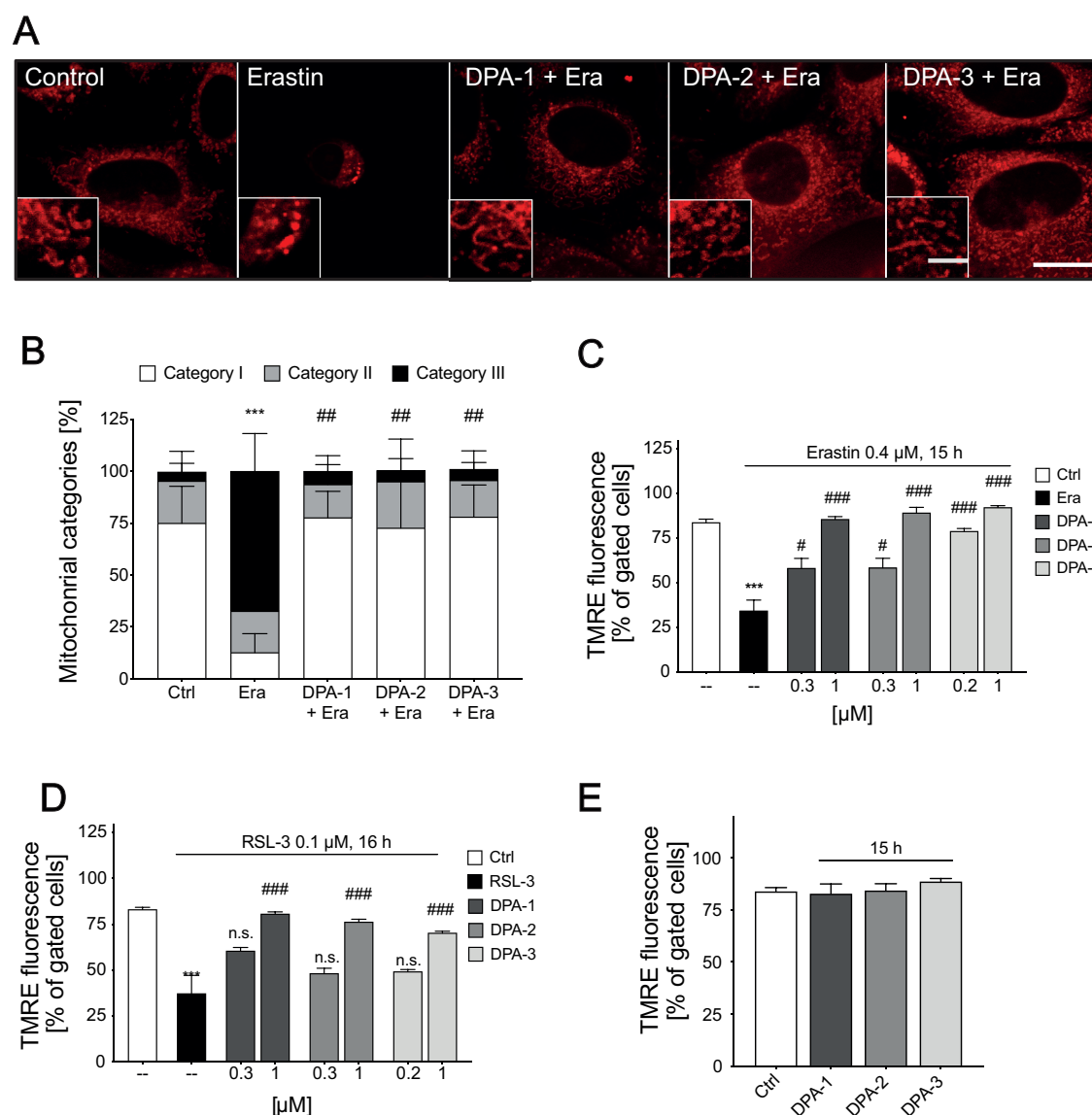


Figure 47. Compounds preserved mitochondrial morphology and mitochondrial membrane potential. A) Representative images (63 x oil-objective) of mitochondria after 10 h of erastin treatment (erastin) (0.4 μM) or medium control (control). DPA compounds (1 μM) were applied as co-treatment. Cells were stained with MitoTracker DeepRed (0.2 μM) before being fixed using 4 % PFA solution. Scale bar: overview: 20 μm , zoom: 5 μm . **B)** Categorization of mitochondria was performed in accordance with the protocol detailed in methods. For quantification, at least $n = 500$ cells per condition of three independent experiments were taken into consideration and thereby a strong preservation of mitochondrial morphology was revealed. *** $p < 0.001$ of cells classified as category III compared to untreated control; ## $p < 0.01$ of cells classified as category III compared to erastin treated control (ANOVA, Scheffé's test). **C-E)** Representative results ($n = 3$) of mitochondrial membrane potential analysis after erastin (0.4 μM , 15 h **C**) or RSL-3 (0.1 μM , 16 h **D**) treatment or without ferroptosis inducing agent **E**). **C-E)** All data are shown as mean + S.D. *** $p < 0.001$ compared to untreated control; # $p < 0.05$, ### $p < 0.001$ compared to erastin/ RSL-3 treated control (ANOVA, Scheffé's test).

3.2.8. DPA compounds maintain mitochondrial respiration and function

To investigate whether the DPA compounds affect mitochondrial bioenergetics, the Seahorse system was utilized for the analysis of important respiration parameters such as the oxygen consumption rate (OCR) which is an indicator for energy supply through oxidative phosphorylation in mitochondria, as well as the extracellular acidification rate (ECAR) as an indicator for energy supply based on glycolysis. When HT22 cells were treated with 0.15 μ M erastin over 15 – 16 h, a striking drop in basal OCR and ECAR was observed (Figure 48 B, D). Additionally, erastin treatment caused a remarkable reduction in the capacity for maximal respiration induced by the administration of the protonophore FCCP (Figure 48 B). When the DPA compounds were applied without additional erastin treatment, basal respiration seemed to be slightly increased above control levels (Figure 48 A), although the statistical analysis of three independent experiments revealed that this effect was not significant for any of the compounds (Figure 48 E). DPA compound-erastin co-treatment provided a complete maintenance of the basal respiration (Figure 48 B) which was substantiated in the quantification of the pooled results (Figure 48 E). Moreover, the statistical analysis further demonstrated no intrinsic effects on FCCP stimulated maximal respiration, when the compounds were applied in absence of erastin (Figure 48 A, F), but a totally preserved maximal respiration when applied together with erastin (Figure 48 B, F). The analysis of mitochondrial independent energy metabolism revealed that basal glycolytic activity was not affected when DPA compounds were applied at concentrations of 1 μ M without additional erastin treatment (Figure 48 C). However, the detrimental effects of erastin on glycolysis were completely blocked by co-treatment with the DPA compounds (Figure 48 D).

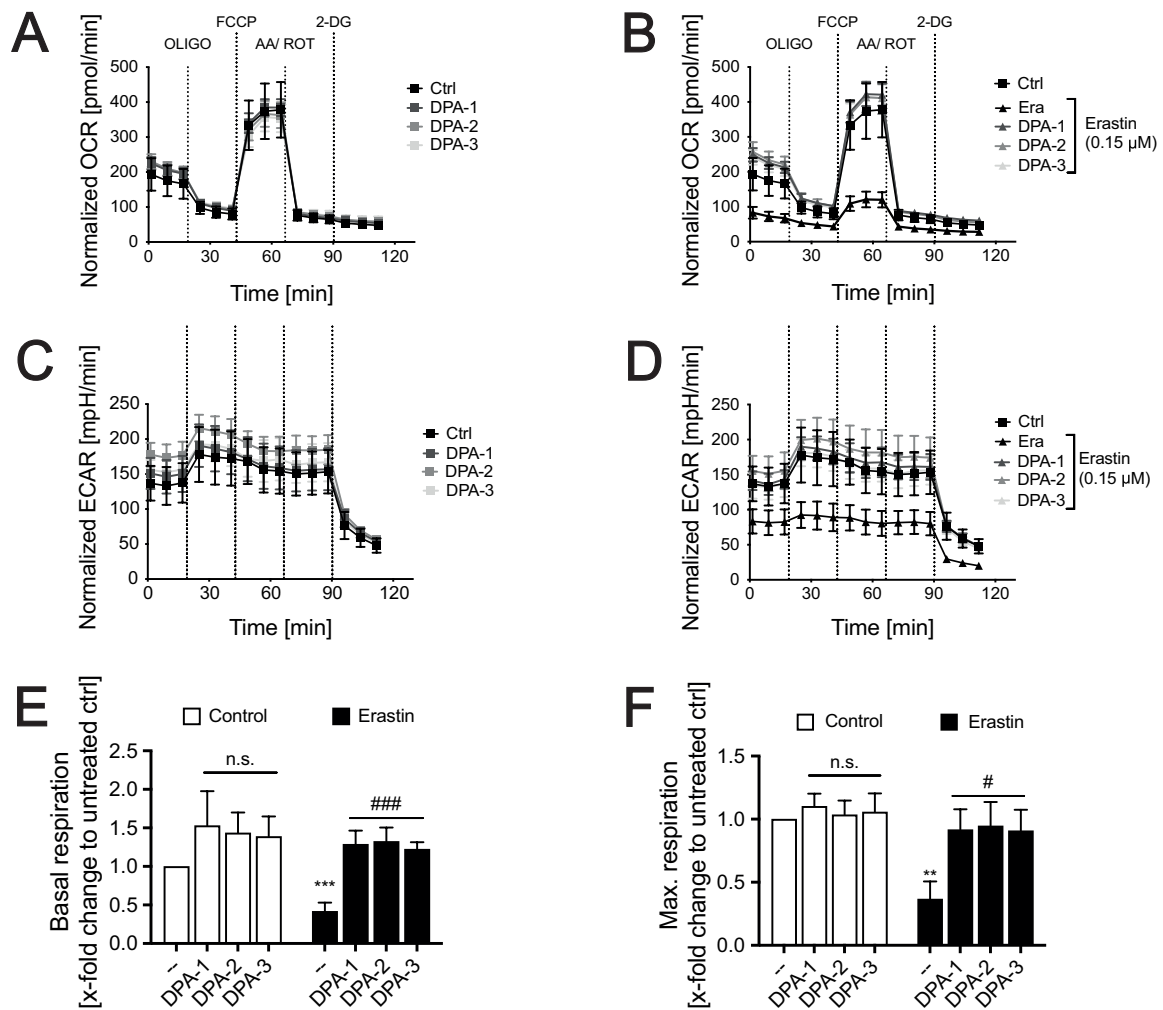


Figure 48. Novel compounds maintained mitochondrial respiratory function upon erastin treatment. **A-D)** Representative results from Seahorse measurements after 16 h of respective treatments ($n = 6 - 8$ / condition). Plots show the effects of $1 \mu\text{M}$ compound treatment on oxygen consumption rate (OCR) and extracellular acidification rate (ECAR) after 16 h incubation without erastin treatment **A), C)** or in combined treatment with $0.15 \mu\text{M}$ erastin **B), D)**. 16 h of erastin treatment resulted in strong decrease in OCR **B)** and ECAR **D)** which was completely prevented by the compounds. **E), F)** Quantification of basal respiration (before oligomycin injection) **E)** and maximal respiration (after FCCP injection) **F)** of three independent experiments. DPA compounds led to slight, but not significant rise of basal respiration (**white columns E)**) and no alterations in the maximal respiration (**white columns F)**) in absence of erastin. In presence of erastin, both basal and maximal respiration were fully restored to control levels (**black columns E) and F)**). All data are shown as mean + S.D. or +/- S.D. ** $p < 0.01$, *** $p < 0.001$ compared to untreated control; # $p < 0.05$, ### $p < 0.001$ compared to respective erastin treated control (ANOVA, Scheffé's test).

Furthermore, ATP levels of the cells were measured to investigate an additional parameter for mitochondrial function. Sixteen hours of erastin treatment caused an intense decline in ATP levels due to marked mitochondrial damage which could be prevented by the compounds in a dose-dependent manner (Figure 49).

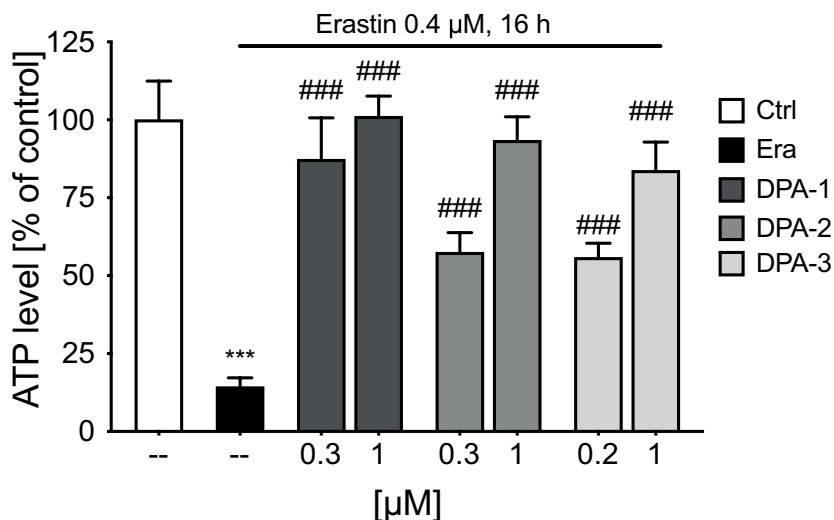


Figure 49. ATP levels were maintained by the novel DPA compounds. ATP levels were investigated via ATP luminescence assay 16 h after erastin treatment. Novel diphenylamine compounds maintain ATP levels in accordance with their EC50 and EC100 (n=8). Data are shown as mean + S.D. ***p < 0.001 compared to untreated control; ###p < 0.001 compared to respective erastin treated control (ANOVA, Scheffé's test).

The results imply that the novel DPA compounds were very effective in maintaining mitochondrial integrity and function against ferroptotic demise, thereby providing a significant contribution to cell survival.

3.2.9. Confirmation of the results in mouse hypothalamus (mHypo) cells

To exclude a cell line specific protection of the DPA compounds in HT22 cells, the findings obtained so far were confirmed in the mouse hypothalamus (mHypo) cell line. Previous studies demonstrated that these cells were responsive to the ferroptosis cell death stimulus erastin¹⁶⁴. The mHypo cells were treated with 1 µM of erastin in co-treatment with the respective doses of the DPA compounds for 16 h. Immediately before the MTT assay was performed, cell morphology was evaluated under the microscope.

As expected, 1 μM of erastin resulted in severe demise of the mHypo cells (Figure 50 A Erastin). When EC50 concentrations of the DPA compounds were applied, much more viable cells were detected, whereas EC100 concentrations totally abolished cell death (Figure 50 A DPA 1-3 + Era). This impression was also quantified via MTT and Annexin V/ PI measurements, drawing a similar picture as what was expected from the microscopic images. In both assays, EC50 concentrations attenuated the detrimental effect of the erastin treatment, whereas EC100 concentrations provided complete protection (Figure 50 B, C).

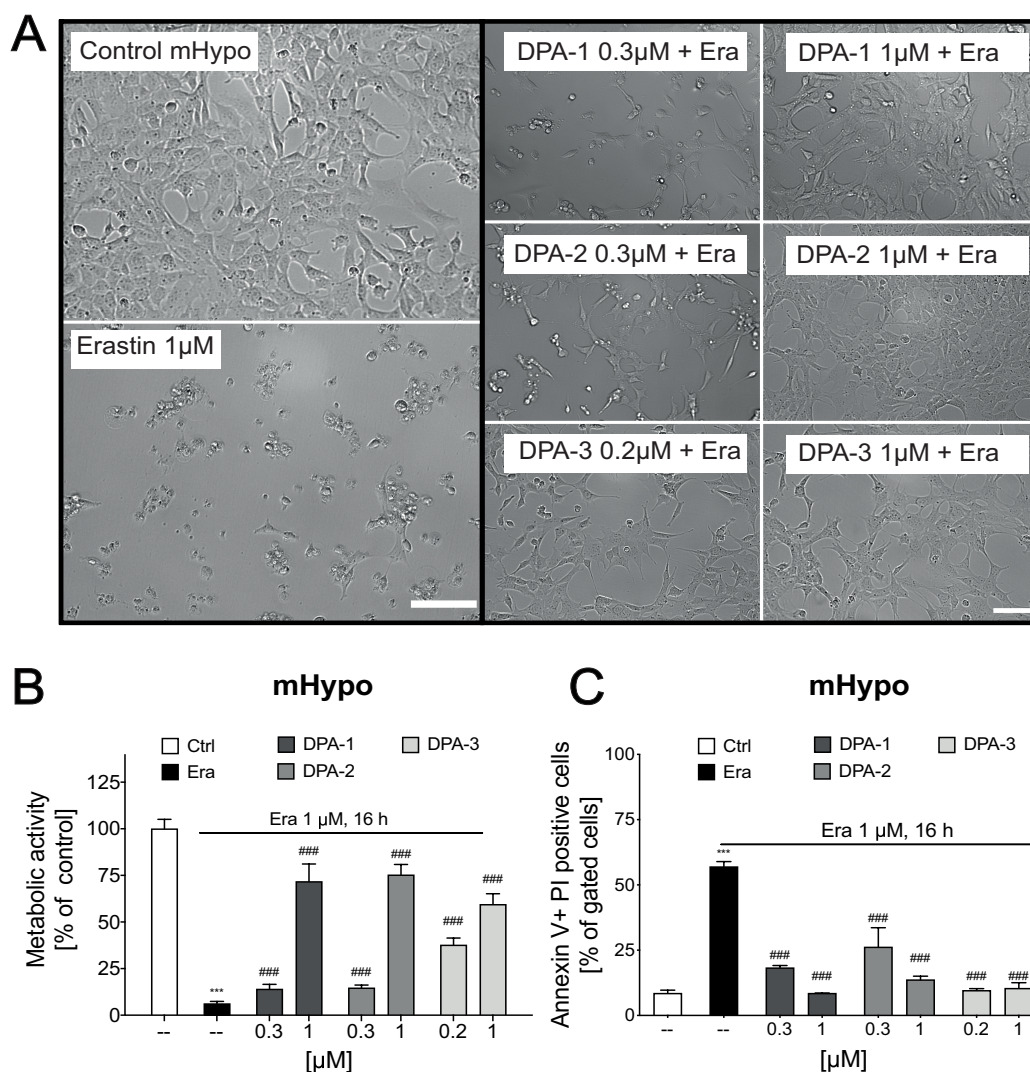


Figure 50. mHypo cells were protected against ferroptosis by the DPA compounds. A) Representative bright field images of mHypo cells (10x magnification) treated with erastin (1 μM , 16h) in absence or presence of EC50 and EC100 of the novel compounds, respectively (Scale bars 100 μm). Cell viability **B)** and cell death **C)** measurements revealed a dose-dependent protection for all DPA compounds against ferroptotic cell demise in the neuronal mHypo cells. **B), C)** show representative results from $n = 3$; all data are shown as mean + S.D. *** $p < 0.001$ compared to untreated control, #### $p < 0.001$ compared to erastin treated control (ANOVA, Scheffé's test).

In addition, it was investigated whether the DPA compounds exhibited similar activity against the development of the key ferroptosis parameters such as lipid peroxidation, mitochondrial ROS formation, and loss of mitochondrial membrane potential in the mHypo cells as what has been shown in the HT22 cells. These hallmarks were analyzed as endpoint measurements after 18 h of erastin compound co-treatment. mHypo cells responded to erastin treatment similarly to HT22 cells with elevated lipid peroxide production and mitochondrial ROS formation in combination with a decrease in mitochondrial membrane potential. As suggested 1 μ M of DPA compounds application completely abolished all these deleterious effects in the mHypo cells.

These results imply that the novel compounds prevent ferroptotic cell death independent of the used neuronal cell line by the same mechanisms previously investigated in the HT22 cells.

mHypo cells

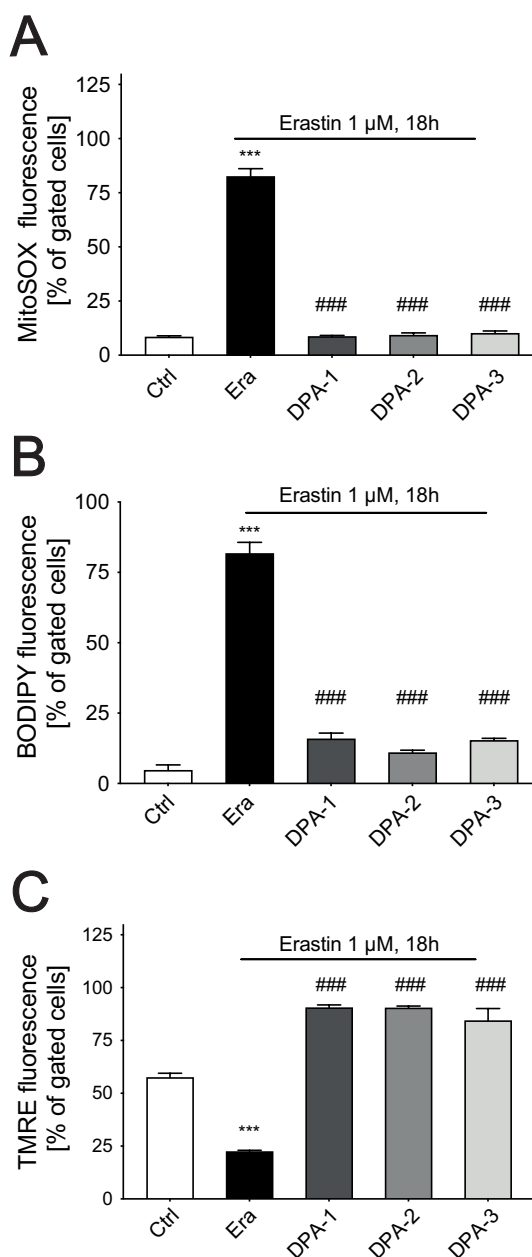


Figure 51. Novel compounds prevented the development of major ferroptosis hallmarks in mHypo cells. 24 h in advance to the treatments, 40 K mHypo cells were seeded in 24-well plates. Co-treatments of erastin (1 μ M) with the different DPA compounds (1 μ M) for 18 h protected the cells from development of major ferroptosis hallmarks like lipid peroxidation **A**), mitochondrial ROS formation **B**), and the loss of mitochondrial membrane potential **C**). **A-C**) show representative results from $n = 3$; all data are shown as mean + S.D., *** $p < 0.001$ compared to untreated control, ### $p < 0.001$ compared to erastin treated control (ANOVA, Scheffé's test).

3.2.10. Post-treatment time windows after ferroptosis induction

In order to determine an effective time window, in which the compounds could be applied to effectively inhibit cell death and prevent the development of the hallmarks of ferroptosis, post-treatment experiments were conducted in HT22 cells. For these experiments, ferroptosis was initiated by erastin treatment prior to DPA compound application. At the indicated post-treatment time points, erastin solution was exchanged with an erastin solution containing the novel compounds. Afterwards, the cells were further incubated to a total incubation time of 24 h.

First, the duration of time the compounds could prevent ferroptotic cell death was evaluated using MTT assays as well as Annexin V/ PI measurements. Both experimental settings clearly demonstrated that when DPA compounds were added within the first 4 – 6 h after initial erastin treatment, a vast majority of the HT22 cells were rescued (Figure 52 A, B). This dramatically changed at the 8 h time point, where DPA compound application only could prevent a small proportion of cells from cell death. Finally, when DPA compounds were added after 10 h of ferroptosis initiation, cell demise could not be canceled anymore.

In line with these results, lipid peroxidation as well as cytosolic and mitochondrial ROS formation was prevented up to 6 h after ferroptosis induction (Figure 52 C - E), whereas mitochondrial membrane potential was still largely maintained when DPA compounds were applied 8 h after erastin challenge (Figure 52 F).

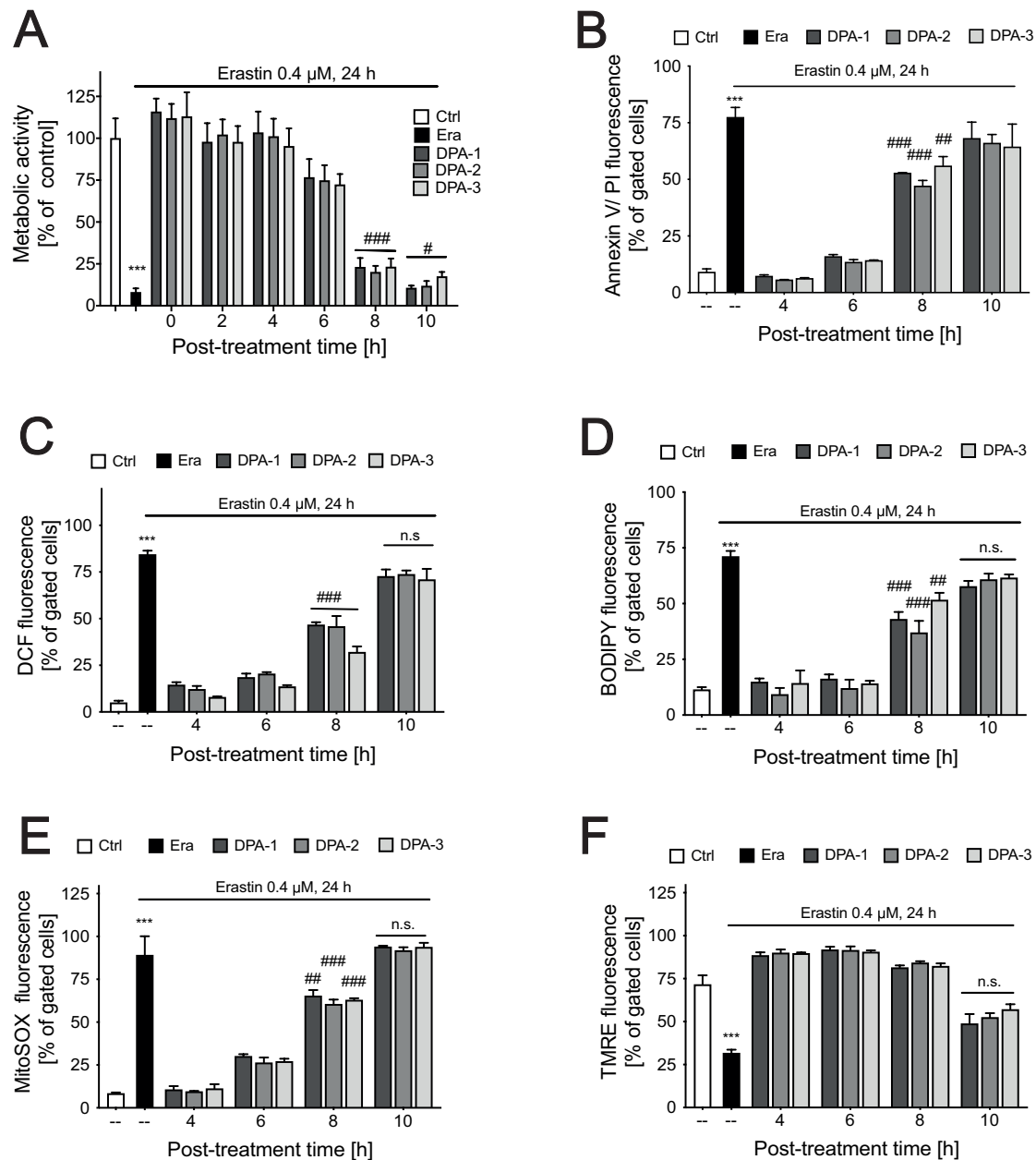


Figure 52. Cell death and formation of different ROS species could be blocked up to 6 h and loss of mitochondrial membrane potential could be prevented up to 8 h after ferroptosis induction. A - F) Ferroptosis was induced 0 – 10 h in advance to novel compound application (1 μ M). After the last DPA compound treatment, cells were incubated to a total treatment time of 24 h. **A, B) Compounds largely preserved cell viability measured via MTT **A)** and Annexin V/PI **B)** assay when applied no later than 6 h after initial erastin treatment. **C - E)** Cytosolic **C)**, lipid **D)**, and mitochondrial **E)** ROS formation were also widely abolished until 6 h of previous ferroptosis initiation. Interestingly, loss of mitochondrial membrane potential **F)** was largely blocked until 8 h after first erastin exposure. All data are shown as representative examples with mean + S.D. of n = 3, all experiments were repeated in similar ways at least three times with similar outcomes. ***p < 0.001 compared to untreated control; #p < 0.05, ###p < 0.01, ####p < 0.001 compared to erastin treated control (ANOVA, Scheffé's test).**

3.2.1. Approaches to investigate BID as a target structure for the novel DPA compounds

Since it may be obvious that the derivatives of the BID inhibitor BI-6c9 were also able to inhibit the same target structure, different assays were conducted to test this hypothesis, including the already established t-Bid overexpression which was also used before to validate the former BID inhibitors^{29,145,146}. Furthermore, the binding of the DPA compounds to the Bid3CCSS protein, introduced in the first part of this thesis, was investigated using microscale thermophoresis (MST), a NMR-based method, as well as co-crystallization and soaking experiments.

3.2.1.1. t-BID overexpression assay

The t-BID overexpression assay was performed using the established pIRES-t-Bid construct. Unfortunately, pIRES-t-Bid induced cell death could not be prevented by the novel DPA compounds. Notably, also BI-6c9 as a positive control failed to show a reliable and pronounced protection from t-BID induced toxicity (Figure 53). Hence, in this study the pIRES-t-Bid overexpression assay was not sufficient to finally clarify whether BID inhibition contributed to the protective mechanism.

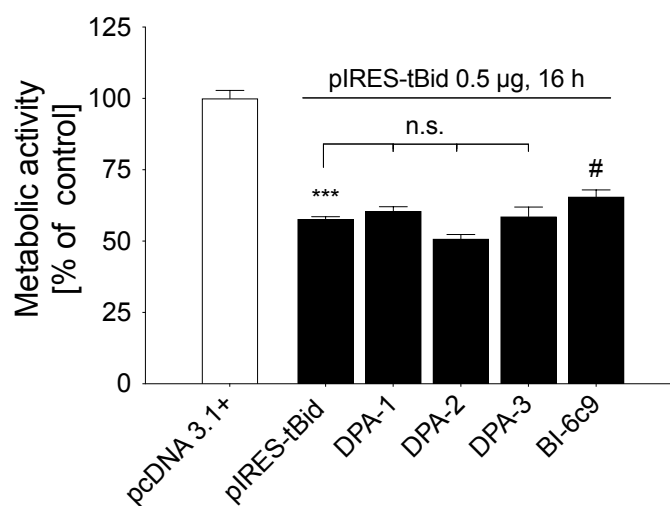


Figure 53. DPA compounds did not prevent pIRES-t-Bid induced cell death. HT22 cells were transfected with pIRES-t-Bid vector (0.5 µg) or pcDNA 3.1 + vector (0.5 µg) as control for 16 h. Only co-treatment using BI-6c9 (10 µM) slightly prevented pIRES-t-Bid induced cell death. Diphenylamine compounds (1µM) did not rescue the cells from decreased cell viability. All data are shown as representative examples with mean + S.D. ***p < 0.001 compared to untreated control, #p < 0.05 compared to pIRES-t-Bid control.

3.2.1.2. Investigations of DPA compound-BID binding using the Bid3CCSS construct

Microscale thermophoresis (MST)

The principle of MST measurements is based on the fact that the binding of a compound to a previously labeled protein causes an alteration in the diffusion kinetics of the protein in a temperature gradient (thermophoresis), which could be detected as changes of the fluorescence count in the heated area in the MST assay.

Therefore, initial labeling and ligand-interaction tests had to be performed with the Bid3CCSS construct. Therefore, the protein was diluted in labeling buffer and labeled with a RED-NHS 2nd generation dye that forms covalent bonds to lysine residues. Subsequently, the labeled protein was measured in dilutions of 1:1, 1:5, and 1:10 with PBS to determine the right concentration for the most suitable fluorescence intensity. Moreover, it was checked whether adhesion effects occur within the capillary that would compromise the measurement. The capillary scan demonstrated that Bid3CCSS could be sufficiently labeled. The dilution of 1:5 reached the most ideal fluorescence count of ~500 (Target range: 300 - 1000) (Figure 54). The peaks were well-shaped which indicates that adhesion of the protein to the capillary wall seemed to be minimal under these conditions.

All in all, these results showed that the Bid3CCSS protein is suitable for MST measurements, thus binding experiments were performed under similar conditions.

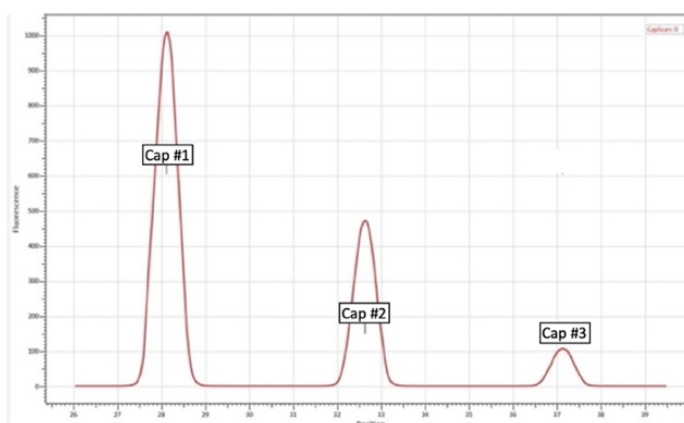


Figure 54. Capillary scan to determine the fluorescence intensity in different Bid3CCSS dilutions. The figure shows unprocessed data of the capillary scan (Laser: 20/ Led: 40) of 4.5 μM Bid3CCSS which was labeled with three-fold excess of fluorescence dye and thereafter diluted with PBS in the following ratios: Cap #1: 1:1; Cap #2: 1:5; Cap #3: 1:10. Peaks show a clear shape and a concentration-dependent decrease in fluorescence intensity with increasing dilutions.

Having established the labeling protocol for Bid3CCSS, BI-6c9 and the novel DPA compounds were measured at a final concentration of 1 mM (10 % DMSO) and 10 % DMSO as a negative control in a preliminary experiment. Interestingly, capillary scan results demonstrated that the DPA-2 compound interferes with the fluorescence signal. A minor perturbation of the fluorescence was also observed with the DPA-3 compound, while BI-6c9 and DPA-1 did not change the fluorescence intensity compared to DMSO control in this assay (Figure 55 A). The MST measurement curve of the 10 % DMSO negative control was well-shaped indicating that this DMSO concentration was well-tolerated by the Bid3CCSS protein. When a binding event of the compound to the Bid3CCSS protein occurs, an upward or downward shift of the curve is expected due to an altered diffusion behavior of the Bid3CCSS- compound complex in solution. All compounds showed a switched curve in comparison to DMSO control. BI-6c9 and DPA-3 showed a slightly shifted curve, whereas the signal shift for DPA-1 as well as DPA-2 was very striking. That could indicate for a binding event, although at least the strong shift for DPA-2 compound may be due to the fluorescence interfering activity.

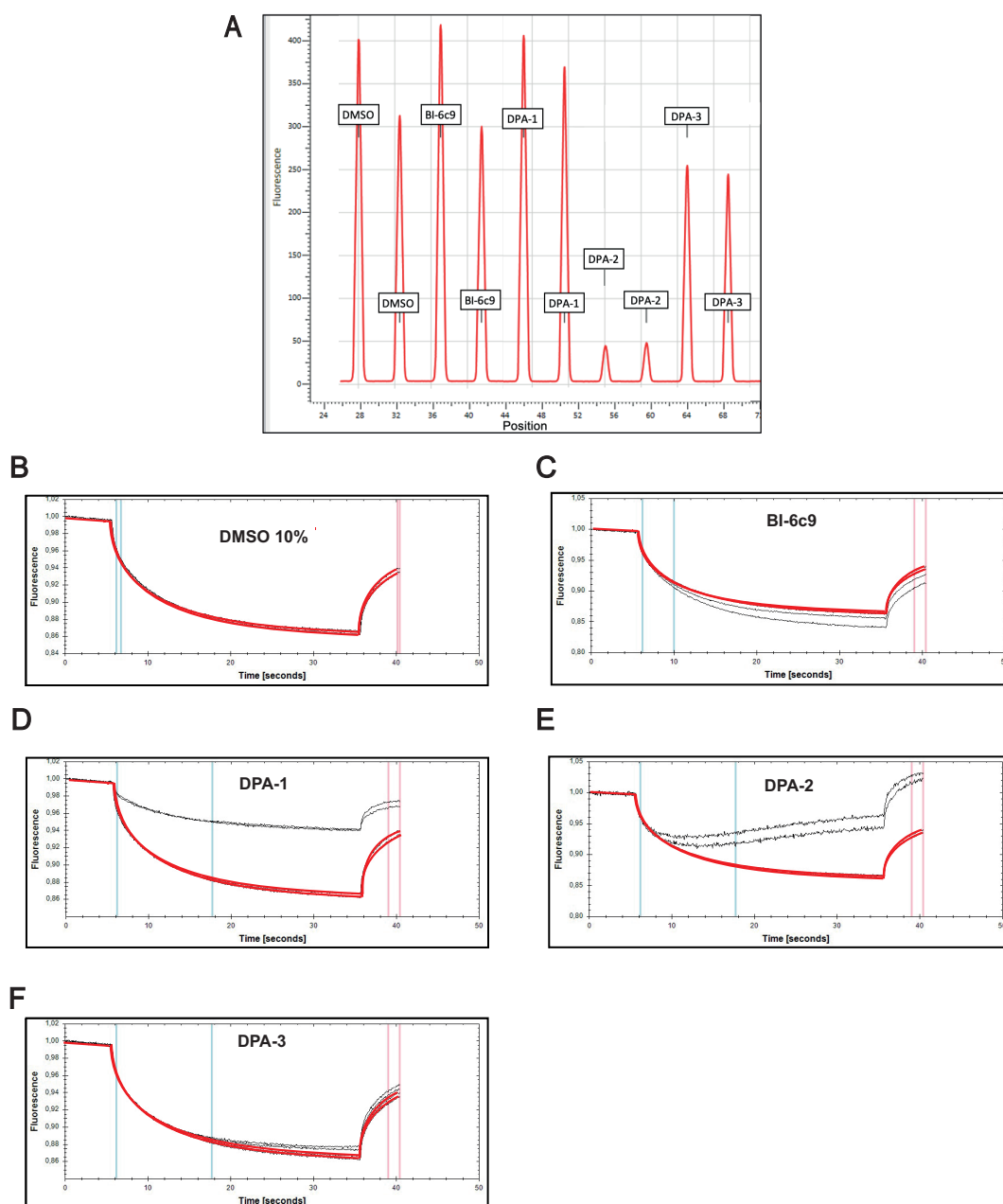


Figure 55. Preliminary results of MST measurements. MST measurements were conducted using 1 mM of the respective compounds in 10 % DMSO or 10 % DMSO alone, serving as control (**red curves**). The labeled Bid3CCSS protein was added in a ratio of 1:5. The measurements were performed in doublets. **A)** Capillary scan revealed a striking interference of the DPA-2 compound and to a less extent DPA-3 compound with the fluorescence. **B-F)** MST measurements of the individual compounds (**black curves**) in comparison to DMSO control (**red curves**).

Investigation of Bid3CCSS-compound interaction using NMR

In addition to the MST assay, a NMR-based approach was exploited to analyze the binding of the compounds to the Bid3CCSS protein. When a ligand binds to a certain protein this results in a signal shift in the NMR spectrum. The selected assay conditions contained very little protein concentration (5 μ M) and a great excess of ligand (100 mM).

The wide peak in the high-field at around 1 ppm in the red curve (compounds + Bid3CCSS) which is missing in the blue curve (compounds alone) showed that the Bid3CCSS protein is clearly visible in all samples (Figure 56). These characteristic wide peaks resulted from overlapping NMR signals of various alkyl groups within the protein. Thus, the Bid3CCSS construct is in principle measurable in this NMR assay under the applied conditions. However, BI-6c9 as well as DPA-3 were barely soluble at the applied concentrations (100 mM, 5% D₆-DMSO) leading to poor NMR signals and poor signal-to-noise ratios, although 512 scans were conducted (Figure 56 blue curve BI-6c9, DPA-3). Interestingly, when the compounds were measured together with the Bid3CCSS protein, the solubility of the compounds was increased, as reflected, for example, in the more intense aromatic signals in the low-field at approximately 7 ppm (Figure 56 red curve BI-6c9, DPA-3). The signal intensity was considerably enhanced for the charged compounds DPA-1 and DPA-2 due to the better solvent properties. Unfortunately, when the signals of the compounds alone were compared to the signals of the compounds that were measured in the presence of Bid3CCSS protein, no signal shifts were detectable for any of the compounds (Figure 56 red area) indicating that at least under the applied conditions no binding of any of the compounds could be confirmed so far.

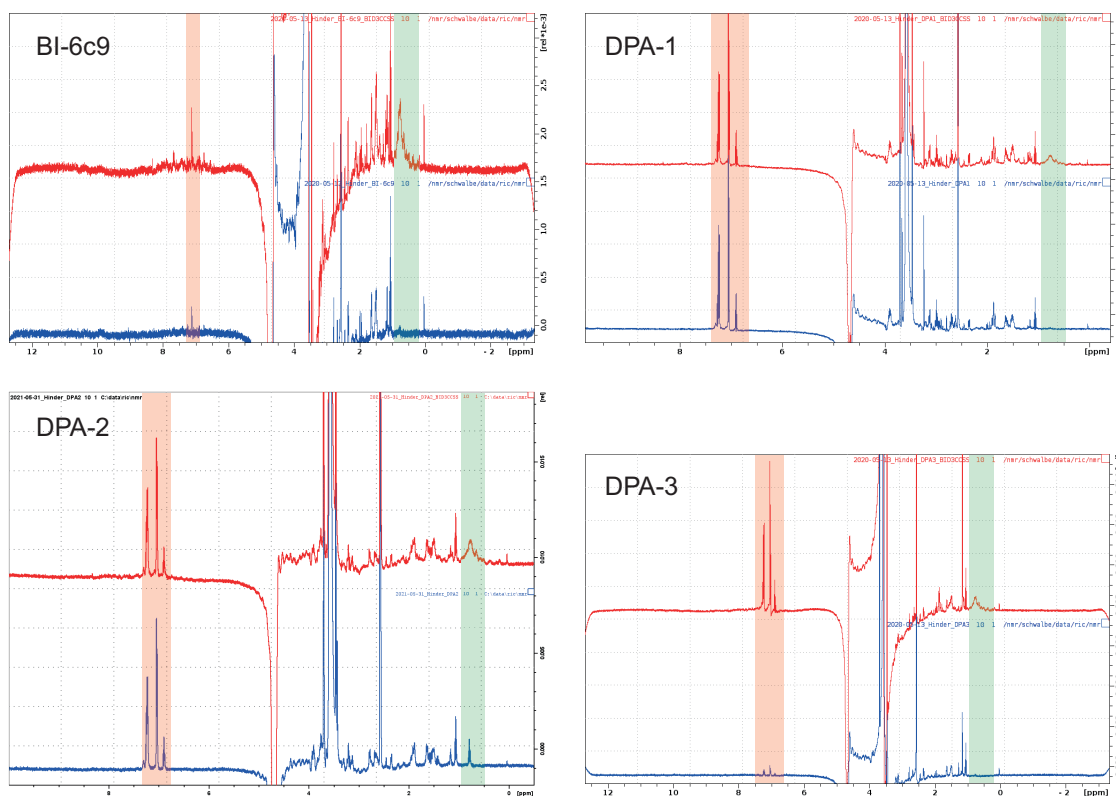


Figure 56. Ligand-based NMR measurements of BI-6c9 and the novel DPA compounds with Bid3CCSS. For ligand-based-NMR measurements all compounds were dissolved to a final concentration of 100 μM (5 % D6-DMSO in gel filtration buffer) in presence or absence of 5 μM Bid3CCSS protein. **Blue curves:** NMR spectra of the compounds alone. **Red curves:** NMR spectra of the compounds in presence of the Bid3CCSS protein. **Green area:** BID3CCSS protein peak in the red curves, which is not visible in the blue curves. **Red area:** No signal shifts were detectable in the red curves in comparison to the signals in the blue curve, which would indicate a compound-binding to the Bid3CCSS protein.

Preliminary co-crystallization and soaking experiments

As a third approach, the optimized crystallization protocol from the first part of the thesis was used for preliminary co-crystallization and soaking trials with the Bid3CCSS construct. These experiments could not only provide crucial information about the binding mode of the small molecules to the BID protein, the compounds could also lead to a stabilization of the flexible parts and/ or a changed protein packing, both of which were beneficial for further crystallization experiments.

Initial screens showed that the crystallization was not disturbed by DMSO concentrations up to 10 %. Therefore, BI-6c9 and the novel DPA compounds 1-3 were applied at a concentration of 1 mM and 10 % DMSO into the crystallization condition. Unfortunately, these experiments only yielded very small crystals which were not sufficient for synchrotron analysis.

Initial soaking experiments using 1 mM of the aforementioned compounds revealed that compound soaked crystals did not subsequently result in the destruction of the crystals. Some crystals were even stable for 24 hours. However, for the crystals soaked for 24 h, X-ray data sets were of insufficient quality to judge whether or not there was a binding of the compounds to the Bid3CCSS protein. Only for the DPA-3 compound, which was soaked for 1 h, a data set was obtained with a sufficient resolution of 2.1 Å. However, no compound binding was observed.

4. Discussion

Neurodegenerative disorders are of growing concern in the ageing modern societies and a leading cause for disability and death worldwide ^{165,166}. However, until now no causal treatment options are available and only symptomatic therapies are applied ¹⁶⁷. In recent years, oxidative cell death pathways such as ferroptosis have been of emerging relevance in these neurodegenerative processes. In this context, the pro-apoptotic protein BID is involved in the execution of this type of oxidative cell death by mediating mitochondrial impairments. Thus, BID and related mitochondrial dysfunction are interesting targets for the development of novel neuroprotective agents.

However, only two NMR structures were available for the BID protein today. Therefore, the first part of this thesis focused on the determination of the crystal structure for BID. Intensive optimization of the native Morpheus A5 crystallization conditions significantly improved the Bid3CCSS crystals making the protein accessible for X-ray measurements and structure determination. The crystal structure shows that the Bid3CCSS protein is a highly helical protein that crystallizes as a trimer. Although two of three monomers still have unstructured regions that lower the overall quality criteria of the structure, one monomer is sufficiently defined to be used for *in silico* compound searches in the future.

In parallel, as described in the second part of the thesis, novel diphenylamine (DPA) compounds were characterized in the ferroptosis paradigm. These compounds were previously developed upon a medicinal chemistry approach using BI-6c9 as a scaffold molecule. This study confirmed that the novel DPA compounds have an increased antiferroptotic potency compared to the former developed BID inhibitors. Moreover, the results suggest that especially the maintenance of mitochondrial integrity and the abrogation of ROS contributed to the observed protective mechanism. Furthermore, the establishment of the MST assay, NMR-based measurements and co-crystallization/ soaking protocols provide promising techniques to elucidate whether BID targeting is the main mechanism of action of the DPA compounds.

In conclusion, the thesis set a basis for the development and validation of ferroptosis inhibitors based on BID inhibition in the future and highlights strategies for mitochondrial protection as effective treatment options against neurodegenerative diseases.

4.1. BID crystallization

Unravelling the molecular structure of a protein significantly enhances the understanding in the interaction of the protein with other biomolecules and/ or ligands which leads to a more precise insight into the protein's mechanisms and the potential participation in diseases.

Although the pivotal role of BID in neuronal cell death is well-established, so far only two NMR structures have been described for the BID protein^{94,95}. Upon these data, BID is a highly helical protein, with the hydrophobic helix 6 and helix 7 being surrounded by the remaining six amphiphilic helices. In addition, an unstructured loop is exposed on the outside of the helical core, which functions as the target site for several proteins for BID cleavage into its pro-apoptotic truncated form, i.e. t-BID⁹⁶.

So far, only crystal structures of the BID-BH3 domain (amino acids ~90-100), located in helix 3 of the BID protein (Figure 5), have been published. The available structures show the BH3 domain in complex with other pro- and anti-apoptotic proteins of the BCL-2 family¹⁶⁸⁻¹⁷¹. However, for understanding the mechanism of BID-mediated effects, especially in caspase-independent cell death paradigms, the sole description of the BH3 domain interaction of BID with other BCL 2 family members is not sufficient. For example the targeting of the mitochondrial membrane, which is presumably of crucial importance in oxidative cell death, was performed with the helices H6 and H8, and thus independently of the BH3 domain^{104,172-174}. Moreover, the cardiolipin binding domain (CBD) (amino acids 103-162) was shown to induce cytochrome c release in isolated mitochondria as well as in isolated mitochondria from Bax^{-/-} MEF cells, demonstrating alternative mechanisms of cytochrome c release that are independent of the BH3 domain and any BID-BAX interaction¹⁷⁵. Furthermore, especially in caspase-independent oxidative cell death, cleavage of full-length BID was until now not found in neuronal cells^{29,36,134}. This suggests that other mechanisms for BID activation may exist apart from BID cleavage and BH3-dependent cell death. Moreover, solving the crystal structure may help to understand more precisely the possible interaction of BID and VDAC, which is still controversial^{118,119}.

In addition, in today's drug discovery research, it is inevitable to address individual target proteins with highly specific compounds to increase the treatment effects

while reducing side effects due to non-specific binding to other proteins. Having outlined the importance of the BID molecule in caspase-dependent and independent cell death in neurons^{15,19}, the search for potent and specific inhibitors of BID would be significantly supported by the option of *in silico* compound searches on the basis of a crystal structure. That the availability of crystal structures stimulate the process of inhibitor development was already demonstrated for other BCL-2 family members^{176–180}.

In the present thesis, the Morpheus A5 crystallization condition for the Bid3CCSS construct was further optimized, in which small crystals were previously obtained in a reproducible manner¹⁰⁰. The Bid3CCSS protein solution needed to be stored at 4°C, as thawed protein solutions, after being stored at -80°C, resulted in significantly less crystal growth. Crystal growth was also impaired when the used Bid3CCSS protein solution was older than 3-4 months, so a fresh Bid3CCSS solution had to be prepared after this period. In addition, the protein concentration had to be adjusted to at least 10 mg/ml for proper crystal formation.

Optimization of the initial Morpheus A5 condition led to the removal of MgCl₂. All other substances including CaCl₂, both buffers (HEPES/ MOPS) and both PEGs (PEG550 MME, PEG 20000) were kept. Remarkably, CaCl₂ and both buffers (HEPES/ MOPS) significantly enhanced crystal growth when their concentrations were increased ~3-4 times compared to the original Morpheus A5 condition. In murine hepatocytes, BID has been shown to be involved in endoplasmic calcium regulation¹⁸¹ indicating towards a certain affinity of BID to calcium which might explain the increased crystal growth upon higher calcium concentrations during crystallization. However, these crystals had to be subjected to a seeding protocol followed by cryo-protection to obtain crystals of a proper shape and size without ice ring formation that could be measured at the synchrotron. In these X-ray measurements, data sets for the Bid3CCSS protein were obtained with resolutions between 2.0 – 2.3 Å

However, phase determination using molecular replacement was not possible with the available NMR structures. This could be due to the fact that the protein structures may vary between the NMR structure obtained in solution and X-ray structures obtained in the solid state. Moreover, NMR structures did not reveal a

single constitution for a protein so that it could be difficult to find the correct state that fits the X-ray data between many incorrect data ¹⁸², even though molecular replacement for Bid3CCSS was tried with all available states of the BID NMR-structure. In addition, especially old NMR structures are not good enough to be used as a model for molecular replacement in crystal structures ¹⁸³. Therefore, heavy metal soaks using gadolinium-acetate were performed to determine the phases. This information was then applied to the apo crystal structure data set so that the first ever crystal structure of the Bid3CCSS protein could be modeled.

The crystal structure revealed that the Bid3CCSS construct is crystallized as a trimer suggesting an intrinsic tendency of the protein towards self-assembly. This supports previous findings showing BID homo-oligomerization at mitochondria ¹²⁵ which may contribute to its mechanism of action. However, both SDS-PAGE and the ESI-MS measurements did not show an oligomerization in solution. Therefore, oligomerization might only occur under special circumstances, i.e., when BID is activated during cell death or in supersaturated solutions during the crystallization process.

Furthermore, structural analysis demonstrated a highly helical composition of the Bid3CCSS protein, confirming the general construction of the BID protein obtained by the NMR measurements (Figure 57). However, two of three monomers exhibited disordered regions which resulted in quality criteria for the crystal structures that was not as good as expected for a crystal structure with a resolution of 2.0 – 2.3 Å. However, the best resolved monomer (Figure 57 B) may already be sufficient for initial preliminary docking experiments and compound search.

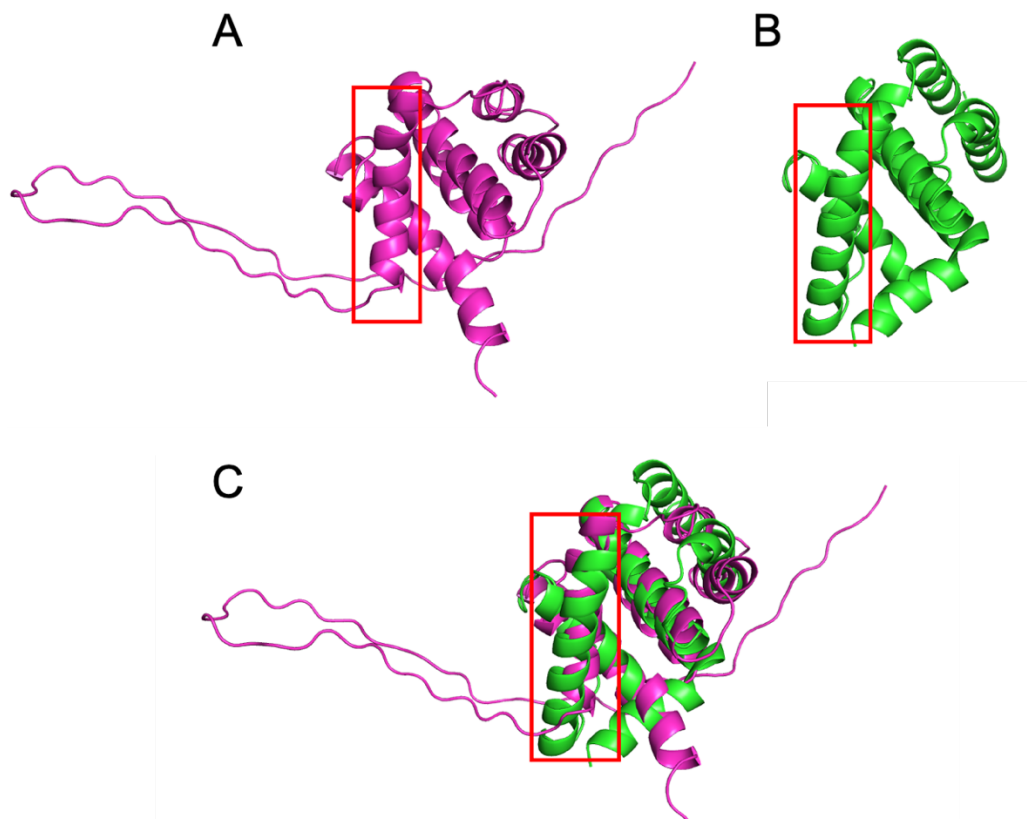


Figure 57. Comparison of the NMR structure and the crystal structure of BID. A) BID NMR structure (1DDB). **B)** Best resolved monomer of the crystal structure. **C)** Overlap of the NMR structure (pink) and crystal structure (green) of BID. Red boxes mark the helix 3.

Even though the optimization process described in this thesis was of great success, the crystallization procedure is still sensitive to disturbances that could reduce crystal growth. The most error-prone components might be the PEGs, as they are critical components for the successful Bid3CCSS crystallization. Slight deviations in the composition of the PEGs, for example, when another batch was used, had a striking impact on crystal growth so that PEG concentration had to be adjusted. Furthermore, temperatures over 20°C also significantly hindered crystallization. In addition, crystal formation per se is still problematic. Even with

the best crystallization conditions elaborated so far, the probability for growing nicely shaped Bid3CCSS apo crystals of a proper size was only about 10% (without seeding). When these apo crystals were then subjected to the streak seeding protocol, the crystallization probability increased significantly. However, when the seed crystals were older than 2–3-months, crystal growth was again reduced.

In order to further enhance the crystallization ability of the Bid3CCSS construct, modifications of the crystal contact sides are recommended. Therefore, a method called Surface Entropy Reduction (SER) could be used. Here, solvent exposed amino acids with disordered side chains possessing high intrinsic entropy like Lys, Glu, and Gln are replaced in favor of short amino acids such as Ala¹⁵⁹. This approach is particularly promising, when simultaneously two or three amino acids of high entropy were removed that were located in near proximity¹⁸⁴. With the help of the freely available SER prediction tool (SERp)¹⁸⁵, <http://www.doe-mpi.ucla.edu/Services/SER>, the amino acid cluster AA: 80-83 of Bid3CCSS was defined as the most promising sequence for this approach (Figure 58). Furthermore, the modified crystal contact sides may also cause the crystal packing to change from the trimeric to a monomeric structure.

Proposed Mutations:

Cluster #1:	Residues 80 - 83: EEDK [?]
• E 80 => A	
• E 81 => A	
• K 83 => A	
	SERp Score: 4.75 [?]
Cluster #2:	Residues 39 - 41: QAYSQEE [?]
• Q 39 => A	
• E 40 => A	
• E 41 => A	
	SERp Score: 3.62 [?]
Cluster #3:	Residues 116 - 118: AKKVASHA [?]
• K 117 => A	
• K 118 => A	
	SERp Score: 3.2 [?]

Figure 58. Surface Entropy Reduction prediction (SERp) of the Bid3CCSS protein. Bid3CCSS protein sequence was analyzed using the SERp online tool in order to detect high entropic clusters that could compromise crystallization. Cluster #1 (AA 80-83 of Bid3CCSS) turned out to be the most promising sequence for mutations to Ala to enhance crystallization. Cluster #2 (AA 39-41) and Cluster #3 (AA 116-118) are additional options for this approach.

Finally, it was investigated whether the Bid3CCSS protein was still biologically active, since the modifications of the BID protein introduced in favor of better crystallization possibly resulted in a rearrangement of some helices (Figure 57 C) which could interfere with the function of BID.

Therefore, Bid3CCSS was applied to isolated mitochondria of the frontal cortex of Sprague-Dawley rats followed by analysis of the mitochondrial bioenergetics using the Seahorse Analyzer. Previous studies have demonstrated that BID translocation to the mitochondria caused significant impairments in mitochondrial constitution and bioenergetics ^{35,45}.

Bid3CCSS protein treatment led to an overall and concentration-dependent mitochondrial dysfunction represented by a decreased respiratory control ratio. Thereby, basal and state 3 respiration were most significantly impaired indicating that especially oxidative phosphorylation machinery was affected by the Bid3CCSS treatment. This observation was in line with studies demonstrating that the application of recombinant t-BID to isolated HeLa mitochondria also suppressed mitochondrial state 3 respiration ¹⁷⁵. These similar effects of the modified Bid3CCSS compared to the unmodified t-BID construct on mitochondrial respiration confirmed that the Bid3CCSS construct was biologically active and functional.

4.2. Characterization of novel DPA compounds as ferroptosis inhibitors

Already in the early 2000s it became clear that BID participates in neuronal cell death. Bid knockout neurons were resistant against oxygen/glucose deprivation and Bid knockout mice subjected to cerebral ischemia developed significantly smaller brain infarct volumes ¹⁹.

Therefore, pharmacological compounds against BID were designed based on an NMR-based approach leading to the development of the first BID inhibitor BI-6c9 which exerted pronounced protective effects against oxidative cell death at concentrations of 10 μ M in HT22 cells ^{29,35,36,45}. However, BI-6c9 application *in vivo* was not successful due to its poor solubility and low bioavailability ¹⁴⁰. In the following years, 4-phenoxyaniline derivatives ¹⁴⁵ and N-phenyl-substituted thiazolidinediones ¹⁴⁶ were developed as BID inhibitors upon a medicinal chemistry approach using BI-6c9 as a scaffold structure. With the objective to generate novel compounds with increased activity against oxidative cell death pathways, Dr. Pfaff developed the diphenylamine compounds, again using the medicinal chemistry approach, which were then characterized in this study.

First, the potency of the DPA compounds to inhibit ferroptosis was investigated in MTT assays, microscopic analyses and Annexin V/ PI FACS measurements. In all assays, the novel compounds revealed a strong concentration-dependent protection in the ferroptosis paradigm induced by the XC- inhibitor erastin and the GPX-4 inhibitor RSL-3, respectively. The EC₅₀ values ranged from 0.23-0.32 μ M for the DPA compounds 1-3. In comparison to BI-6c9 the potency of the novel compounds was 10-fold increased ^{35,55,146}. When compared to the N-phenyl thiazolidinedione or the 4-phenoxyaniline derivatives, the DPA compounds were ~20-fold more effective in inhibiting oxidative cell death ^{145,146}. Additionally, xCELLigence measurements further revealed that at DPA concentrations of 1 μ M a persistent protection was provided. On the contrary, both, the thiazolidinedione and the 4-phenoxyaniline compounds only showed transient protection against glutamate treatment in concentrations of 10 μ M - 25 μ M ^{145,146}. For persistent protection, concentrations of 50 μ M were needed. These results further emphasize the increased potency of the novel DPA compounds against oxidative cell death

pathways. Notably, no indications of intrinsic cytotoxic effects of the DPA compounds were found in any of the cell death measurements. In the MTT assay, the low neurotoxic potential was additionally confirmed for concentrations up to 100 μ M suggesting that the compounds have a sufficient therapeutic window before neurotoxic effects occur.

Furthermore, the DPA compounds were unable to inhibit apoptotic cell death through staurosporine treatment. This implies a specificity of these novel compounds towards caspase-independent cell death mechanisms like ferroptosis and oxytosis. In addition, only the caspase inhibitor QVD and not the scaffold molecule BI-6c9 could block staurosporine induced apoptosis confirming previous results demonstrating that BID is probably not required for mediating staurosporine induced cell death ²⁹.

Moreover, simultaneous treatment of the novel DPA compounds with erastin or RSL-3 prevented the development of lipid peroxidation and cytosolic as well as mitochondrial ROS formation in a concentration-dependent manner. Previous studies showed that radical-trapping compounds such as liproxstatin-1 or ferrostatin-1 equally abrogated ferroptosis induced ROS development and ferroptotic cell death ³⁵. Therefore, it seemed obvious that the DPA compounds may inhibit ferroptosis as radical scavenging agents due to the inserted diphenylamine structure previously described as an antioxidative moiety ^{186,187}. However, the preliminary screening of the DPA compounds in the oxytosis paradigm demonstrated that the substituted compounds DPA 1-3 were 10-fold more effective in abrogating glutamate induced cell death than the unsubstituted starting molecule for DPA compound synthesis (p-aminodiphenylamine) ¹⁴⁷. This data already indicated that the antioxidative effect provided by the diphenylamine structure may be only partially responsible for the protective mechanism. Additionally, unlike ferrostatin-1 ^{38,188}, no direct radical scavenging effect could be demonstrated for the novel DPA compounds in the DPPH assay.

Moreover, the established radical scavenger Trolox was more effective than the DPA compounds in preventing H₂O₂ induced cell death and cytosolic ROS formation. In line with these results, the antioxidants liproxstatin-1 and ferrostatin-1 also showed strong protection from H₂O₂ induced cell death in a rat glioblastoma

cell line ¹⁸⁹. These experiments further indicated towards an only limited direct antioxidative activity of the novel anti-ferroptotic compounds.

Moreover, the DPA compounds did not abrogate ROS development by interfering with the antioxidant machinery by, for example, increasing the glutathione levels or GPX-4 expression.

In addition to ROS development, mitochondrial impairments are widely believed to play a key role in the mechanism of oxidative stress induced neurodegeneration ^{35,190,191}. As also shown in this study, mitochondrial demise upon ferroptosis induction comprises mitochondrial fragmentation, a loss of mitochondrial membrane potential and impaired mitochondrial energy metabolism. Pharmacological interventions, focusing on the rescue of mitochondria for instance via the mitochondrial ROS scavenger MitoQ or by BID inhibition were recently described as an effective strategy to prevent cell death in oxidative stress models ^{35,61,146}. Consequently, maintenance of mitochondrial integrity and functional cellular energy metabolism seems to be crucial for neuronal cell survival in the ferroptotic paradigm. Therefore, protecting mitochondria serves as a promising way, in particular in neurodegenerative diseases that involve excessive oxidative mitochondrial damage, i.e., Parkinson's disease ¹⁹².

All novel DPA compounds prevented the loss of mitochondrial membrane potential in a concentration-dependent manner in co-treatment with ferroptosis inducers. Accordingly, mitochondrial morphology and mitochondrial oxidative phosphorylation were preserved when the cells were simultaneously treated with erastin and 1 μ M of the novel DPA compounds. In contrast, 20 μ M of the thiazolidine compounds and 10 μ M for BI-6c9 was required for the maintenance of the mitochondrial membrane potential and mitochondrial respiration ¹⁴⁶. However, earlier studies showed that NSAIDs which also possess a diphenylamine structure (i.e. diclofenac) act as uncoupling agents of oxidative phosphorylation, thereby evoking decreased ATP levels and cytotoxicity ^{193,194}. In contrast, toxic effects were neither demonstrated in the TMRE assay, nor in the Seahorse measurements for either of the DPA compounds in the maximal protective concentration of 1 μ M. Determinations of ATP levels additionally revealed that mitochondrial integrity was preserved by the DPA compounds when treated concomitantly with erastin in a concentration-dependent manner.

These results showed that the novel DPA compounds protected the neuronal HT22 cells from mitochondrial impairment and were well-tolerated at the mitochondrial and cellular level.

The protective, anti-ferroptotic effects of the novel DPA compounds were further confirmed using the hypothalamus mHypo cell line, which was also responsive to erastin induced ferroptosis¹⁶⁴. Similarly, as shown in the HT22 cells, the most significant ferroptosis hallmarks such as lipid peroxidation, mitochondrial ROS formation, and loss of mitochondrial membrane potential were all completely abolished when DPA compounds were applied together with erastin in the mHypo cells.

Consequently, the DPA compounds can be expected to protect a broad variety of neuronal cells from ferroptotic cell death by abrogating ROS species and protecting mitochondria.

In addition, the effective time window for DPA compound application was investigated using post-treatment experiments in HT22 cells. Ferroptotic cell death was largely blocked when the DPA compounds were applied up to 6 h after initial erastin treatment. This is in line with the effective post-treatment time window of BI-6c9 in HT22 cells upon RSL-3 induced ferroptosis³⁵. Lipid, cytosolic and mitochondrial ROS development were also completely blocked when the DPA compounds were applied before the 6 h post-treatment time point. However, at treatment times 8-10 h after ferroptosis induction, the development of these ROS species could no longer be prevented. Intriguingly, DPA compound application at the 8 h post-treatment time point still largely maintained mitochondrial membrane potential at control levels although cell death was already determined.

These results further confirmed that the DPA compounds did not act as direct radical scavengers but rather interfere with the ROS formation process, especially in the early phase of ferroptosis when mitochondria were not yet affected. Presumably, mitochondrial impairments then led to a second phase of ROS development fueling the ongoing cell death progression that could no longer be halted by DPA compound application. A development of a delayed, secondary ROS boost was also reported in previous studies in the glutamate-induced oxytosis paradigm³⁶. Moreover, the ability of the novel compounds to maintain MMP up to

the 8 h time point provides further evidence that the protective mechanism of the DPA compounds was largely attributed to the mitochondrial protection. However, once the mitochondria were impaired in the detrimental course of ferroptosis, the execution of cell death continued, although a further decrease in the mitochondrial membrane potential could be prevented by the compounds.

The reported results from this study indicate that the mechanism of action of the DPA compounds to provide mitochondrial protection may involve the inhibition of the pro-apoptotic protein BID, like the scaffold molecule BI-6c9. This suggestion is supported by studies demonstrating that the key hallmarks of ferroptosis like lipid peroxide and mitochondrial ROS formation as well as mitochondrial demise were also abrogated by BID inhibition or genetic Bid depletion^{29,35,36}. However, structural analysis of the novel compounds revealed that the steric conformation of the DPA compounds largely differs from the BI-6c9 structure which could possibly preclude a binding event to the same hydrophobic crevice of BID¹⁴⁷.

In the established pIRES-tBid toxicity assay^{29,145,146}, all DPA compounds failed to protect the HT22 cells from dying. Interestingly, also BI-6c9 only showed very little protection in this series of experiments suggesting that the inhibitory ability of the compounds to protect against cell death induced by t-BID overexpression is not very robust and therefore could vary between experiments. Moreover, it is still unclear whether BID cleavage in its “activated” t-BID form is mandatory in the paradigm of caspase-independent cell death pathways in neuronal cells. So far, BID cleavage could not be demonstrated in HT22 cells in models of glutamate induced oxytosis^{29,146}. Additionally, other studies demonstrated that in HT22 cells and rat neurons BID migrates to mitochondria in its full-length form upon glutamate treatment^{29,133}. It appears that the t-BID overexpression assay is unsuitable in finally clarifying the potential role of full-length BID in oxidative cell death.

To elucidate more directly the binding ability of the compounds to BID, preliminary measurements were conducted using the microscale thermophoresis (MST) assay, an NMR-based approach and co-crystallization/ soaking trials. These experiments were performed using the previously established Bid3CCSS construct.

In MST measurements, DPA-2 and to a lesser extent DPA-3 interfered with the fluorescence signal resulting in a decreased fluorescence count, which should be considered while data analysis. Nevertheless, all compounds in concentrations of 1 mM showed a fluorescence shift in comparison to the DMSO control that could indicate for a binding event. However, these preliminary measurements need further optimization by carefully titrating protein, dye, compound and DMSO concentrations. Afterwards, it has to be investigated whether the observed signal shifts could be obtained in a concentration-dependent manner, which then would confirm a binding event.

On the contrary, for none of the compounds a clear binding-induced signal shift was observed in the NMR spectrum. However, the poor solubility of BI-6c9 and DPA-3 led to a poor signal-to-noise ratio that constrained a clear interpretation of the results. Interestingly, when the compounds were applied together with the Bid3CCSS protein, the signal strength was increased, which may indicate a direct interaction between the BID protein and the compounds, although, this could also be a nonspecific effect due to random protein-compound interaction. In summary, the positive control BI-6c9 was not functional and, therefore, it is still questionable whether there is truly no binding of the DPA compounds to the protein, or the experimental setup needs further optimization. In the selected assay settings, the protein-ligand interaction was studied with a large excess of ligand (~1:200). Previously, NMR measurements were conducted investigating BI-6c9 binding to a ^{15}N -labeled BID protein. Here, the compounds were applied at a protein-to-compound ratio of 1:2^{133,134}. These differences in the protein-to-compound ratio could possibly elicit a different binding mode of the compound to the protein. Therefore, NMR-assays using ^{15}N -labeled Bid3CCSS and a further adjusted compound-to-protein ratio could be an additional approach for studying compound-Bid3CCSS binding in the future.

Moreover, preliminary co-crystallization experiments were conducted in order to confirm a binding event to the Bid3CCSS protein. Successful co-crystallization could provide important structural information on the binding mode of the compounds possibly also apart from the previously described hydrophobic crevice of BID, which could be used for inhibitor development in the future¹⁴¹. Additionally,

compound binding may enhance the crystallization behavior due to reduction of the intramolecular flexibility and probably altered crystal packing.

For co-crystallization experiments the compound concentration should be 10-fold higher than the protein concentration ¹⁹⁵, however, due to the low water solubility of BI-6c9, 1 mM of BI-6c9 and the novel DPA compounds were applied to the crystallization conditions representing a compound-to-protein ratio of approximately 1:2. The first attempts did not result in the formation of any crystals suitable for X-ray measurements. This could be interpreted in several directions. First, the addition of ligands could lead to substantial conformational changes to the protein. This may be beneficial for crystal formation if it prevents trimerization of the Bid3CCSS protein as discussed earlier. However, a new constitution could need a completely different crystallization protocol which has to be established from scratch ¹⁵⁹. In contrary to this hypothesis, when the compounds were subjected to a soaking protocol, Bid3CCSS was stable for several hours so that an immediate, intense restructuring process due to compound binding is rather unlikely or extremely disfavored in the crystal state. Instead, the compounds could change the crystallization conditions in a way that crystal formation is not possible anymore, or the crystallization protocol is per se not optimal yet for the co-crystallization process.

In the compound-soaking experiments only one good data set for the DPA-3 compound was obtained so far due to varying quality of the used apo crystals. However, this DPA-3 soaked Bid3CCSS crystal did not reveal any ligand binding possibly because of the short incubation time of the compound with the Bid3CCSS crystal for only 1 hour. Additionally, 1 mM of compound may have been too low of a concentration for crystal soaking and should therefore be increased in future experiments. However, for compounds DPA-3 and BI-6c9 higher DMSO concentrations would have to be simultaneously increased to ensure solubility.

Nevertheless, the soaking experiments should be extended, if possible, with further optimized apo crystals.

To conclude, although the establishment of the MST, NMR based assays and co-crystallization/ soaking experiments were successfully conducted, extensive optimization of those is still required to eventually clarify whether the DPA compounds address BID as their major target. Furthermore, these methods could also be used to validate new BID inhibiting compounds in the future.

However, also other molecular target structures for the DPA compounds beside BID are conceivable. Therefore, proteomic analysis could provide additional insights into how the expression pattern of the various mitochondrial proteins are altered by the compounds. Of particular interest would be changes of protein levels involved in the maintenance of the mitochondrial membrane potential, for example, the electron transport chain complexes.

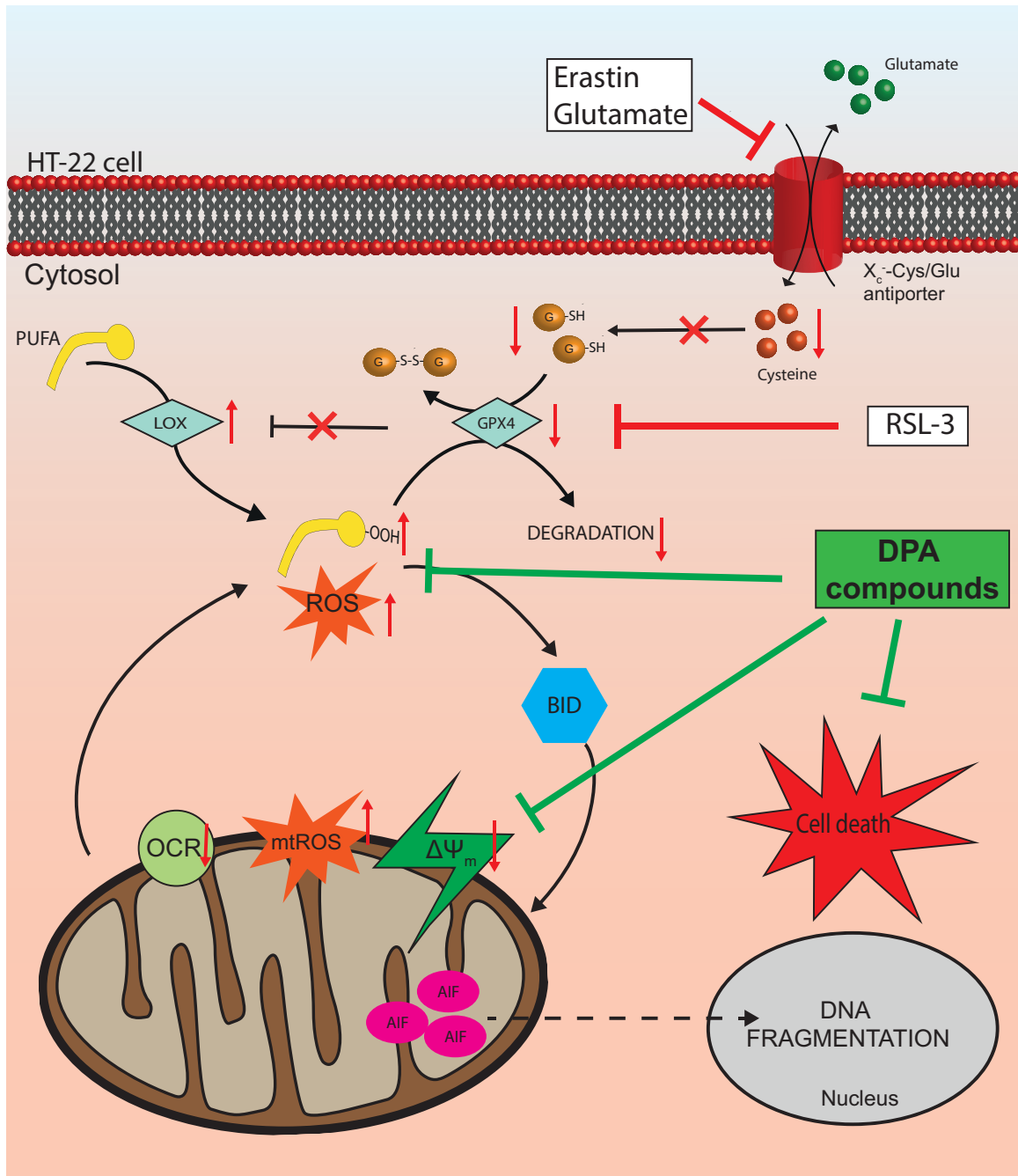


Figure 59 Mechanism of the DPA compounds preventing ferroptosis

The strong protective effect of the novel DPA compounds to prevent excessive ROS and lipid ROS burden, mitochondrial impairments and consequently ferroptotic cell death in various neuronal cell lines (HT22 and mHypo cells) at low micromolar concentrations together with the low intrinsic toxicity, encourages for further *in vivo* application of these compounds in the future. In addition, the good water solubility, especially of compounds DPA-1 and 2, provides a major advantage for *in vivo* application compared to BI-6c9.

In order to estimate the *in vivo* metabolism and toxicity of the novel DPA compounds, a risk assessment of the parent molecule diphenylamine by the German “Bundesanstalt für Arbeitsschutz und Arbeitsmedizin (BAuA)” about toxicity and metabolism (EINECS No: 204-539-4) was used. This risk assessment reported that diphenylamine is well orally bioavailable. Afterwards, the molecule is metabolized into 12 different metabolites. According to the available data, diphenylamine is regularly hydroxylated at the meta position. This position is also readily accessible in the novel DPA molecules suggesting a similar hydroxylation pattern for the compounds upon metabolism. Furthermore, during phase II metabolism, sulfatation and glucuronidation may occur at the hydroxyl groups resulting in fast renal elimination of the compounds. Notably, N-hydroxylamine metabolites which were regularly found in metabolism studies of aromatic amines and may cause methaemoglobinemia were not found in studies on diphenylamine metabolism. Moreover, studies in mammals revealed low acute oral toxicity and no neurotoxicity. Furthermore, a dose of 0.075 mg/ kg bw/day diphenylamine is considered acceptable for long-term intake, as shown by studies in rats over two years ¹⁹⁶.

However, the metabolism pattern can drastically change through variation of the precursor molecule. Therefore, *in silico* ADME and toxicity studies with the open-access *preADMET-server* ¹⁹⁷ and *admetSAR-server* ¹⁵⁷ were conducted to simulate possible side effects and metabolism of the DPA compounds. Here, in line with the reports on the parent molecule diphenylamine, a low carcinogenicity and mutagenicity with acceptable oral bioavailability were predicted for all DPA derivatives (Table 35). However, renal excretion seemed to be highly dependent on the substitution pattern, so that DPA-3 was suggested to be much better renally excreted than the other two compounds. Predictions of possible metabolism

indicate possible P-glycoprotein inhibition for DPA-1 and 2, whereas DPA-1 and 3 could be substrates for the Cyp3A4 enzyme, however, this is also the case for most drugs in use (Table 36).

Unfortunately, low blood-brain-barrier (BBB) permeability was predicted for DPA-1 and -2, possibly due to their charged nature, whereas for DPA-3 a good brain penetration was suggested (Table 35). Moreover, the *in silico* analysis revealed no major issues in terms of toxicity. The only exception was the predicted activity of two compounds on the hERG indicating a potential risk for cardiac arrhythmia (Table 35).

All in all, the *in silico* predictions revealed no major issues which would preclude further development or *in vivo* testing. These predictions should be experimentally addressed for confirmation or disproved in the course of future developments. For this purpose, a model systems of intracerebral hemorrhage (ICH) could be used, where hallmarks of neuronal ferroptosis like GSH depletion, lipid peroxidation as well as mitochondrial demise have recently been detected ¹⁵⁸. To circumvent possible pharmacokinetic issues with crossing of the blood brain barrier, as suggested for compound DPA-1 and 2 in the *in silico* analysis and metabolism, compound application through intracerebroventricular injections would be favorable. For dosing, conditions similar to those already elaborated in the cell culture are recommended, i.e., about 1 nmol of the different DPA compounds in an aqueous saline solution (containing 0,01% DMSO), the injected volume should not exceed 5 μ L so that a concentration of 1 μ M is reached in the brain.

Table 35 *In silico* ADME-parameters predicted with the preADMET-server:

Properties	DPA-1	DPA-2	DPA-3
(1) BBB-Penetration	0.0651745	0.0646825	2.64996
(2) Caco2 (nm/sec)	17.2368	15.1995	24.7099
(3) HIA (%)	87.538415	85.01442	94.491544
(4) MDCK (nm/sec)	6.81055	2.51159	0.0944907
(5) PPB (%)	73.398999	49.861928	90.898779
(6) hERG-Inhibition	ambiguous	high risk	high risk
(7) AMES Test	non-mutagen	non-mutagen	non-mutagen
(8) Carcinogenicity	non-carcinogen	non-carcinogen	non-carcinogen

(1) BBB: Blood-Brain Barrier; a value >1 indicates an CNS-active compound (2) Caco-2: Human intestinal cell line used for *in silico* simulation for cell permeability; low permeability: <4, medium permeability 4~70; high permeability: more than 70. (3) HIA: Human Intestinal Permeability; value closer to 1 represents better absorption through the intestine. (4) MDCK: Madin-Darby Canine Kidney; Represents the renal clearance of the molecule. Lower values indicate higher clearance (5) PPB: Plasma Protein Binding (6) hERG: human Ether-a-go-go Related Gene (7) Ames Test for potential mutagenicity of the compounds (8) Carcinogenicity indicates the cancer inducing ability of the molecule

Table 36 *In silico* metabolism properties of DPA-1, DPA-2 and DPA-3 obtained from the admetSAR-server

Properties	DPA-1	DPA-2	DPA-3
(1) P-gp Inhibition/Substrate	Yes/No	Yes/No	No/No
(2) Cyp-3A4 Inhibition/Substrate	No/Yes	No/No	No/Yes
(3) Cyp-2D6 Inhibition/Substrate	No/No	No/No	No/No
(4) Cyp-2C9 Inhibition/Substrate	No/No	No/No	No/No
(5) Cyp-2C19 Inhibition	No	No	No
(6) Cyp-1A2 Inhibition	No	No	No
(7) Cyp inhibitory promiscuity	No	No	No

5. Summary

Neurodegenerative disorders such as Alzheimer's and Parkinson's disease as well as stroke are of growing concern in our aging societies. In the last decades, biochemical hallmarks of these pathologies, containing excessive lipid peroxide formation, iron overload and mitochondrial impairments were linked to recently described forms of regulated, oxidative cell death mechanisms such as oxytosis and ferroptosis. Neurons are vulnerable to mitochondrial damage due to their high energy demand associated with the high electrical activity. Thus, protecting mitochondria is a reasonable approach for preventing neuronal dysfunction and cell death. In particular, the pro-apoptotic protein BID is of central interest in the pathology of neurodegeneration. Studies using Bid KO mice showed a significant decrease in infarct volumes upon stroke induction. Moreover, Bid knock-out trials in HT22 neurons demonstrated that BID was crucially involved in the mechanisms of oxidative cell death model of oxytosis and ferroptosis, possibly participating in the transfer of the ROS-dependent upstream events to mitochondria. Hence, BID is an attractive target molecule for ferroptosis inhibition and, therefore, for the development of novel compounds targeting neurodegenerative diseases.

However, *in silico* compound search was always hampered by a missing high-resolution X-ray structure of the BID protein. To improve the current understanding of the protein, the previously started approaches to elucidate the 3D crystal structure of the BID protein were continued. These experiments were conducted using the established Bid3CCSS construct. Previous high-throughput screens showed that in the Morpheus A5 condition, Bid3CCSS crystals could be consistently obtained in the form of ingrown needle clusters. Due to intensive screening of the components from the Morpheus A5 condition during the presented work, crystal quality was considerably enhanced. The best crystals from this optimization process were then subjected to a streak seeding protocol and cryoprotection. X-ray measurements of the obtained non-ingrown crystals resulted in data sets for the apo Bid3CCSS crystal with a resolution of 2.0 – 2.3 Å. After successful phase determination using gadolinium-acetate-soaked crystals, a crystal structure of the BID3CCSS could be modeled for the first time. The Bid3CCSS protein crystallized as a trimer. Although the protein is constructed mainly of alpha helices, large parts of two monomers were disordered, which resulted in below-average refinement statistics. However, one monomer is well-resolved and therefore could serve as a basis for targeted *in silico* compound development against the BID protein in the future.

Further crystallographic experiments should be conducted to lower the protein's flexibility in the crystal assembly, change the crystal packing by improving the crystal contacts, and identify (novel) binding pockets by the introduction of ligands.

In the second part of the thesis, novel diphenylamine (DPA) compounds were characterized in ferroptosis. These compounds were previously developed upon a medicinal chemistry approach using the first BID inhibitor BI-6c9 as a scaffold molecule to identify novel inhibitors of oxidative cell death. The selected DPA compounds 1-3 were the most potent inhibitors against glutamate induced oxytosis in preliminary experiments. Similarly, these novel DPA compounds were very potent and selective ferroptosis inhibitors. With EC50 values between 0.23-0.32 μM , the compounds were 10-20-fold more potent in preventing oxidative cell death than the previously described BID inhibitors. The DPA compounds abrogated lipid ROS formation, as the most conclusive hallmark of ferroptosis, as well as cytosolic and mitochondrial ROS formation without affecting the upstream cascade of ferroptosis including glutathione levels and GPX4 expression. Interestingly, a pronounced ROS scavenging effect by the DPA compounds could be excluded indicating that a direct antioxidant effect, possibly provided by the diphenylamine structure, was of minor relevance for the observed protective effects.

Moreover, mitochondrial respiration and constitution were maintained in a concentration-dependent manner. Post-treatment experiments substantiated the suggestion that mitochondrial protection and an interference in the ROS development processes by the compounds may contribute to the protective mechanism. Testing BID as a potential target structure in t-BID overexpression assays, failed to demonstrate a significant effect of the DPA compounds on t-BID. Moreover, preliminary binding assays of the compounds to the Bid3CCSS protein construct using MST and NMR techniques as well as co-crystallization and soaking experiments showed no clear binding activities so far, although these assays need further optimization.

In conclusion, these results highlight the role for mitochondrial protection as a strategy for the development of anti-ferroptotic compounds as possible new treatment options of neurodegenerative disorders in the future. The *in vitro* results encourage for further *in vivo* testing of the DPA compounds to evaluate the toxicity and effectiveness in models where ferroptosis might play a significant role, as for example in cerebral hemorrhage.

6. Zusammenfassung

Neurodegenerative Erkrankungen wie die Alzheimer- und Parkinson-Krankheit als auch der Schlaganfall sind von zunehmender Bedeutung in unserer alternden Gesellschaft.

In den vergangenen Jahren wurden bei diesen Erkrankungsbildern biochemische Merkmale, wie eine übermäßige Lipidperoxidbildung, Eisenüberladung und eine Schädigung der Mitochondrien festgestellt. Diese Merkmale sind eng mit den kürzlich beschriebenen Formen des regulierten, oxidativen Zelltods verknüpft, die als Oxytose und Ferroptose bezeichnet werden. Für Neurone ist eine Schädigung der Mitochondrien besonders problematisch, da diese infolge ihrer elektrischen Aktivität einen sehr hohen Energiebedarf aufweisen. Daher stellen Ansätze, die auf den Schutz der Mitochondrien abzielen, eine sinnvolle Möglichkeit dar, neuronale Zellen vor dem Untergang zu schützen. Insbesondere das pro-apoptotische Protein BID ist dabei von zentraler Bedeutung. *In vitro* und *in vivo* Studien belegen eine enge Verbindung zwischen dem BID Protein und neuronalem Zelltod, der unter anderem durch Oxytose und Ferroptose hervorgerufen sein kann. Daher ist das BID Protein ein interessantes Zielmolekül, um z.B. Ferroptose-Inhibitoren zu entwickeln, die anschließend gegebenenfalls als Wirkstoffe zur Behandlung von neurodegenerativen Erkrankungen eingesetzt werden könnten.

Die computergestützte *in silico* Suche nach neuen Wirkstoffkandidaten war jedoch bislang nur eingeschränkt möglich, da hochaufgelöste 3D-Röntgenstrukturdaten des BID-Proteins fehlten. Daher sollte in der vorliegenden Arbeit die Kristallstruktur des BID-Proteins aufgeklärt werden. Für diese Experimente wurde das bereits etablierte Bid3CCSS-Konstrukt genutzt. Im Rahmen früherer Arbeiten durchgeführte Hochdurchsatz-Screens zeigten, dass in der Morpheus A5-Bedingungen zuverlässig Bid3CCSS Kristalle erhalten wurden, die allerdings starke Verwachsungen aufwiesen. Durch eine akribische, strukturierte Testung aller Bestandteile der Ausgangsbedingung, mit anschließendem Seeding und Kryo-Schutz konnte die Kristallqualität erheblich verbessert werden. Die durch dieses Vorgehen erhaltenen stäbchenförmigen Kristalle wurden anschließend röntgenkristallographisch untersucht. Dabei wurden für die apo Bid3CCSS-Kristalle Datensätze mit einer Auflösung von 2,0-2,3 Å erhalten. Nach erfolgreicher Phasenbestimmung, mit Gadolinium-Acetat-getränkten Bid3CCSS Kristallen, konnte nun erstmalig eine Kristallstruktur des Bid3CCSS Proteins erstellt werden. Bid3CCSS kristallisierte dabei als Trimer. Obwohl das Protein hauptsächlich aus Alpha-Helices aufgebaut ist, lagen größere Bereiche von zwei der drei Monomere weitgehend ungeordnet vor, was zu einer unterdurchschnittlichen Verfeinerungsstatistik führte. Allerdings wies die Kristallstruktur eines Monomers eine definierte Elektronendichte für die gesamte

Aminosäurenkette auf, sodass dieses für zukünftige *in silico*-Versuche zur Ligandenfindung herangezogen werden kann.

Es wird dennoch empfohlen weiterführende kristallographische Experimente durchzuführen, um die Flexibilität des Proteins im Kristallverband zu verringern, die Kristallpackung durch eine Optimierung der Kristallkontakte zu ändern und mit Hilfe verschiedener Ligandenfragmente neue Bindungstaschen zu identifizieren.

Im zweiten Teil der Arbeit wurden neuartige Diphenylaminverbindungen (DPA) in Modellsystemen der Ferroptose charakterisiert. Diese Verbindungen wurden zuvor mittels medizinisch-chemischer Methoden entwickelt, um neuartige Inhibitoren gegen den oxidativen Zelltod zu identifizieren. Der bekannte BID-Inhibitor BI-6c9 diente dabei als Matrize. In der vorliegenden Studie zeigte sich, dass diese DPA-Verbindungen sehr potente und selektive Ferroptose-Inhibitoren darstellten. Mit EC₅₀-Werten zwischen 0,23-0,32 µM waren die neuen Verbindungen um das 10-20-fache protektiver gegen den oxidativen Zelltod als alle bislang beschriebenen BID-Inhibitoren. Die DPA-Verbindungen waren dabei in der Lage die Bildung von Lipid-ROS, sowie zytosolische und mitochondriale ROS Entstehung zu unterdrücken. Diese Hemmung erfolgte ohne eine Beeinflussung der Glutathionspiegel und der GPX4-Expression, welche wesentliche Bestandteile des antioxidativen Systems der Zelle darstellen. Ausgeprägte Radikalfänger-Eigenschaften der DPA-Verbindungen konnten ebenfalls nicht festgestellt werden. Dahingegen wurde die mitochondriale Integrität durch die Verbindungen konzentrationsabhängig bewahrt. Nachbehandlungsexperimente untermauerten schließlich die Annahme, dass eine durch die DPA-Verbindungen vermittelte Mitochondrienprotektion sowie eine Störung der ROS-Bildungsprozesse zum Schutzmechanismus beitragen. Untersuchungen der Verbindungen mittels t-BID-Toxizitätsexperimenten, NMR- und MST-Methoden sowie Co-Kristallisations- und Soaking-Experimenten, konnten bis dato keine eindeutige Interaktion der neuen Verbindungen mit dem BID/ t-BID Protein bestätigen oder entsprechende Bindungsstellen definieren. Um diese Fragestellung allerdings abschließend klären zu können, bedürfen die genannten Testverfahren weiterer Optimierung.

Zusammenfassend unterstreicht diese Arbeit den mitochondrialen Schutz als mögliche Strategie für die Entwicklung weiterer Ferroptose-Inhibitoren, welche als zukünftige Behandlungsoptionen von neurodegenerativen Erkrankungen eingesetzt werden könnten. Die *in vitro*-Ergebnisse sprechen dafür, die DPA-Verbindungen weiter *in vivo* zu untersuchen, um weitere Erkenntnisse zur Toxizität und Wirksamkeit in Modellen zu gewinnen, in denen Ferroptose eine wichtige Rolle spielen könnte. Dafür würden sich z.B. Modelle des hämorrhagischen Schlaganfalls eignen.

7. Abbreviations

+/-	In presence or absence (with or without)
2-DG	2-deoxyglucose
A1	Bcl-2-related protein A1
AA	Antimycin A
AB	Antibody
ACD	Accidental cell death
ACSL4	Acyl-CoA synthetase long-chain family member 4
Acyl-CoA	Acyl-Coenzyme A
AD	Alzheimer's disease
ADME	Absorption, distribution, metabolism, elimination
ADP	Adenosinediphosphate
AIF	Apoptosis-inducing-factor
ALOX12-15	12/15-lipoxygenase
Annexin V FITC	Annexin V conjugated with fluorescein isothiocyanate
ANOVA	Analysis of variances
AnV/ PI	Annxin V FITC
APAF 1	Apoptotic protease-activating factor 1
apo	Unliganded
APS	Ammonium persulfate solution
ATP	Adenosinetriphosphate
BAD	Bcl-2 antagonist of cell death
BAK	Bcl-2 antagonist killer 1
BAX	Bcl-2 associated x protein
BBB	Blood-Brain Barrier
BCA	Bicinchoninic acid
BCL-2,	B-cell lymphoma-2
BCL-W	Bcl-2-like protein 2
BCL-XL	Bcl-2 related gene, long isoform
BF	Bright field
BH	BCL-2 homology
BID	BH3 interacting domain death agonist
BID	Bcl-2 interacting domain death antagonist
bidest. H2O	Double distilled water
BIK	Bcl-2-interacting killer
BIM	Bcl-2-interacting mediator of cell death
BODIPY	4,4-Difluoro-5-(4-phenyl-1,3-butadienyl)-4-bora 3a,4a-diaza-sindacene-3-undecanoic acid
BSA	Bovine serum albumin
bw	Body weight
CBD	Cardiolipin binding domain

CCI	Controlled cortical impact
CI	Cell index
CRISPR/ Cas9	Clustered regularly-interspaced short palindromic repeats/ CRISPR associated protein 9
Ctrl	Control
Cyp	Cytochrome P450
D6-DMSO	Hexadeutero-dimethylsulfoxid
DAPI	4',6-Diamidino-2-phenylindole
DCF	2',7'-dichlorodihydrofluorescein diacetate
DFO	Deferoxamine
DMEM	Dulbecco's Modified Eagle's Medium
DMSO	Dimethylsulfoxide
DNA	<i>Deoxyribonucleic acid</i>
DPA	Diphenylamine
DPPH	2,2diphenyl-1-picrylhydrazyl
DTNB	5,5'-dithio-bis2-(nitrobenzoic acid), Ellman's reagent
DTT	DL-Dithiothreitol
e.g.	Exempli gratia
EC100	Maximal effective concentration
EC50	Half maximal effective concentration
ECAR	extracellular acidification rate
EDTA	Ethylene diamine-tetra-acetic acid
EGTA	Ethylene glycol-bis(2-aminoethylether)-N,N,N',N'- tetraacetic acid
ER	Endoplasmatic reticulum
Era	Erastin
ETC	Electron transport chain
EtOH	Ethanol
FACS	Fluorescence-activated cell sorting
FCCP	Carbonyl cyanide-p-trifluoromethoxyphenylhydrazone
FCS	Heat-inactivated fetal calf serum
GPX4	Glutathione peroxidase 4
GSH	Glutathione
GST	Glutathione-S-transferase
HD	Huntington's disease
HEPES	4-(2-Hydroxyethyl)piperazine-1-ethanesulfonic acid
hERG	Human Ether-a-go-go Related Gene
HRP	Horseradish peroxidase
i.e.	Id est
IAP	Inhibitor of apoptosis protein
ICH	Intracerebral hemorrhage
IPTG	Isopropyl β -D-1thiogalactopyranoside

Abbreviations

KO	Knock-out
lat.	Latein
LB	Lysogeny broth
LOX	Lipoxygenases
M	Marker
MAS	Mitochondrial assay solution
MCL-1	Induced myeloid leukemia cell differentiation protein
MEF	Mouse embryonic fibroblasts
MES	2-(N-morpholino) ethanesulphonic acid
MME	Monomethyl ether
MMP	Mitochondrial membrane potential
MOAP-1	Modulator of apoptosis-1
MOMP	mitochondrial membrane permeabilization
MOPS	(3-(N-morpholino)propanesulfonic acid)
MSHE	Mitochondrial isolation buffer
MST	Microscale thermophoresis
MT	Mitotracker deep red
MTCH2	Mitochondrial carrier homolog 2
MTT	3-(4,5-dimethylthiazol-2yl)-2,5-diphenyltetrazolium bromide
n = x	Number of replicates
N-BAK	Neuronal BAK
n.s.	not significant
N ₂ (l)	Liquid nitrogen
NADPH	Nicotinamidadeninukleotidphosphat
NMDA	<i>N-Methyl-d-aspartic acid</i>
NMR	Nuclear magnetic resonance
NOXA	Phorbol-12-myristate-13-acetate-induced protein 1
NSAID	Non-steroidal anti-inflammatory drug
O ₂	Oxygen
OCR	Oxygen consumption rate
OGD	Oxygen glucose deprivation
OLIGO	Oligomycin
OPA-1	Optic Atrophy 1 protein
OptiMEM	OptiMEM I reduced serum medium
OXPHOS	Oxidative phosphorylation
p IRES	Internal ribosome entry site plasmid
P-gp	Permeability glycoprotein
p53	Tumor protein p53
PBS	Phosphate buffered saline
PCD	Programmed cell death
PD	Parkinson's disease

PEG	Polyethyleneglycole
PFA	paraformaldehyde
pH	Pondus hydrogenii
PI	Propidium iodide
PMSF	Phenylmethylsulfonyl fluoride
PUFA	Polyunsaturated fatty acids
PUMA	p53 upregulated modulator of apoptosis
PVDF	Polyvinylidene fluoride
RCD	Regulated cell death
RCR	Respiratory control ratio
RNA	Ribonucleic acid
ROS	Reactive oxygen species
Rot	Rotenone
RSL-3 (1S, 3R RSL-3)	RAS-selective lethal compound 3
RT	Room temperature
SAD	Single-wavelength anomalous diffraction
SAR by ILOEs	Structure activity relationships by interligand nuclear Overhauser effect
SD	Standard deviation
SDS	Sodium dodecyl sulfate
SEC	Size exclusion chromatography
SERp	Surface Entropy Reduction prediction
siRNA	Small interfering ribonucleic acid
Smac/ DIABLO	Second mitochondria – derived activator of caspase/direct IAP binding protein with low pI
STS	Staurosporine
t-Bid	Truncated Bid
TBS	Tris-buffered solution
TBST	Tris-buffered solution with Tween 20
TC	Thrombin cleavage
TCA	Tricarboxylic acid cycle
TL	Total lysate
TMRE	Tetramethylrhodamin ethyl ester
TNF	Tumor necrosis factor
Tris	Tris(hydroxymethyl)aminomethane
UV	Ultraviolet
V	Volumn
VDAC	Voltage-dependent anion channel
VIP	Vasoactive intestinal peptide
Vis	Visible
X _C ⁻ -system	Cysteine-Glutamate antiporter
xCT	Cysteine-Glutamate antiporter
^x p<x	Probability value

Abbreviations

ϵ	Extinction coefficient
V	Volt
L	Liter
g	Gram
M	Molar
m	Meter
RPM	Rounds per minute
min	Minute
h	Hour(s)
U	Unit
Da	Dalton
M	10^6
k	10^3
m	10^{-3}
μ	10^{-6}
n	10^{-9}
p	10^{-12}
ppm	Parts per million

8. References

- (1) Ditzel, M.; Meier, P. Apoptosis. *Cell* **2002**, *111* (4), 465–467. [https://doi.org/10.1016/S0092-8674\(02\)01130-3](https://doi.org/10.1016/S0092-8674(02)01130-3).
- (2) Tang, D.; Kang, R.; Vanden Berghe, T.; Vandenabeele, P.; Kroemer, G. The Molecular Machinery of Regulated Cell Death. *Cell Res.* **2019**, *29* (5), 347–364. <https://doi.org/10.1038/s41422-019-0164-5>.
- (3) Kerr, J. F. R.; Wyllie, A. H.; Curriert, A. R. *APOPTOSIS: A BASIC BIOLOGICAL PHENOMENON WITH WIDE-RANGING IMPLICATIONS IN TISSUE KINETICS*; 1972; Vol. 26.
- (4) Schweichel, J. -U; Merker, H. -J. The Morphology of Various Types of Cell Death in Prenatal Tissues. *Teratology* **1973**, *7* (3), 253–266. <https://doi.org/10.1002/tera.1420070306>.
- (5) Galluzzi, L.; Vitale, I. Molecular Mechanisms of Cell Death: Recommendations of the Nomenclature Committee on Cell Death 2018. *Cell Death Differ.* **2018**, *25*, 486–541. <https://doi.org/10.1038/s41418-017-0012-4>.
- (6) Galluzzi, L.; Bravo-San Pedro, J. M.; Vitale, I.; Aaronson, S. A.; Abrams, J. M.; Adam, D.; Alnemri, E. S.; Altucci, L.; Andrews, D.; Annicchiarico-Petruzzelli, M.; et al. Essential versus Accessory Aspects of Cell Death: Recommendations of the NCCD 2015. *Cell Death Differ.* **2015**, *22* (1), 58–73. <https://doi.org/10.1038/cdd.2014.137>.
- (7) Berghe, T. Vanden; Linkermann, A.; Jouan-Lanhouet, S.; Walczak, H.; Vandenabeele, P. Regulated Necrosis: The Expanding Network of Non-Apoptotic Cell Death Pathways. *Nat. Rev. Mol. Cell Biol.* **2014**, *15* (2), 135–147. <https://doi.org/10.1038/nrm3737>.
- (8) Conrad, M.; Angeli, J. P. F.; Vandenabeele, P.; Stockwell, B. R. Regulated Necrosis: Disease Relevance and Therapeutic Opportunities. *Nature Reviews Drug Discovery.* May 18, 2016, pp 348–366. <https://doi.org/10.1038/nrd.2015.6>.
- (9) Lalaoui, N.; Lindqvist, L. M.; Sandow, J. J.; Ekert, P. G. The Molecular Relationships between Apoptosis, Autophagy and Necroptosis. *Semin. Cell Dev. Biol.* **2015**, *39*, 63–69. <https://doi.org/10.1016/j.semcdb.2015.02.003>.
- (10) Rhoads, D. M.; Umbach, A. L.; Subbiah, C. C.; Siedow, J. N. Mitochondrial Reactive Oxygen Species. Contribution to Oxidative Stress and Interorganellar Signaling. *Plant Physiology.* 2006, pp 357–366. <https://doi.org/10.1104/pp.106.079129>.
- (11) Tu, B. P.; Weissman, J. S. Oxidative Protein Folding in Eukaryotes: Mechanisms and Consequences. *Journal of Cell Biology.* The Rockefeller University Press February 2, 2004, pp 341–346. <https://doi.org/10.1083/jcb.200311055>.
- (12) Zeeshan, H. M. A.; Lee, G. H.; Kim, H.-R.; Chae, H.-J. Endoplasmic Reticulum Stress and Associated ROS. *Int. J. Mol. Sci.* 2016, Vol. 17, Page 327 **2016**, *17* (3), 327. <https://doi.org/10.3390/IJMS17030327>.
- (13) Chiurchiu, V.; Orlacchio, A.; Maccarrone, M. Is Modulation of Oxidative Stress an Answer? The State of the Art of Redox Therapeutic Actions in Neurodegenerative Diseases. **2016**. <https://doi.org/10.1155/2016/7909380>.
- (14) Halliwell, B. Biochemistry of Oxidative Stress. *Biochem. Soc. Trans.* **2007**, *35* (5), 1147–1150. <https://doi.org/10.1042/BST0351147>.
- (15) Singh, A.; Kukreti, R.; Saso, L.; Kukreti, S. Oxidative Stress: A Key Modulator in Neurodegenerative Diseases. *Molecules.* April 22, 2019, p 1583. <https://doi.org/10.3390/molecules24081583>.
- (16) Praticò, D. Oxidative Stress Hypothesis in Alzheimer's Disease: A Reappraisal. *Trends in Pharmacological Sciences.* Elsevier December 1, 2008, pp 609–615. <https://doi.org/10.1016/j.tips.2008.09.001>.
- (17) Zhao, Y.; Zhao, B. Oxidative Stress and the Pathogenesis of Alzheimer's Disease. *Oxidative Medicine and Cellular Longevity.* 2013. <https://doi.org/10.1155/2013/316523>.
- (18) Stack, E. C.; Matson, W. R.; Ferrante, R. J. Evidence of Oxidant Damage in Huntington's Disease: Translational Strategies Using Antioxidants. In *Annals of the New York Academy of Sciences*; Blackwell Publishing Inc., 2008; Vol. 1147, pp 79–92. <https://doi.org/10.1196/annals.1427.008>.
- (19) Culmsee, C.; Plesnila, N. Targeting Bid to Prevent Programmed Cell Death in Neurons. *Biochem. Soc. Trans.* **2006**, *34* (Pt 6), 1334–1340. <https://doi.org/10.1042/BST0341334>.
- (20) Coyle, J. T.; Puttfarcken, P. Oxidative Stress, Glutamate, and Neurodegenerative Disorders. *Science (80-)*. **1993**, *262* (5134), 689–695. <https://doi.org/10.1126/science.7901908>.
- (21) Uttara, B.; Singh, A. V.; Zamboni, P.; Mahajan, R. T. *Oxidative Stress and Neurodegenerative Diseases: A Review of Upstream and Downstream Antioxidant Therapeutic Options*; 2009; Vol. 7.
- (22) Murphy, T. H.; Miyamoto, M.; Sastre, A.; Schnaar, R. L.; Coyle, J. T. Glutamate Toxicity in a Neuronal Cell Line Involves Inhibition of Cystine Transport Leading to Oxidative Stress. *Neuron* **1989**, *2* (6), 1547–1558. [https://doi.org/10.1016/0896-6273\(89\)90043-3](https://doi.org/10.1016/0896-6273(89)90043-3).
- (23) Bassi, M. T.; Gasol, E.; Manzoni, M.; Pineda, M.; Riboni, M.; Martín, R.; Zorzano, A.; Borsani, G.; Palacín, M. Identification and Characterisation of Human XCT That Co-Expresses, with 4F2 Heavy Chain, the Amino Acid Transport Activity System Xc-. *Pflugers Arch. Eur. J. Physiol.* **2001**, *442* (2), 286–296. <https://doi.org/10.1007/s004240100537>.
- (24) Bannai, S. Exchange of Cystine and Glutamate across Plasma Membrane of Human Fibroblasts. *J. Biol. Chem.* **1986**, *261* (5), 2256–2263. [https://doi.org/10.1016/s0021-9258\(17\)35926-4](https://doi.org/10.1016/s0021-9258(17)35926-4).
- (25) Goji, T.; Takahara, K.; Negishi, M.; Katoh, H. Cystine Uptake through the Cystine/Glutamate Antiporter XCT Triggers Glioblastoma Cell Death under Glucose Deprivation. *J. Biol. Chem.* **2017**, *292* (48), 19721–19732. <https://doi.org/10.1074/jbc.M117.814392>.
- (26) Dwivedi, D.; Megha, K.; Mishra, R.; Mandal, P. K. Glutathione in Brain: Overview of Its Conformations, Functions, Biochemical Characteristics, Quantitation and Potential Therapeutic Role in Brain Disorders. *Neurochemical Research.* Springer July 1, 2020, pp 1461–1480. <https://doi.org/10.1007/s11064-020-03030-1>.
- (27) Tan, S.; Schubert, D.; Maher, P. Oxytosis: A Novel Form of Programmed Cell Death. *Curr. Top. Med. Chem.* **2001**, *1* (6), 497–506. <https://doi.org/10.2174/1568026013394741>.
- (28) Fukui, M.; Song, J. H.; Choi, J.; Choi, H. J.; Zhu, B. T. Mechanism of Glutamate-Induced Neurotoxicity in HT22 Mouse Hippocampal Cells. *Eur. J. Pharmacol.* **2009**, *617* (1–3), 1–11. <https://doi.org/10.1016/j.ejphar.2009.06.059>.
- (29) Landshamer, S.; Hoehn, M.; Barth, N.; Duvezin-Caubet, S.; Schwake, G.; Tobaben, S.; Kazhdan, I.; Becattini, B.; Zahler, S.; Vollmar, A.; et al. Bid-Induced Release of AIF from Mitochondria Causes Immediate Neuronal Cell

References

- Death. *Cell Death Differ.* **2008**, *15* (10), 1553–1563. <https://doi.org/10.1038/cdd.2008.78>.
- (30) Brigelius-Flohé, R.; Maiorino, M. Glutathione Peroxidases. *Biochim. Biophys. Acta - Gen. Subj.* **2013**, *1830* (5), 3289–3303. <https://doi.org/10.1016/j.bbagen.2012.11.020>.
- (31) Lewerenz, J.; Ates, G.; Methner, A.; Conrad, M.; Maher, P. Oxytosis/Ferroptosis-(Re-) Emerging Roles for Oxidative Stress-Dependent Non-Apoptotic Cell Death in Diseases of the Central Nervous System. *Front. Neurosci.* **2018**, *12*, 214. <https://doi.org/10.3389/fnins.2018.00214>.
- (32) Seiler, A.; Schneider, M.; Förster, H.; Roth, S.; Wirth, E. K.; Culmsee, C.; Plesnila, N.; Kremmer, E.; Rådmark, O.; Wurst, W.; et al. Glutathione Peroxidase 4 Senses and Translates Oxidative Stress into 12/15-Lipoxygenase Dependent- and AIF-Mediated Cell Death. *Cell Metab.* **2008**, *8* (3), 237–248. <https://doi.org/10.1016/J.CMET.2008.07.005>.
- (33) Yang, W. S.; Stockwell, B. R. Synthetic Lethal Screening Identifies Compounds Activating Iron-Dependent, Nonapoptotic Cell Death in Oncogenic-RAS-Harboring Cancer Cells. *Chem. Biol.* **2008**, *15* (3), 234–245. <https://doi.org/10.1016/j.chembiol.2008.02.010>.
- (34) Yang, W. S.; Sriramaratnam, R.; Welsch, M. E.; Shimada, K.; Skouta, R.; Viswanathan, V. S.; Cheah, J. H.; Clemons, P. A.; Shamji, A. F.; Clish, C. B.; et al. Regulation of Ferroptotic Cancer Cell Death by GPX4. *Cell* **2014**, *156* (1–2), 317–331. <https://doi.org/10.1016/j.cell.2013.12.010>.
- (35) Jelinek, A.; Heyder, L.; Daude, M.; Plessner, M.; Krippner, S.; Grosse, R.; Diederich, W. E.; Culmsee, C. Mitochondrial Rescue Prevents Glutathione Peroxidase-Dependent Ferroptosis. *Free Radic. Biol. Med.* **2018**, *117* (December 2017), 45–57. <https://doi.org/10.1016/j.freeradbiomed.2018.01.019>.
- (36) Tobaben, S.; Grohm, J.; Seiler, A.; Conrad, M.; Plesnila, N.; Culmsee, C. Bid-Mediated Mitochondrial Damage Is a Key Mechanism in Glutamate-Induced Oxidative Stress and AIF-Dependent Cell Death in Immortalized HT-22 Hippocampal Neurons. *Cell Death Differ.* **2011**, *18* (2), 282–292. <https://doi.org/10.1038/cdd.2010.92>.
- (37) Dolma, S.; Lessnick, S. L.; Hahn, W. C.; Stockwell, B. R. Identification of Genotype-Selective Antitumor Agents Using Synthetic Lethal Chemical Screening in Engineered Human Tumor Cells. *Cancer Cell* **2003**, *3* (3), 285–296. [https://doi.org/10.1016/S1535-6108\(03\)00050-3](https://doi.org/10.1016/S1535-6108(03)00050-3).
- (38) Dixon, S. J.; Lemberg, K. M.; Lamprecht, M. R.; Skouta, R.; Zaitsev, E. M.; Gleason, C. E.; Patel, D. N.; Bauer, A. J.; Cantley, A. M.; Yang, W. S.; et al. Ferroptosis: An Iron-Dependent Form of Nonapoptotic Cell Death. *Cell* **2012**, *149* (5), 1060–1072. <https://doi.org/10.1016/j.cell.2012.03.042>.
- (39) Muhoberac, B. B.; Vidal, R. Iron, Ferritin, Hereditary Ferritinopathy, and Neurodegeneration. *Front. Neurosci.* **2019**, *13* (December), <https://doi.org/10.3389/fnins.2019.01195>.
- (40) Fanzani, A.; Poli, M. Iron, Oxidative Damage and Ferroptosis in Rhabdomyosarcoma. *International Journal of Molecular Sciences*. MDPI AG August 7, 2017. <https://doi.org/10.3390/ijms18081718>.
- (41) Chen, X.; Yu, C.; Kang, R.; Tang, D. Iron Metabolism in Ferroptosis. *Frontiers in Cell and Developmental Biology*. Frontiers Media S.A. October 7, 2020, p 590226. <https://doi.org/10.3389/fcell.2020.590226>.
- (42) Stockwell, B. R.; Jiang, X.; Gu, W. Emerging Mechanisms and Disease Relevance of Ferroptosis. *Trends Cell Biol.* **2020**, *30* (6), 478–490. <https://doi.org/10.1016/j.tcb.2020.02.009>.
- (43) Kagan, V. E.; Mao, G.; Qu, F.; Angeli, J. P. F.; Doll, S.; Croix, C. S.; Dar, H. H.; Liu, B.; Tyurin, V. A.; Ritov, V. B.; et al. Oxidized Arachidonic and Adrenic PEs Navigate Cells to Ferroptosis. *Nat. Chem. Biol.* **2017**, *13* (1), 81–90. <https://doi.org/10.1038/nchembio.2238>.
- (44) Maher, P.; Currais, A.; Schubert, D. Using the Oxytosis/Ferroptosis Pathway to Understand and Treat Age-Associated Neurodegenerative Diseases. *Cell Chem. Biol.* **2020**, *27* (12), 1456–1471. <https://doi.org/10.1016/J.CHEMBIOL.2020.10.010>.
- (45) Neitemeier, S.; Jelinek, A.; Laino, V.; Hoffmann, L.; Eisenbach, I.; Eying, R.; Ganjam, G. K.; Dolga, A. M.; Oppermann, S.; Culmsee, C. BID Links Ferroptosis to Mitochondrial Cell Death Pathways. *Redox Biol.* **2017**, *12*, 558–570. <https://doi.org/10.1016/j.redox.2017.03.007>.
- (46) Angelova, P. R.; Horrocks, M. H.; Klenerman, D.; Gandhi, S.; Abramov, A. Y.; Shchepinov, M. S. Lipid Peroxidation Is Essential for α -Synuclein-Induced Cell Death. *J. Neurochem.* **2015**, *133* (4), 582–589. <https://doi.org/10.1111/jnc.13024>.
- (47) Chen, L.; Na, R.; Gu, M.; Richardson, A.; Ran, Q. Lipid Peroxidation Up-Regulates BACE1 Expression in Vivo: A Possible Early Event of Amyloidogenesis in Alzheimer's Disease. *J. Neurochem.* **2008**, *107* (1), 197–207. <https://doi.org/10.1111/j.1471-4159.2008.05603.x>.
- (48) Williams, T. I.; Lynn, B. C.; Markesbery, W. R.; Lovell, M. A. Increased Levels of 4-Hydroxynonenal and Acrolein, Neurotoxic Markers of Lipid Peroxidation, in the Brain in Mild Cognitive Impairment and Early Alzheimer's Disease. *Neurobiol. Aging* **2006**, *27* (8), 1094–1099. <https://doi.org/10.1016/j.neurobiolaging.2005.06.004>.
- (49) Hauser, D. N.; Dukes, A. A.; Mortimer, A. D.; Hastings, T. G. Dopamine Quinone Modifies and Decreases the Abundance of the Mitochondrial Selenoprotein Glutathione Peroxidase 4. *Free Radic. Biol. Med.* **2013**, *65*, 419–427. <https://doi.org/10.1016/j.freeradbiomed.2013.06.030>.
- (50) Yoritaka, A.; Hattori, N.; Uchida, K.; Tanaka, M.; Stadtman, E. R.; Mizuno, Y. Immunohistochemical Detection of 4-Hydroxynonenal Protein Adducts in Parkinson Disease. *Proc. Natl. Acad. Sci. U. S. A.* **1996**, *93* (7), 2696–2701. <https://doi.org/10.1073/pnas.93.7.2696>.
- (51) Bellinger, F. P.; Raman, A. V.; Rueli, R. H.; Bellinger, M. T.; Dewing, A. S.; Seale, L. A.; Andres, M. A.; Uyehara-Lock, J. H.; White, L. R.; Ross, G. W.; et al. Changes in Selenoprotein P in Substantia Nigra and Putamen in Parkinson's Disease. *J. Parkinsons. Dis.* **2012**, *2* (2), 115–126. <https://doi.org/10.3233/JPD-2012-11052>.
- (52) Abeti, R.; Uzun, E.; Renganathan, I.; Honda, T.; Pook, M. A.; Giunti, P. Targeting Lipid Peroxidation and Mitochondrial Imbalance in Friedreich's Ataxia. *Pharmacol. Res.* **2015**, *99*, 344–350. <https://doi.org/10.1016/j.phrs.2015.05.015>.
- (53) Armstrong, J. S.; Khdour, O.; Hecht, S. M. Does Oxidative Stress Contribute to the Pathology of Friedreich's Ataxia? A Radical Question. *FASEB J.* **2010**, *24* (7), 2152–2163. <https://doi.org/10.1096/fj.09-143222>.
- (54) Cong, W.; Cai, H.; Wang, R.; Daimon, C. M.; Maudsley, S.; Raber, K.; Canneva, F.; von Hörsten, S.; Martin, B. Altered Hypothalamic Protein Expression in a Rat Model of Huntington's Disease. *PLoS One* **2012**, *7* (10), e47240. <https://doi.org/10.1371/journal.pone.0047240>.
- (55) Culmsee, C.; Zhu, C.; Landshamer, S.; Becattini, B.; Wagner, E.; Pellecchia, M.; Blomgren, K.; Plesnila, N. Apoptosis-Inducing Factor Triggered by Poly(ADP-Ribose) Polymerase and Bid Mediates Neuronal Cell Death after Oxygen-Glucose Deprivation and Focal Cerebral Ischemia. *J. Neurosci.* **2005**, *25* (44), 10262–10272. <https://doi.org/10.1523/JNEUROSCI.2818-05.2005>.

- (56) Zhou, J.; Jin, Y.; Lei, Y.; Liu, T.; Wan, Z.; Meng, H.; Wang, H. Ferroptosis Is Regulated by Mitochondria in Neurodegenerative Diseases. *Neurodegener. Dis.* **2020**, *20* (1), 20–34. <https://doi.org/10.1159/000510083>.
- (57) Speer, R. E.; Karuppagounder, S. S.; Basso, M.; Sleiman, S. F.; Kumar, A.; Brand, D.; Smirnova, N.; Gazaryan, I.; Khim, S. J.; Ratan, R. R. Hypoxia-Inducible Factor Prolyl Hydroxylases as Targets for Neuroprotection by “Antioxidant” Metal Chelators: From Ferroptosis to Stroke. *Free Radic. Biol. Med.* **2013**, *62*, 26–36. <https://doi.org/10.1016/j.freeradbiomed.2013.01.026>.
- (58) Zille, M.; Karuppagounder, S. S.; Chen, Y.; Gough, P. J.; Bertin, J.; Finger, J.; Milner, T. A.; Jonas, E. A.; Ratan, R. R. Neuronal Death after Hemorrhagic Stroke in Vitro and in Vivo Shares Features of Ferroptosis and Necroptosis. *Stroke* **2017**, *48* (4), 1033–1043. <https://doi.org/10.1161/STROKEAHA.116.015609>.
- (59) Liu, Y.; Wang, W.; Li, Y.; Xiao, Y.; Cheng, J.; Jia, J. The 5-Lipoxygenase Inhibitor Zileuton Confers Neuroprotection against Glutamate Oxidative Damage by Inhibiting Ferroptosis. *Biol. Pharm. Bull.* **2015**, *38* (8), 1234–1239. <https://doi.org/10.1248/bpb.b15-00048>.
- (60) Skouta, R.; Dixon, S. J.; Wang, J.; Dunn, D. E.; Orman, M.; Shimada, K.; Rosenberg, P. A.; Lo, D. C.; Weinberg, J. M.; Linkermann, A.; et al. Ferrostatins Inhibit Oxidative Lipid Damage and Cell Death in Diverse Disease Models. *J. Am. Chem. Soc.* **2014**, *136* (12), 4551–4556. <https://doi.org/10.1021/ja411006a>.
- (61) Friedmann Angeli, J. P.; Schneider, M.; Proneth, B.; Tyurina, Y. Y.; Tyurin, V. A.; Hammond, V. J.; Herbach, N.; Aichler, M.; Walch, A.; Eggenhofer, E.; et al. Inactivation of the Ferroptosis Regulator Gpx4 Triggers Acute Renal Failure in Mice. *Nat. Cell Biol.* **2014**, *16* (12), 1180–1191. <https://doi.org/10.1038/ncb3064>.
- (62) Tan, S.; Wood, M.; Maher, P. Oxidative Stress Induces a Form of Programmed Cell Death with Characteristics of Both Apoptosis and Necrosis in Neuronal Cells. *J. Neurochem.* **1998**, *71* (1), 95–105. <https://doi.org/10.1046/j.1471-4159.1998.71010095.x>.
- (63) Yagoda, N.; Von Rechenberg, M.; Zaganjor, E.; Bauer, A. J.; Yang, W. S.; Fridman, D. J.; Wolpaw, A. J.; Smukste, I.; Peltier, J. M.; Boniface, J. J.; et al. RAS-RAF-MEK-Dependent Oxidative Cell Death Involving Voltage-Dependent Anion Channels. *Nature* **2007**, *447* (7146), 864–868. <https://doi.org/10.1038/nature05859>.
- (64) Krainz, T.; Gaschler, M. M.; Lim, C.; Sacher, J. R.; Stockwell, B. R.; Wipf, P. A Mitochondrial-Targeted Nitrooxide Is a Potent Inhibitor of Ferroptosis. *ACS Cent. Sci.* **2016**, *2* (9), 653–659. <https://doi.org/10.1021/acscentsci.6b00199>.
- (65) Youle, R. J.; Strasser, A. The BCL-2 Protein Family: Opposing Activities That Mediate Cell Death. *Nat. Rev. Mol. Cell Biol.* **2008**, *9* (1), 47–59. <https://doi.org/10.1038/nrm2308>.
- (66) Barnhart, B. C.; Alappat, E. C.; Peter, M. E. The CD95 Type I/Type II Model. *Semin. Immunol.* **2003**, *15* (3), 185–193. [https://doi.org/10.1016/S1044-5323\(03\)00031-9](https://doi.org/10.1016/S1044-5323(03)00031-9).
- (67) Shamas-Din, A.; Bindner, S.; Zhu, W.; Zaltsman, Y.; Campbell, C.; Gross, A.; Leber, B.; Andrews, D. W.; Fradin, C. TBID Undergoes Multiple Conformational Changes at the Membrane Required for Bax Activation. *J. Biol. Chem.* **2013**, *288* (30), 22111–22127. <https://doi.org/10.1074/jbc.M113.482109>.
- (68) Sun, Y. F.; Yu, L. Y.; Saarma, M.; Timmusk, T.; Arumäe, U. Neuron-Specific Bcl-2 Homology 3 Domain-Only Splice Variant of Bak Is Anti-Apoptotic in Neurons, but Pro-Apoptotic in Non-Neuronal Cells. *J. Biol. Chem.* **2001**, *276* (19), 16240–16247. <https://doi.org/10.1074/jbc.M010419200>.
- (69) Nakano, K.; Vousden, K. H. PUMA, a Novel Proapoptotic Gene, Is Induced by P53. *Mol. Cell* **2001**, *7* (3), 683–694. [https://doi.org/10.1016/S1097-2765\(01\)00214-3](https://doi.org/10.1016/S1097-2765(01)00214-3).
- (70) Li, M. The Role of P53 Up-Regulated Modulator of Apoptosis (PUMA) in Ovarian Development, Cardiovascular and Neurodegenerative Diseases. *Apoptosis*. Springer 2021. <https://doi.org/10.1007/s10495-021-01667-z>.
- (71) Puthalakath, H.; O’Reilly, L. A.; Gunn, P.; Lee, L.; Kelly, P. N.; Huntington, N. D.; Hughes, P. D.; Michalak, E. M.; McKimm-Breschkin, J.; Motoyama, N.; et al. ER Stress Triggers Apoptosis by Activating BH3-Only Protein Bim. *Cell* **2007**, *129* (7), 1337–1349. <https://doi.org/10.1016/j.cell.2007.04.027>.
- (72) Li, H.; Zhu, H.; Xu, C. J.; Yuan, J. Cleavage of BID by Caspase 8 Mediates the Mitochondrial Damage in the Fas Pathway of Apoptosis. *Cell* **1998**, *94* (4), 491–501. [https://doi.org/10.1016/S0092-8674\(00\)81590-1](https://doi.org/10.1016/S0092-8674(00)81590-1).
- (73) Letai, A.; Bassik, M. C.; Walensky, L. D.; Sorcinelli, M. D.; Weiler, S.; Korsmeyer, S. J. Distinct BH3 Domains Either Sensitize or Activate Mitochondrial Apoptosis, Serving as Prototype Cancer Therapeutics. *Cancer Cell* **2002**, *2* (3), 183–192. [https://doi.org/10.1016/S1535-6108\(02\)00127-7](https://doi.org/10.1016/S1535-6108(02)00127-7).
- (74) Willis, S. N.; Chen, L.; Dewson, G.; Wei, A.; Naik, E.; Fletcher, J. I.; Adams, J. M.; Huang, D. C. S. Proapoptotic Bak Is Sequestered by Mcl-1 and Bcl-XL, but Not Bcl-2, until Displaced by BH3-Only Proteins. *Genes Dev.* **2005**, *19* (11), 1294–1305. <https://doi.org/10.1101/gad.1304105>.
- (75) Certo, M.; Moore, V. D. G.; Nishino, M.; Wei, G.; Korsmeyer, S.; Armstrong, S. A.; Letai, A. Mitochondria Primed by Death Signals Determine Cellular Addiction to Antiapoptotic BCL-2 Family Members. *Cancer Cell* **2006**, *9* (5), 351–365. <https://doi.org/10.1016/j.ccr.2006.03.027>.
- (76) Wei, M. C.; Lindsten, T.; Mootha, V. K.; Weiler, S.; Gross, A.; Ashiya, M.; Thompson, C. B.; Korsmeyer, S. J. *TBID, a Membrane-Targeted Death Ligand, Oligomerizes BAK to Release Cytochrome C*; 2000.
- (77) Kuwana, T.; Bouchier-Hayes, L.; Chipuk, J. E.; Bonzon, C.; Sullivan, B. A.; Green, D. R.; Newmeyer, D. D. BH3 Domains of BH3-Only Proteins Differentially Regulate Bax-Mediated Mitochondrial Membrane Permeabilization Both Directly and Indirectly. *Mol. Cell* **2005**, *17* (4), 525–535. <https://doi.org/10.1016/j.molcel.2005.02.003>.
- (78) Marani, M.; Tenev, T.; Hancock, D.; Downward, J.; Lemoine, N. R. Identification of Novel Isoforms of the BH3 Domain Protein Bim Which Directly Activate Bax To Trigger Apoptosis. *Mol. Cell. Biol.* **2002**, *22* (11), 3577–3589. <https://doi.org/10.1128/mcb.22.11.3577-3589.2002>.
- (79) Kuwana, T.; Mackey, M. R.; Perkins, G.; Ellisman, M. H.; Latterich, M.; Schneider, R.; Green, D. R.; Newmeyer, D. D. Bid, Bax, and Lipids Cooperate to Form Supramolecular Openings in the Outer Mitochondrial Membrane. *Cell* **2002**, *111* (3), 331–342. [https://doi.org/10.1016/S0092-8674\(02\)01036-X](https://doi.org/10.1016/S0092-8674(02)01036-X).
- (80) Korsmeyer, S. J.; Wei, M. C.; Saito, M.; Weiler, S.; Oh, K. J.; Schlesinger, P. H. Pro-Apoptotic Cascade Activates BID, Which Oligomerizes BAK or BAX into Pores That Result in the Release of Cytochrome C. *Cell Death and Differentiation*. Cell Death Differ 2000, pp 1166–1173. <https://doi.org/10.1038/sj.cdd.4400783>.
- (81) Tait, S. W. G.; Green, D. R. Mitochondria and Cell Death: Outer Membrane Permeabilization and Beyond. *Nature Reviews Molecular Cell Biology*. Nature Publishing Group September 4, 2010, pp 621–632. <https://doi.org/10.1038/nrm2952>.
- (82) Wang, X. The Expanding Role of Mitochondria in Apoptosis. *Genes Dev.* **2001**, *15* (22), 2922–2933.
- (83) Siddiqui, W. A.; Ahad, A.; Ahsan, H. The Mystery of BCL2 Family: Bcl-2 Proteins and Apoptosis: An Update. *Arch. Toxicol.* **2015**, *89* (3), 289–317. <https://doi.org/10.1007/s00204-014-1448-7>.
- (84) Zou, H.; Li, Y.; Liu, X.; Wang, X. An APAF-1 · Cytochrome C Multimeric Complex Is a Functional Apoptosome That

References

- Activates Procaspase-9. *J. Biol. Chem.* **1999**, *274* (17), 11549–11556. <https://doi.org/10.1074/jbc.274.17.11549>.
- (85) Dargusch, R.; Piasecki, D.; Tan, S.; Liu, Y.; Schubert, D. The Role of Bax in Glutamate-Induced Nerve Cell Death. *J. Neurochem.* **2001**, *76* (1), 295–301. <https://doi.org/10.1046/j.1471-4159.2001.00035.x>.
- (86) Ochs, J. Pharmacological Inhibition and CRISPR/Cas9 Knock-out of the BCL-2 Protein BAX Exhibits Protective Effects in a Model of Glutamate-Induced Neuronal Cell Death, 2016.
- (87) Wolpaw, A. J.; Shimada, K.; Skouta, R.; Welsch, M. E.; Akavia, U. D.; Péer, D.; Shaika, F.; Bulinski, J. C.; Stockwell, B. R. Modulatory Profiling Identifies Mechanisms of Small Molecule-Induced Cell Death. *Proc. Natl. Acad. Sci. U. S. A.* **2011**, *108* (39), 771–780. <https://doi.org/10.1073/pnas.1106149108>.
- (88) Niu, X.; Brahmabhatt, H.; Mergenthaler, P.; Zhang, Z.; Sang, J.; Daude, M.; Ehlert, F. G. R.; Diederich, W. E.; Wong, E.; Zhu, W.; et al. A Small-Molecule Inhibitor of Bax and Bak Oligomerization Prevents Genotoxic Cell Death and Promotes Neuroprotection. *Cell Chem. Biol.* **2017**, *24* (4), 493–506.e5. <https://doi.org/10.1016/j.CHEMBIOL.2017.03.011>.
- (89) Pfeiffer, A.; Schneider, J.; Bueno, D.; Dolga, A.; Voss, T. D.; Lewerenz, J.; Wüllner, V.; Methner, A. Bcl-XL Knockout Attenuates Mitochondrial Respiration and Causes Oxidative Stress That Is Compensated by Pentose Phosphate Pathway Activity. *Free Radic. Biol. Med.* **2017**, *112* (August), 350–359. <https://doi.org/10.1016/j.freeradbiomed.2017.08.007>.
- (90) Lewerenz, J.; Letz, J.; Methner, A. Activation of Stimulatory Heterotrimeric G Proteins Increases Glutathione and Protects Neuronal Cells against Oxidative Stress. *J. Neurochem.* **2003**, *87* (2), 522–531. <https://doi.org/10.1046/j.1471-4159.2003.02019.x>.
- (91) Gascón, S.; Murenu, E.; Masserdotti, G.; Ortega, F.; Russo, G. L.; Petrik, D.; Deshpande, A.; Heinrich, C.; Karow, M.; Robertson, S. P.; et al. Identification and Successful Negotiation of a Metabolic Checkpoint in Direct Neuronal Reprogramming. *Cell Stem Cell* **2016**, *18* (3), 396–409. <https://doi.org/10.1016/j.stem.2015.12.003>.
- (92) Sahin, M.; Saxena, A.; Joost, P.; Lewerenz, J.; Methner, A. Induction of Bcl-2 by Functional Regulation of G-Protein Coupled Receptors Protects from Oxidative Glutamate Toxicity by Increasing Glutathione. *Free Radic. Res.* **2006**, *40* (11), 1113–1123. <https://doi.org/10.1080/10715760600838191>.
- (93) Voehringer, D. W.; Meyn, R. E. Redox Aspects of Bcl-2 Function. *Antioxid. Redox Signal.* **2000**, *2* (3), 537–550. <https://doi.org/10.1089/15230860050192314>.
- (94) Chou, J. J.; Li, H.; Salvesen, G. S.; Yuan, J.; Wagner, G. Solution Structure of BID, an Intracellular Amplifier of Apoptotic Signaling. *Cell* **1999**, *96* (5), 615–624. [https://doi.org/10.1016/S0092-8674\(00\)80572-3](https://doi.org/10.1016/S0092-8674(00)80572-3).
- (95) McDonnell, J. M.; Fushman, D.; Milliman, C. L.; Korsmeyer, S. J.; Cowburn, D. *Solution Structure of the Proapoptotic Molecule BID: A Structural Basis for Apoptotic Agonists and Antagonists*; 1999; Vol. 96.
- (96) Billen, L. P.; Shamas-Din, A.; Andrews, D. W. Bid: A Bax-like BH3 Protein. *Oncogene* **2008**, *27*, S93–S104. <https://doi.org/10.1038/onc.2009.47>.
- (97) Zha, J.; Weiler, S.; Oh, K. J.; Wei, M. C.; Korsmeyer, S. J. Posttranslational N-Myristoylation of BID as a Molecular Switch for Targeting Mitochondria and Apoptosis. *Science* **2000**, *290* (5497), 1761–1765. <https://doi.org/10.1126/science.290.5497.1761>.
- (98) Holcomb, J.; Spellmon, N.; Zhang, Y.; Doughan, M.; Li, C.; Yang, Z.; Medicine, T. Crystallography. **2017**, *4* (4), 557–575. <https://doi.org/10.3934/biophy.2017.4.557>. Protein.
- (99) Oppermann, S. Targeting Bid for Mitoprotection - Bid Crystallization, New Mechanisms and Inhibitory Compounds, University of Marburg, 2014.
- (100) Jelinek, A. A Key Role for BID-Mediated Mitochondrial Damage in Oxidative Cell Death, University of Marburg, 2018.
- (101) Gross, A.; Yin, X. M.; Wang, K.; Wei, M. C.; Jockel, J.; Milliman, C.; Erdjument-Bromage, H.; Tempst, P.; Korsmeyer, S. J. Caspase Cleaved BID Targets Mitochondria and Is Required for Cytochrome c Release, While BCL-X(L) Prevents This Release but Not Tumor Necrosis Factor-R1/Fas Death. *J. Biol. Chem.* **1999**, *274* (2), 1156–1163. <https://doi.org/10.1074/jbc.274.2.1156>.
- (102) Desagher, S.; Osen-Sand, A.; Montessuit, S.; Magnenat, E.; Vilbois, F.; Hochmann, A.; Journot, L.; Antonsson, B.; Martinou, J. C. Phosphorylation of Bid by Casein Kinases I and II Regulates Its Cleavage by Caspase 8. *Mol. Cell* **2001**, *8* (3), 601–611. [https://doi.org/10.1016/S1097-2765\(01\)00335-5](https://doi.org/10.1016/S1097-2765(01)00335-5).
- (103) Wang, K.; Yin, X. M.; Chao, D. T.; Milliman, C. L.; Korsmeyer, S. J. BID: A Novel BH3 Domain-Only Death Agonist. *Genes Dev.* **1996**, *10* (22), 2859–2869. <https://doi.org/10.1101/gad.10.22.2859>.
- (104) Kim, T.-H.; Zhao, Y.; Ding, W.-X.; Shin, J. N.; He, X.; Seo, Y.-W.; Chen, J.; Rabinowich, H.; Amoscato, A. A.; Yin, X.-M. Bid-Cardiolipin Interaction at Mitochondrial Contact Site Contributes to Mitochondrial Cristae Reorganization and Cytochrome C Release. *Mol. Biol. Cell* **2004**, *15* (7), 3061–3072. <https://doi.org/10.1091/mbc.e03-12-0864>.
- (105) Lovell, J. F.; Billen, L. P.; Bindner, S.; Shamas-Din, A.; Fradin, C.; Leber, B.; Andrews, D. W. Membrane Binding by TBid Initiates an Ordered Series of Events Culminating in Membrane Permeabilization by Bax. *Cell* **2008**, *135* (6), 1074–1084. <https://doi.org/10.1016/j.cell.2008.11.010>.
- (106) Gonzalez, F.; Pariselli, F.; Jalmar, O.; Dupaigne, P.; Sureau, F.; Dellinger, M.; Hendrickson, E. A.; Bernard, S.; Petit, P. X. Mechanistic Issues of the Interaction of the Hairpin-Forming Domain of TBid with Mitochondrial Cardiolipin. *PLoS One* **2010**, *5* (2), e9342. <https://doi.org/10.1371/journal.pone.0009342>.
- (107) Gonzalez, F.; Pariselli, F.; Dupaigne, P.; Budihardjo, I.; Lutter, M.; Antonsson, B.; Dirolez, P.; Manon, S.; Martinou, J. C.; Goubern, M.; et al. TBid Interaction with Cardiolipin Primarily Orchestrates Mitochondrial Dysfunctions and Subsequently Activates Bax and Bak. *Cell Death Differ.* **2005**, *12* (6), 614–626. <https://doi.org/10.1038/sj.cdd.4401571>.
- (108) Zaltsman, Y.; Shachnai, L.; Yivgi-Ohana, N.; Schwarz, M.; Maryanovich, M.; Houtkooper, R. H.; Vaz, F. M.; De Leonardis, F.; Fiermonte, G.; Palmieri, F.; et al. MTCH2/MIMP Is a Major Facilitator of TBid Recruitment to Mitochondria. *Nat. Cell Biol.* **2010**, *12* (6), 553–562. <https://doi.org/10.1038/ncb2057>.
- (109) Manara, A.; Lindsay, J.; Marchioreto, M.; Astegno, A.; P. Gilmore, A.; Esposti, M. D.; Crimi, M. Bid Binding to Negatively Charged Phospholipids May Not Be Required for Its Pro-Apoptotic Activity in Vivo. *Biochim. Biophys. Acta - Mol. Cell Biol. Lipids* **2009**, *1791* (10), 997–1010. <https://doi.org/10.1016/j.bbalip.2009.05.003>.
- (110) Cogliati, S.; Scorrano, L. A BID on Mitochondria with MTCH2. *Cell Res.* **2010**, *20* (8), 863–865. <https://doi.org/10.1038/cr.2010.100>.
- (111) Tan, C. T.; Zhou, Q. L.; Su, Y. C.; Fu, N. Y.; Chang, H. C.; Tao, R. N.; Sukumaran, S. K.; Baksh, S.; Tan, Y. J.; Sabapathy, K.; et al. MOAP-1 Mediates Fas-Induced Apoptosis in Liver by Facilitating TBid Recruitment to Mitochondria. *Cell Rep.* **2016**, *16* (1), 174–185. <https://doi.org/10.1016/j.celrep.2016.05.068>.

- (112) Esposti, M. D.; Erler, J. T.; Hickman, J. A.; Dive, C. Bid, a Widely Expressed Proapoptotic Protein of the Bcl-2 Family, Displays Lipid Transfer Activity. *Mol. Cell. Biol.* **2001**, *21* (21), 7268–7276. <https://doi.org/10.1128/MCB.21.21.7268-7276.2001>.
- (113) Higuchi, H.; Miyoshi, H.; Bronk, S. F.; Zhang, H.; Dean, N.; Gores, G. J. Bid Antisense Attenuates Bile Acid-Induced Apoptosis and Cholestatic Liver Injury. *J. Pharmacol. Exp. Ther.* **2001**, *299* (3), 866–873.
- (114) Tafani, M.; Karpnich, N. O.; Hurster, K. A.; Pastorino, J. G.; Schneider, T.; Russo, M. A.; Farber, J. L. Cytochrome c Release upon Fas Receptor Activation Depends on Translocation of Full-Length Bid and the Induction of the Mitochondrial Permeability Transition. *J. Biol. Chem.* **2002**, *277* (12), 10073–10082. <https://doi.org/10.1074/jbc.M111350200>.
- (115) Eskes, R.; Desagher, S.; Antonsson, B.; Martinou, J.-C. Bid Induces the Oligomerization and Insertion of Bax into the Outer Mitochondrial Membrane. *Mol. Cell. Biol.* **2000**, *20* (3), 929–935. <https://doi.org/10.1128/mcb.20.3.929-935.2000>.
- (116) Scorrano, L.; Ashiya, M.; Buttle, K.; Weiler, S.; Oakes, S. A.; Mannella, C. A.; Korsmeyer, S. J. A Distinct Pathway Remodels Mitochondrial Cristae and Mobilizes Cytochrome c during Apoptosis. *Dev. Cell* **2002**, *2* (1), 55–67. [https://doi.org/10.1016/S1534-5807\(01\)00116-2](https://doi.org/10.1016/S1534-5807(01)00116-2).
- (117) Frezza, C.; Cipolat, S.; Martins de Brito, O.; Micaroni, M.; Beznoussenko, G. V.; Rudka, T.; Bartoli, D.; Polishuck, R. S.; Danial, N. N.; De Strooper, B.; et al. OPA1 Controls Apoptotic Cristae Remodeling Independently from Mitochondrial Fusion. *Cell* **2006**, *126* (1), 177–189. <https://doi.org/10.1016/j.cell.2006.06.025>.
- (118) Shimizu, S.; Tsujimoto, Y. Proapoptotic BH3-Only Bcl-2 Family Members Induce Cytochrome c Release, but Not Mitochondrial Membrane Potential Loss, and Do Not Directly Modulate Voltage-Dependent Anion Channel Activity. *Proc. Natl. Acad. Sci. U. S. A.* **2000**, *97* (2), 577–582. <https://doi.org/10.1073/pnas.97.2.577>.
- (119) Rostovtseva, T. K.; Antonsson, B.; Suzuki, M.; Youle, R. J.; Colombini, M.; Bezrukov, S. M. Bid, but Not Bax, Regulates VDAC Channels. *J. Biol. Chem.* **2004**, *279* (14), 13575–13583. <https://doi.org/10.1074/jbc.M310593200>.
- (120) Shoshan-Barmatz, V.; De Pinto, V.; Zweckstetter, M.; Raviv, Z.; Keinan, N.; Arbel, N. VDAC, a Multi-Functional Mitochondrial Protein Regulating Cell Life and Death. *Molecular Aspects of Medicine*. Pergamon June 1, 2010, pp 227–285. <https://doi.org/10.1016/j.mam.2010.03.002>.
- (121) Shoshan-Barmatz, V.; De, S.; Meir, A. The Mitochondrial Voltage-Dependent Anion Channel 1, Ca²⁺ Transport, Apoptosis, and Their Regulation. *Front. Oncol.* **2017**, *7* (APR). <https://doi.org/10.3389/fonc.2017.00060>.
- (122) Rostovtseva, T. K.; Tan, W.; Colombini, M. On the Role of VDAC in Apoptosis: Fact and Fiction. *Journal of Bioenergetics and Biomembranes*. June 2005, pp 129–142. <https://doi.org/10.1007/s10863-005-6566-8>.
- (123) Schendel, S. L.; Azimov, R.; Pawłowski, K.; Godzik, A.; Kagan, B. L.; Reed, J. C. Ion Channel Activity of the BH3 Only Bcl-2 Family Member, BID. *J. Biol. Chem.* **1999**, *274* (31), 21932–21936. <https://doi.org/10.1074/jbc.274.31.21932>.
- (124) Gahl, R. F.; Dwivedi, P.; Tjandra, N. Bcl-2 Proteins Bid and Bax Form a Network to Permeabilize the Mitochondria at the Onset of Apoptosis. *Cell Death Dis.* **2016**, *7* (10), e2424. <https://doi.org/10.1038/cddis.2016.320>.
- (125) Grinberg, M.; Sarig, R.; Zaltsman, Y.; Frumkin, D.; Grammatikakis, N.; Reuveny, E.; Gross, A. TBID Homooligomerizes in the Mitochondrial Membrane to Induce Apoptosis*. **2002**. <https://doi.org/10.1074/jbc.M104893200>.
- (126) Esposti, M. D. The Roles of Bid. *Apoptosis* **2002**, *7* (5), 433–440. <https://doi.org/10.1023/A:1020035124855>.
- (127) Ding, W. X.; Ni, H. M.; DiFrancesca, D.; Stolz, D. B.; Yin, X. M. Bid-Dependent Generation of Oxygen Radicals Promotes Death Receptor Activation-Induced Apoptosis in Murine Hepatocytes. *Hepatology* **2004**, *40* (2), 403–413. <https://doi.org/10.1002/hep.20310>.
- (128) Garcia-Perez, C.; Roy, S. S.; Naghdi, S.; Lin, X.; Davies, E.; Hajnóczky, G. Bid-Induced Mitochondrial Membrane Permeabilization Waves Propagated by Local Reactive Oxygen Species (ROS) Signaling. *Proc. Natl. Acad. Sci. U. S. A.* **2012**, *109* (12), 4497–4502. <https://doi.org/10.1073/pnas.1118244109>.
- (129) Krajewska, M.; Mai, J. K.; Zapata, J. M.; Ashwell, K. W.; Schendel, S. L.; Reed, J. C.; Krajewski, S. Dynamics of Expression of Apoptosis-Regulatory Proteins Bid, Bcl-2, Bcl-X, Bax and Bak during Development of Murine Nervous System. *Cell Death Differ.* **2002**, *9* (2), 145–157. <https://doi.org/10.1038/sj/cdd/4400934>.
- (130) Plesnila, N.; Zinkel, S.; Le, D. A.; Amin-Hanjani, S.; Wu, Y.; Qiu, J.; Chiarugi, A.; Thomas, S. S.; Kohane, D. S.; Korsmeyer, S. J.; et al. BID Mediates Neuronal Cell Death after Oxygen/ Glucose Deprivation and Focal Cerebral Ischemia. *Proc. Natl. Acad. Sci.* **2001**, *98* (26), 15318–15323. <https://doi.org/10.1073/pnas.261323298>.
- (131) Yin, X.-M.; Luo, Y.; Cao, G.; Bai, L.; Pei, W.; Kuharsky, D. K.; Chen, J. Bid-Mediated Mitochondrial Pathway Is Critical to Ischemic Neuronal Apoptosis and Focal Cerebral Ischemia. *J. Biol. Chem.* **2002**, *277* (44), 42074–42081. <https://doi.org/10.1074/jbc.M204991200>.
- (132) Bermppohl, D.; You, Z.; Korsmeyer, S. J.; Moskowitz, M. A.; Whalen, M. J. Traumatic Brain Injury in Mice Deficient in Bid: Effects on Histopathology and Functional Outcome. *J. Cereb. Blood Flow Metab.* **2006**, *26*, 625–633. <https://doi.org/10.1038/sj.jcbfm.9600258>.
- (133) Ward, M. W.; Rehm, M.; Duessmann, H.; Kacmar, S.; Concannon, C. G.; Prehn, J. H. M. Real Time Single Cell Analysis of Bid Cleavage and Bid Translocation during Caspase-Dependent and Neuronal Caspase-Independent Apoptosis. *J. Biol. Chem.* **2006**, *281* (9), 5837–5844. <https://doi.org/10.1074/jbc.M511562200>.
- (134) König, H. G.; Rehm, M.; Gudorf, D.; Krajewski, S.; Gross, A.; Ward, M. W.; Prehn, J. H. M. Full Length Bid Is Sufficient to Induce Apoptosis of Cultured Rat Hippocampal Neurons. *BMC Cell Biol.* **2007**, *8*, 1–8. <https://doi.org/10.1186/1471-2121-8-7>.
- (135) Zhu, C.; Qiu, L.; Wang, X.; Hallin, U.; Candé, C.; Kroemer, G.; Hagberg, H.; Blomgren, K. Involvement of Apoptosis-Inducing Factor in Neuronal Death after Hypoxia-Ischemia in the Neonatal Rat Brain. *J. Neurochem.* **2003**, *86* (2), 306–317. <https://doi.org/10.1046/j.1471-4159.2003.01832.x>.
- (136) Plesnila, N.; Zhu, C.; Culmsee, C.; Gröger, M.; Moskowitz, M. A.; Blomgren, K. Nuclear Translocation of Apoptosis-Inducing Factor after Focal Cerebral Ischemia. *J. Cereb. Blood Flow Metab.* **2004**, *24* (4), 458–466. <https://doi.org/10.1097/00004647-200404000-00011>.
- (137) Neitemeier, S.; Dolga, A. M.; Honrath, B.; Karuppagounder, S. S.; Alim, I.; Ratan, R. R.; Culmsee, C. Inhibition of HIF-Prolyl-4-Hydroxylases Prevents Mitochondrial Impairment and Cell Death in a Model of Neuronal Oxytosis. *Cell Death Dis.* **2016**, *7* (5), e2214. <https://doi.org/10.1038/cddis.2016.107>.
- (138) Grohm, J.; Plesnila, N.; Culmsee, C. Bid Mediates Fission, Membrane Permeabilization and Peri-Nuclear Accumulation of Mitochondria as a Prerequisite for Oxidative Neuronal Cell Death. *Brain. Behav. Immun.* **2010**, *24* (5), 831–838. <https://doi.org/10.1016/j.bbi.2009.11.015>.

References

- (139) Degli Esposti, M. Sequence and Functional Similarities between Pro-Apoptotic Bid and Plant Lipid Transfer Proteins. *Biochim. Biophys. Acta - Bioenerg.* **2002**, *1553* (3), 331–340. [https://doi.org/10.1016/S0005-2728\(02\)00187-1](https://doi.org/10.1016/S0005-2728(02)00187-1).
- (140) Becattini, B.; Sareth, S.; Zhai, D.; Crowell, K. J.; Leone, M.; Reed, J. C.; Pellecchia, M. Targeting Apoptosis via Chemical Design: Inhibition of Bid-Induced Cell Death by Small Organic Molecules. *Chem. Biol.* **2004**, *11* (8), 1107–1117. <https://doi.org/10.1016/J.CHEMBIOL.2004.05.022>.
- (141) Becattini, B.; Culmsee, C.; Leone, M.; Zhai, D.; Zhang, X.; Crowell, K. J.; Rega, M. F.; Landshamer, S.; Reed, J. C.; Plesnila, N.; et al. Structure-Activity Relationships by Interligand NOE-Based Design and Synthesis of Antiapoptotic Compounds Targeting Bid. *Proc. Natl. Acad. Sci.* **2006**, *103* (33), 12602–12606. <https://doi.org/10.1073/pnas.0603460103>.
- (142) Grohm, J.; Kim, S.-W.; Mamrak, U.; Tobaben, S.; Cassidy-Stone, A.; Nunnari, J.; Plesnila, N.; Culmsee, C. Inhibition of Drp1 Provides Neuroprotection in Vitro and in Vivo. *Cell Death Differ.* **2012**, *19* (9), 1446–1458. <https://doi.org/10.1038/cdd.2012.18>.
- (143) Anguissola, S.; Köhler, B.; O'Byrne, R.; Dössmann, H.; Cannon, M. D.; Murray, F. E.; Concannon, C. G.; Rehm, M.; Kögel, D.; Prehn, J. H. M. Bid and Calpains Cooperate to Trigger Oxaliplatin-Induced Apoptosis of Cervical Carcinoma HeLa Cells. *Mol. Pharmacol.* **2009**, *76* (5), 998–1010. <https://doi.org/10.1124/mol.109.058156>.
- (144) Köhler, B.; Anguissola, S.; Concannon, C. G.; Rehm, M.; Kögel, D.; Prehn, J. H. M. Bid Participates in Genotoxic Drug-Induced Apoptosis of HeLa Cells and Is Essential for Death Receptor Ligands' Apoptotic and Synergistic Effects. *PLoS One* **2008**, *3* (7), e2844. <https://doi.org/10.1371/journal.pone.0002844>.
- (145) Barho, M. T.; Oppermann, S.; Schrader, F. C.; Degenhardt, I.; Elsässer, K.; Wegscheid-Gerlach, C.; Culmsee, C.; Schlitzer, M. N -Acyl Derivatives of 4-Phenoxyaniline as Neuroprotective Agents. *ChemMedChem* **2014**, *9* (10), 2260–2273. <https://doi.org/10.1002/cmdc.201402195>.
- (146) Oppermann, S.; Schrader, F. C.; Elsässer, K.; Dolga, A. M.; Kraus, A. L.; Doti, N.; Wegscheid-Gerlach, C.; Schlitzer, M.; Culmsee, C. Novel N-Phenyl-Substituted Thiazolidinediones Protect Neural Cells against Glutamate- and TBid-Induced Toxicity. *J. Pharmacol. Exp. Ther.* **2014**, *350* (2), 273–289. <https://doi.org/10.1124/jpet.114.213777>.
- (147) Pfaff, A. L. Synthese Potentiell Neuroprotektiver Wirkstoffe Basierend Auf Heterozyklischen Grundstrukturen, Marburg, 2019.
- (148) Pratt, D. A.; DiLabio, G. A.; Valgimigli, L.; Pedulli, G. F.; Ingold, K. U. Substituent Effects on the Bond Dissociation Enthalpies of Aromatic Amines. *J. Am. Chem. Soc.* **2002**, *124* (37), 11085–11092. <https://doi.org/10.1021/ja026289x>.
- (149) Zilka, O.; Shah, R.; Li, B.; Friedmann Angeli, J. P.; Griesser, M.; Conrad, M.; Pratt, D. A. On the Mechanism of Cytoprotection by Ferrostatin-1 and Liprostatin-1 and the Role of Lipid Peroxidation in Ferroptotic Cell Death. *ACS Cent. Sci.* **2017**, *3* (3), 232–243. <https://doi.org/10.1021/acscentsci.7b00028>.
- (150) Morimoto, B. H.; Koshland, D. E. Excitatory Amino Acid Uptake and N-Methyl-D-Aspartate-Mediated Secretion in a Neural Cell Line. *Proc. Natl. Acad. Sci. U. S. A.* **1990**, *87* (9), 3518–3521. <https://doi.org/10.1073/pnas.87.9.3518>.
- (151) Davis, J. B.; Maher, P. Protein Kinase C Activation Inhibits Glutamate-Induced Cytotoxicity in a Neuronal Cell Line. *Brain Res.* **1994**, *652* (1), 169–173. [https://doi.org/10.1016/0006-8993\(94\)90334-4](https://doi.org/10.1016/0006-8993(94)90334-4).
- (152) Berridge, M. V.; Tan, A. S. Characterization of the Cellular Reduction of 3-(4,5-Dimethylthiazol-2-Yl)-2,5-Diphenyltetrazolium Bromide (MTT): Subcellular Localization, Substrate Dependence, and Involvement of Mitochondrial Electron Transport in MTT Reduction. *Arch. Biochem. Biophys.* **1993**, *303* (2), 474–482. <https://doi.org/10.1006/abbi.1993.1311>.
- (153) Diemert, S.; Dolga, A. M.; Tobaben, S.; Grohm, J.; Pfeifer, S.; Oexler, E.; Culmsee, C. Impedance Measurement for Real Time Detection of Neuronal Cell Death. *J. Neurosci. Methods* **2012**, *203* (1), 69–77. <https://doi.org/10.1016/j.jneumeth.2011.09.012>.
- (154) Mailloux, R. J. Teaching the Fundamentals of Electron Transfer Reactions in Mitochondria and the Production and Detection of Reactive Oxygen Species. *Redox Biology*. Elsevier B.V. April 1, 2015, pp 381–398. <https://doi.org/10.1016/j.redox.2015.02.001>.
- (155) Schmitt, S.; Eberhagen, C.; Weber, S.; Aichler, M.; Zischka, H. Isolation of Mitochondria from Cultured Cells and Liver Tissue Biopsies for Molecular and Biochemical Analyses; 2015; pp 87–97. https://doi.org/10.1007/978-1-4939-2550-6_8.
- (156) Rogers, G.; Murphy, A.; Elorza, A.; Brand, M. Analyzing Microgram Quantities of Isolated Mitochondria in the XF24 Analyzer. *Nat. Methods | Appl. Notes* **2012**.
- (157) Bioinformatics and Molecular Design Research Bioinformatics Center. PreADMET Program. **2004**, Seoul, South Korea.
- (158) Cheng, F.; Li, W.; Zhou, Y.; Shen, J.; Wu, Z.; Liu, G.; Lee, P. W.; Tang, Y. AdmetSAR: A Comprehensive Source and Free Tool for Assessment of Chemical ADMET Properties. *J. Chem. Inf. Model.* **2012**, *52* (11), 3099–3105. <https://doi.org/10.1021/ci300367a>.
- (159) Bergfors, T. M. *Protein Crystallization-Second Edition*; 2009.
- (160) Jerabek-Willemsen, M.; André, T.; Wanner, R.; Roth, H. M.; Duhr, S.; Baaske, P.; Breitsprecher, D. MicroScale Thermophoresis: Interaction Analysis and Beyond. *J. Mol. Struct.* **2014**, *1077*, 101–113. <https://doi.org/10.1016/j.molstruc.2014.03.009>.
- (161) Michels, S.; Dolga, A. M.; Braun, M. D.; Kisko, T. M.; Sungur, A. Ö.; Witt, S. H.; Rietschel, M.; Dempfle, A.; Wöhr, M.; Schwarting, R. K. W.; et al. Interaction of the Psychiatric Risk Gene *Cacna1c* With Post-Weaning Social Isolation or Environmental Enrichment Does Not Affect Brain Mitochondrial Bioenergetics in Rats. *Front. Cell. Neurosci.* **2019**, *13*, 483. <https://doi.org/10.3389/fncel.2019.00483>.
- (162) Brand, M. D.; Nicholls, D. G. Assessing Mitochondrial Dysfunction in Cells. *Biochem. J.* **2011**, *435* (2), 297–312. <https://doi.org/10.1042/BJ20110162>.
- (163) Kang, S. M.; Cha, S. H.; Ko, J. Y.; Kang, M. C.; Kim, D.; Heo, S. J.; Kim, J. S.; Heu, M. S.; Kim, Y. T.; Jung, W. K.; et al. Neuroprotective Effects of Phlorotannins Isolated from a Brown Alga, *Ecklonia Cava*, against H₂O₂-Induced Oxidative Stress in Murine Hippocampal HT22 Cells. *Environ. Toxicol. Pharmacol.* **2012**, *34* (1), 96–105. <https://doi.org/10.1016/j.etap.2012.03.006>.
- (164) Rabenau, M.; Unger, M.; Drewe, J.; Culmsee, C. Metabolic Switch Induced by *Cimicifuga Racemosa* Extract Prevents Mitochondrial Damage and Oxidative Cell Death. *Phytomedicine* **2019**, *52*, 107–116. <https://doi.org/10.1016/j.phymed.2018.09.177>.
- (165) Feigin, V. L.; Nichols, E.; Alam, T.; Bannick, M. S.; Beghi, E.; Blake, N.; Culpepper, W. J.; Dorsey, E. R.; Elbaz, A.;

- Ellenbogen, R. G.; et al. Global, Regional, and National Burden of Neurological Disorders, 1990–2016: A Systematic Analysis for the Global Burden of Disease Study 2016. *Lancet Neurol.* **2019**, *18* (5), 459–480. [https://doi.org/10.1016/S1474-4422\(18\)30499-X](https://doi.org/10.1016/S1474-4422(18)30499-X).
- (166) Organization, W. H. The top 10 causes of death.
- (167) Chen, X.; Pan, W. The Treatment Strategies for Neurodegenerative Diseases by Integrative Medicine. *Integr. Med. Int.* **2015**, *1* (4), 223–225. <https://doi.org/10.1159/000381546>.
- (168) Denisov, A. Y.; Chen, G.; Sprules, T.; Moldoveanu, T.; Beauparlant, P.; Gehring, K. Structural Model of the BCL-w-BID Peptide Complex and Its Interactions with Phospholipid Micelles. *Biochemistry* **2006**, *45* (7), 2250–2256. <https://doi.org/10.1021/bi052332s>.
- (169) Smits, C.; Czabotar, P. E.; Hinds, M. G.; Day, C. L. Structural Plasticity Underpins Promiscuous Binding of the Prosurvival Protein A1. *Structure* **2008**, *16* (5), 818–829. <https://doi.org/10.1016/j.str.2008.02.009>.
- (170) Czabotar, P. E.; Westphal, D.; Dewson, G.; Ma, S.; Hockings, C.; Fairlie, W. D.; Lee, E. F.; Yao, S.; Robin, A. Y.; Smith, B. J.; et al. Bax Crystal Structures Reveal How BH3 Domains Activate Bax and Nucleate Its Oligomerization to Induce Apoptosis. *Cell* **2013**, *152* (3), 519–531. <https://doi.org/10.1016/j.cell.2012.12.031>.
- (171) Robin, A. Y.; Krishna Kumar, K.; Westphal, D.; Wardak, A. Z.; Thompson, G. V.; Dewson, G.; Colman, P. M.; Czabotar, P. E. Crystal Structure of Bax Bound to the BH3 Peptide of Bim Identifies Important Contacts for Interaction. *Cell Death Dis.* **2015**, *6* (7), e1809-9. <https://doi.org/10.1038/cddis.2015.141>.
- (172) Oh, K. J.; Barbuto, S.; Meyer, N.; Kim, R.-S.; Collier, R. J.; Korsmeyer, S. J. Conformational Changes in BID, a pro-Apoptotic BCL-2 Family Member, upon Membrane Binding. A Site-Directed Spin Labeling Study. *J. Biol. Chem.* **2005**, *280* (1), 753–767. <https://doi.org/10.1074/jbc.M405428200>.
- (173) Lutter, M.; Fang, M.; Luo, X.; Nishijima, M.; Xie, X. S.; Wang, X. Cardiolipin Provides Specificity for Targeting of TBid to Mitochondria. *Nat. Cell Biol.* **2000**, *2* (10), 754–756. <https://doi.org/10.1038/35036395>.
- (174) Katz, C.; Zaltsman-Amir, Y.; Mostizky, Y.; Kollet, N.; Gross, A.; Friedler, A. Molecular Basis of the Interaction between Proapoptotic Truncated BID (TBID) Protein and Mitochondrial Carrier Homologue 2 (MTCH2) Protein: Key Players in Mitochondrial Death Pathway. *J. Biol. Chem.* **2012**, *287* (18), 15016–15023. <https://doi.org/10.1074/jbc.M111.328377>.
- (175) Liu, J.; Weiss, A.; Durrant, D.; Chi, N. W.; Lee, R. M. The Cardiolipin-Binding Domain of Bid Affects Mitochondrial Respiration and Enhances Cytochrome c Release. *Apoptosis* **2004**, *9* (5), 533–541. <https://doi.org/10.1023/B:APPT.0000038034.16230.ea>.
- (176) Souers, A. J.; Levenson, J. D.; Boghaert, E. R.; Ackler, S. L.; Catron, N. D.; Chen, J.; Dayton, B. D.; Ding, H.; Enschede, S. H.; Fairbrother, W. J.; et al. ABT-199, a Potent and Selective BCL-2 Inhibitor, Achieves Antitumor Activity While Sparing Platelets. *Nat. Med.* **2013**, *19* (2), 202–208. <https://doi.org/10.1038/nm.3048>.
- (177) Stewart, M. L.; Fire, E.; Keating, A. E.; Walensky, L. D. The MCL-1 BH3 Helix Is an Exclusive MCL-1 Inhibitor and Apoptosis Sensitizer. *Nat. Chem. Biol.* **2010**, *6* (8), 595–601. <https://doi.org/10.1038/nchembio.391>.
- (178) Lessene, G.; Czabotar, P. E.; Sleebs, B. E.; Zobel, K.; Lowes, K. N.; Adams, J. M.; Baell, J. B.; Colman, P. M.; Deshayes, K.; Fairbrother, W. J.; et al. Structure-Guided Design of a Selective BCL-XL Inhibitor. *Nat. Chem. Biol.* **2013**, *9* (6), 390–397. <https://doi.org/10.1038/nchembio.1246>.
- (179) Zhou, H.; Aguilar, A.; Chen, J.; Bai, L.; Liu, L.; Meagher, J. L.; Yang, C.-Y.; McEachern, D.; Cong, X.; Stuckey, J. A.; et al. Structure-Based Design of Potent Bcl-2/Bcl-XL Inhibitors with Strong in Vivo Antitumor Activity. *J. Med. Chem.* **2012**, *55* (13), 6149–6161. <https://doi.org/10.1021/jm300608w>.
- (180) Krishna, S.; Kumar, S. B.; Murthy, T. P. K.; Murahari, M. Structure-Based Design Approach of Potential BCL-2 Inhibitors for Cancer Chemotherapy. *Comput. Biol. Med.* **2021**, *134*, 104455. <https://doi.org/10.1016/j.compbiomed.2021.104455>.
- (181) Ni, H. M.; Baty, C. J.; Li, N.; Ding, W. X.; Gao, W.; Li, M.; Chen, X.; Ma, J.; Michalopoulos, G. K.; Yin, X. M. Bid Agonist Regulates Murine Hepatocyte Proliferation by Controlling Endoplasmic Reticulum Calcium Homeostasis. *Hepatology* **2010**, *52* (1), 338–348. <https://doi.org/10.1002/hep.23672>.
- (182) Scapin, G. Molecular Replacement Then and Now. *Acta Crystallogr. Sect. D Biol. Crystallogr.* **2013**, *69* (11), 2266–2275. <https://doi.org/10.1107/S0907444913011426>.
- (183) Mao, B.; Guan, R.; Montelione, G. T. Improved Technologies Now Routinely Provide Protein NMR Structures Useful for Molecular Replacement. *Structure* **2011**, *19* (6), 757–766. <https://doi.org/10.1016/j.str.2011.04.005>.
- (184) Derewenda, Z. S. Application of Protein Engineering to Enhance Crystallizability and Improve Crystal Properties. *Acta Crystallogr. D. Biol. Crystallogr.* **2010**, *66* (Pt 5), 604–615. <https://doi.org/10.1107/S090744491000644X>.
- (185) Goldschmidt, L.; Cooper, D. R.; Derewenda, Z. S.; Eisenberg, D. Toward Rational Protein Crystallization: A Web Server for the Design of Crystallizable Protein Variants. *Protein Sci.* **2007**, *16* (8), 1569–1576. <https://doi.org/10.1110/ps.072914007>.
- (186) Conrad, M.; Pratt, D. A. The Chemical Basis of Ferroptosis. *Nat. Chem. Biol.* **2019**, *15* (12), 1137–1147. <https://doi.org/10.1038/s41589-019-0408-1>.
- (187) Sugihara, T.; Rao, G.; Hebbel, R. P. Diphenylamine: An Unusual Antioxidant. *Free Radic. Biol. Med.* **1993**, *14* (4), 381–387. [https://doi.org/10.1016/0891-5849\(93\)90087-B](https://doi.org/10.1016/0891-5849(93)90087-B).
- (188) Skouta, R.; Dixon, S. J.; Wang, J.; Dunn, D. E.; Orman, M.; Shimada, K.; Rosenberg, P. A.; Lo, D. C.; Weinberg, J. M.; Linkermann, A.; et al. Ferrostatins Inhibit Oxidative Lipid Damage and Cell Death in Diverse Disease Models. **2014**. <https://doi.org/10.1021/ja411006a>.
- (189) Jiang, T.; Chu, J.; Chen, H.; Cheng, H.; Su, J.; Wang, X.; Cao, Y.; Tian, S.; Li, Q. Gastrodin Inhibits H₂O₂-Induced Ferroptosis through Its Antioxidative Effect in Rat Glioma Cell Line C6. *Biol. Pharm. Bull.* **2020**, *43* (3), 480–487. <https://doi.org/10.1248/bpb.b19-00824>.
- (190) Battaglia, A. M.; Chirillo, R.; Aversa, I.; Sacco, A.; Costanzo, F.; Biamonte, F. Ferroptosis and Cancer: Mitochondria Meet the “Iron Maiden” Cell Death. *Cells* **2020**, *9* (6), 1–26. <https://doi.org/10.3390/cells9061505>.
- (191) Knott, A. B.; Perkins, G.; Schwarzenbacher, R.; Bossy-Wetzel, E. Mitochondrial Fragmentation in Neurodegeneration. *Nat. Rev. Neurosci.* **2008**, *9* (7), 505–518. <https://doi.org/10.1038/nrn2417>.
- (192) Smith, R. A. J.; Murphy, M. P. Animal and Human Studies with the Mitochondria-Targeted Antioxidant MitoQ. In *Annals of the New York Academy of Sciences*; Blackwell Publishing Inc., 2010; Vol. 1201, pp 96–103. <https://doi.org/10.1111/j.1749-6632.2010.05627.x>.
- (193) Masubuchi, Y.; Yamada, S.; Horie, T. Diphenylamine as an Important Structure of Nonsteroidal Anti-Inflammatory Drugs to Uncouple Mitochondrial Oxidative Phosphorylation. *Biochem. Pharmacol.* **1999**, *58* (5), 861–865. [https://doi.org/10.1016/S0006-2952\(99\)00163-X](https://doi.org/10.1016/S0006-2952(99)00163-X).

References

- (194) Masubuchi, Y.; Saito, H.; Horie, T. *Structural Requirements for the Hepatotoxicity of Nonsteroidal Anti-Inflammatory Drugs in Isolated Rat Hepatocytes 1*; 1998.
- (195) Danley, D. E. Crystallization to Obtain Protein-Ligand Complexes for Structure-Aided Drug Design. *Acta Crystallogr. Sect. D Biol. Crystallogr.* **2006**, *62* (6), 569–575. <https://doi.org/10.1107/S0907444906012601>.
- (196) Rabilloud, T.; Heller, M.; Rigobello, M.-P.; Bindoli, A.; Aebersold, R.; Lunardi, J. The Mitochondrial Antioxidant Defence System and Its Response to Oxidative Stress. *Proteomics* **2001**, *1* (8), 1105–1110. [https://doi.org/10.1002/1615-9861\(200109\)1:9<1105::AID-PROT1105>3.0.CO;2-M](https://doi.org/10.1002/1615-9861(200109)1:9<1105::AID-PROT1105>3.0.CO;2-M).
- (197) Food, E.; Authority, S. Conclusion on the Peer Review of the Pesticide Risk Assessment of the Active Substance Diphenylamine. *EFSA J.* **2012**, *10* (1), 1–59. <https://doi.org/10.2903/j.efsa.2012.2486>.

9. Publications and presentations

Characterization of novel diphenylamine compounds as ferroptosis inhibitors.

L. Hinder, A.L. Pfaff, R.E. Emmerich, S. Michels, M. Schlitzer, and C. Culmsee (2021) *Journal of Pharmacology and Experimental Therapeutics* (JPET-AR-2021-000534), Accepted, Mai 2021

Development of photoactivatable t-Bid constructs

L. Hinder, M. Plessner, C. Krasel, C. Culmsee, Retreat, Rauischholzhausen, Germany, 16.06 – 17.06.2019, poster presentation

Characterization of novel diphenylamine (DPA) derivatives as ferroptosis inhibitors

BPC seminar, 19.01.2021, oral presentation

10. Meetings and conferences

World Congress on Targeting Mitochondria. Berlin, Germany. 27.10 – 29.10.2019

11.Acknowledgments/ Danksagung

Die Seiten 148 und 149 enthalten personenbezogenen Daten und sind deshalb nicht in der elektronischen Version verfügbar.

Die Seiten 148 und 149 enthalten personenbezogene Daten und sind deshalb nicht in der elektronischen Version verfügbar.

12. Curriculum vitae

Die Seite 150 enthält personenbezogene Daten und ist deshalb nicht in der elektronischen Version verfügbar.